University of California
Santa Barbara

Design, Modeling, and Control of Soft Robots

A dissertation submitted in partial satisfaction
of the requirements for the degree

Doctor of Philosophy
in
Mechanical Engineering

by

David Arthur Haggerty

Committee in charge:

Professor Elliot Hawkes, Chair
Professor Igor Mezic
Professor Tyler Susko
Professor Yon Visell

September 2023

The Dissertation of David Arthur Haggerty is approved.

Professor Igor Mezic

Professor Tyler Susko

Professor Yon Visell

Professor Elliot Hawkes, Committee Chair

August 2023

Design, Modeling, and Control of Soft Robots

by

David Arthur Haggerty

To the unnamed giants upon whom's shoulders I stand; and to my mother, father, and two brothers, who helped me stand upon them.

Acknowledgements

First and foremost, I am extremely grateful for my family, all of whom have supported my (at times wayward) path from childhood through to my degree. Without them, none of this would be possible.

Next, I will be forever indebted to my Advisor, Elliot Hawkes. Elliot believed in me, challenged me, tolerated me, and supported me in a complex, yearslong period of growth. The advisor / advisee relationship is unique, to say the least, and ours has played a crucial role in my development as a scientist, mentor, and person.

I would like to express a special thanks for the friends that have stayed by my side through this chapter of my life. Most notably would be James Cazzoli, whom I have relied on in more circumstances than I can ever likely repay.

Special thanks to my RPI mentors, especially Kyle Wilt. Kyle gave me the opportunity to test myself as a proto-Ph.D. student, providing me with an engineering challenge and making himself available for regular support, but leaving the research process up to me to discover and implement. It was working under his direction that confirmed my interest in grad school. I'm sure that one day, the paper I drafted with our findings will be submitted to IEEE!

To my labmates: Nicholas Naclerio, Charlie Xiao, Luke Gockowski, Matt Devlin, Patrick Curtis, Anna Alvarez, and Drew Boyles - thank you all for the support, both in my finest hour and in my lowest moments. To Michael Banks, my trusted collaborator and confidant, don't ever change.

Thanks to my external collaborators, particularly Ervin Kamenar and Alan Cao for their help on our *Science Robotics* paper. And to Laura Blumenschein and Margaret Coad, who were consistently gracious wealth's of information, and who were unknowingly supportive during a particularly difficult period of my Ph.D.

Thank you to Trevor Marks, who regularly saved the day with last-minute provisions and insight.

I also wish to thank the front office staff, particularly Amanda Hart for putting an entire department on her shoulders and not backing down from the challenge, and Julie Dunson, Melecia Valdez, and Laura Reynolds for regularly coming to the rescue when I inevitably waited until the last minute (or, in many cases, beyond the last minute), and keeping my research and academic progress in motion.

Finally, this work would not have been possible without the financial support of the National Science Foundation (Grant 1935327) and the Lucile and David Packard Science and Engineering Fellowship (Award 1944816).

Curriculum Vitæ

David Arthur Haggerty

Education

2023	Ph.D. in Mechanical Engineering, University of California, Santa Barbara.
2018	B.S. in Mechanical Engineering and Design, Innovation, and Society, Rensselaer Polytechnic Institute.

Research and Work Experience

2021-present	*Founder and CEO.* Vine Medical, Inc., Goleta, California.
2021-2023	*Ph.D Candidate.* Hawkes Lab, Dr. Elliot Hawkes, UC Santa Barbara.
2018-2021	*Graduate Research Assistant.* Hawkes Lab, Dr. Elliot Hawkes, UC Santa Barbara.
2017-2018	*Undergraduate Research Assistant* Laboratory for Noise and Vibration Control Research, Dr. Kyle Wilt, Rensselaer Polytechnic Institute.
2016-2017	*Founder and CEO* Nova Health Works, Troy, NY.

Honors and Awards

2018	Professional Leadership Program Fellow
2018	Tau Beta Pi Engineering Honor Society
2017	Leadership Educators Advising Peers (LEAP) Fellow
2015-2018	RPI Dean's List: Fall '15 - Spring '18
2015-2016	Startup Founder of the Year

Service and Teaching

Laguna Blanca High School Science Mentor
Mentored a high school student in a year-long project to develop her engineering skills via a structured soft robotics design objective.

School for Scientific Thought
Led a 6-week, hands-on course for 11 California High School students interested in robotics, covering general soft robotics topics that culminated in a design challenge.

Undergraduate Mentor
Provided in-depth mentorship for an undergraduate student from UC Irvine, providing him with a research opportunity that included soft robot design, modeling, and validation testing in the Stanford Cadaver Lab.

Teaching Assistant
UCSB Dynamics, Spring '21
UCSB Dynamics, Summer '20
UCSB Soft Robotics, Winter '20
UCSB Dynamics, Summer '19
UCSB Junior Design, Spring '19

Journal Publications

1. **Haggerty, D. A.**, Banks, M.J., Kamenar, E., Cao, A.B., Curtis, P.C., Mezić, I., & Hawkes, E. W. (2023). Control of Soft Robots with Inertial Dynamics. Science Robotics, 8(81).
2. **Haggerty, D. A.**, Naclerio, N. D., & Hawkes, E. W. (2021). Hybrid vine robot with internal steering-reeling mechanism enhances system-level capabilities. IEEE Robotics and Automation Letters, 6(3), 5437-5444.
3. Blumenschein, L. H., Coad, M. M., **Haggerty, D. A.**, Okamura, A. M., & Hawkes, E. W. (2020). Design, modeling, control, and application of everting vine robots. Frontiers in Robotics and AI, 7, 548266.
4. Naclerio, N. D., Kerst, C. F., **Haggerty, D. A.**, Suresh, S. A., Singh, S., Ogawa, K., ... & Hawkes, E. W. (2019). Low-cost, continuously variable, strain wave transmission using gecko-inspired adhesives. IEEE Robotics and Automation Letters, 4(2), 894-901.

Refereed Conference Publications

5. Wang, S., Zhang, R., **Haggerty, D. A.**, Naclerio, N. D., & Hawkes, E. W. (2020, May). A dexterous tip-extending robot with variable-length shape-locking. In 2020 IEEE International Conference on Robotics and Automation (ICRA) (pp. 9035-9041). IEEE.
6. Kamenar, E., Ćrnjarić-Žic, N., **Haggerty, D.A.**, Zelenika, S., Hawkes, E. W., & Mezić, I. (2020, September). Prediction of the behavior of a pneumatic soft robot based on Koopman operator theory. In 2020 43rd International Convention on Information, Communication and Electronic Technology (MIPRO) (pp. 1169-1173). IEEE.
7. Devlin, M. R., Young, B. T., Naclerio, N. D., **Haggerty, D. A.**, & Hawkes, E. W. (2020, October). An untethered soft cellular robot with variable volume, fric-

tion, and unit-to-unit cohesion. In 2020 IEEE/RSJ International Conference on Intelligent Robots and Systems (IROS) (pp. 3333-3339). IEEE.

8. **Haggerty, D. A.**, Naclerio, N. D., & Hawkes, E. W. (2019, November). Characterizing environmental interactions for soft growing robots. In 2019 IEEE/RSJ International Conference on Intelligent Robots and Systems (IROS) (pp. 3335-3342). IEEE.

Conference Presentations

1. "Vine Robotics", MARS Conference, Ojai, CA, 2022 (demo support and presenter assistant).
2. "Hybrid vine robot with internal Steering-Reeling Mechanism enhances system-level capabilities", presentation at the International Conference of Robotics and Automation (ICRA), Xi'an, China (virtually presented), 2021.
3. "Characterizing Environmental Interactions for Soft Growing Robots," presentation at IEEE/RSJ International Conference on Intelligent Robots and Systems (IROS), Macau, China, 2019.

Patent Applications

D. Haggerty and E. Hawkes, "Active reeling and steering control of a vine robot." WIPO WO2022192190A1

D. Haggerty, D. Drover and E. Hawkes, "Vine robot tracheal intubation device" WIPO WO2021025911A1

Select Press

Veritasium YouTube video with over 32M views as of 7/23 "This unstoppable robot could save your life," 2021.

Select Grants

NSF Small Business Innovation Research (SBIR) Phase I, "A Soft, Tip-Growing, Self-Deploying Endotracheal Tube that Enables Visualization-Free Intubation," (PI: David Haggerty), $275k. Wrote and manage.

CDMRP Rapid Development and Translational Research Award, "A Biomimetic Tip-Growing, Self-Deploying Intubation Device for Safer, More Effective Airway Management in Austere, Far-Forward Environments" (PIs: David Haggerty and Elliot Hawkes). $3.165m. Wrote and manage. Product expected 2025.

Packard Foundation, "'Artificial Tip-growth as a New Paradigm for Minimally Invasive Patient Care", (PI: Elliot Hawkes), $950k. Provided preliminary data and figures. 2020-2023.

NSF EFRI, "C3 SoRo: Koopman Operator Theory and Light-modulated Materials: A New Paradigm for Controllable C3 ("C4") Robots.", (PI: Elliot Hawkes), $2m. Provided preliminary data and figures. 2020-2023.

Abstract

Design, Modeling, and Control of Soft Robots

by

David Arthur Haggerty

Beginning in the second half of the 20th century, robots have played a growing role in numerous manufacturing sectors. As we move toward the second quarter of the 21st century, robots are still primarily in the factory, with few successful attempts to address new applications outside the factory – in less structured environments that require close interaction with humans. In the past decade, soft robotics has emerged as a potential alternative design direction due to its inherent safety and embodied intelligence, but its reduction to practice on a commercial scale has been limited, in part due to the nonlinearity and associated control complexity of soft systems. In this work, we seek to advance the performance of soft robots via insights gained from analytical and data-driven modeling efforts, which enable new design and control capabilities.

We begin by first seeking to understand the fundamental behaviors various soft robotic systems. In Chapter 2, we develop closed-form models of "vine robots," a type of soft, growing robot that changes length by adding material to its tip and their interactions with the environment. Next, we leverage those insights to design novel mechanisms that overcome performance limitations in Chapter 3,developing a novel mechanism that enables vine robots to access larger workspaces.

We then turn to data-driven modeling, leveraging a modern modeling technique to gain physical insights from a continuum soft arm performing dynamic tasks. In Chapter 4 we apply this method to enable accurate control of two soft robot arms in new regimes, controlling inertial motions that allow a soft arm to both catch and throw a ping pong

ball.

Finally, in Chapter 5, we describe the culminating work aimed at translating soft robotics to broad commercial application, as we develop the world's first soft robotic intubation system that enables life-saving, expert-level performance in novice hands. While there is yet more work to be done, this body of scientific knowledge will help set the groundwork to advance soft systems into everyday life.

Contents

Chapter 1

Introduction

Robotics has played an integral role in shaping modernity from medicine to manufacturing. Whether it is the Intuitive Surgical Da Vinci Robot in the Operating room, or the KUKA arc welding robot arm on the Tesla manufacturing line, such systems have proven invaluable in delivering repeatable, accurate, and precise results previously unattainable by humans alone [1,2].

Unfortunately, a significant limitation arose when trying to translate these systems to novel, unstructured and dynamic environments: the same control architechtures that provided precision and repeatability in controlled environments were ill-suited to providing dynamism and flexibility in uncontrolled environments [3–6]. More generally, the recognition that there are insufficient stability and safety margins in novel environments has required the introduction of new methods of modeling in control - primarily via large troves of data from which learning algorithms develop a rough view of the nonlinear modeling and control landscape [7].

Alternatively, soft robots have become an object of keen study over the past decade in response to these challenges [8–10]. By looking to bioinspiration for new frontiers in robotics, researchers have started an exponentially growing new field [11]. While past efforts have looked to capture the span of possibilities for a given operating environment in the source code of the controller, soft robotics realizes that "embodied intelligence" via compliance allows for much of this complexity to be offloaded to the mechanical system itself [12–14]. Unfortunately, this comes with a Faustian bargain: what you get in mechanical intelligence, you give in nonlinear dynamics.

Thus, there is a major obstacle in the translation of soft robotics research for meaningful societal impact: they are extraordinarily difficult to effectively model and control. This realization has been central to my work throughout my Ph.D., setting the intention to use both analytic and data-driven modeling to unlock new capabilities in soft robotics. Once effectively understood, the subsequent design cycle can be accentuated

via insight-driven design decisions, with some *a priori* understanding of what variables are inside and outside the "controllable subspace," so to speak. This practice is shown in the following chapters, with Chapters 2 and 4 describing analytic and data-driven modeling techniques, respectively, and by Chapter 3 applying modeling insights unearthed in Chapter 2. Finally, Chapter 5 attempts to take this effort to the logical continuation: applying model-based insights to develop a human-enhancing technology in airway management.

1.1 Soft Robotics and Vine Robots

Soft robotics, as defined by Kim et al. in [15], is a field concerned with the study of systems with "bioinspired capabilities that permit adaptive, flexible interactions with unpredictable environments" (examples in Figure 1.1). While there have been early applications of this practice since at least the 1950s, the field began a period of rapid growth in the early 2010s with the work of a few pioneering researchers [16–20].

Since then, numerous different embodiments of this class of system have been developed, including the two subtypes of focus in this work: the "vine robot" (as conceived in [25] and [26]), and the static-length continuum arm (as inspired by the elephant trunk, and shown in such works as [16,27–29]. Both of these systems intentionally include compliance that enable unique capabilities compared to rigid robots, as will be shown throughout the following chapters.

1.1.1 Vine robots

Vine robots move via tip extension, which is distinct from locomotion or other animal-like whole body movements. Whereas movement strategies like locomotion are defined by translation of the body from one location to another [30], movement by tip extension

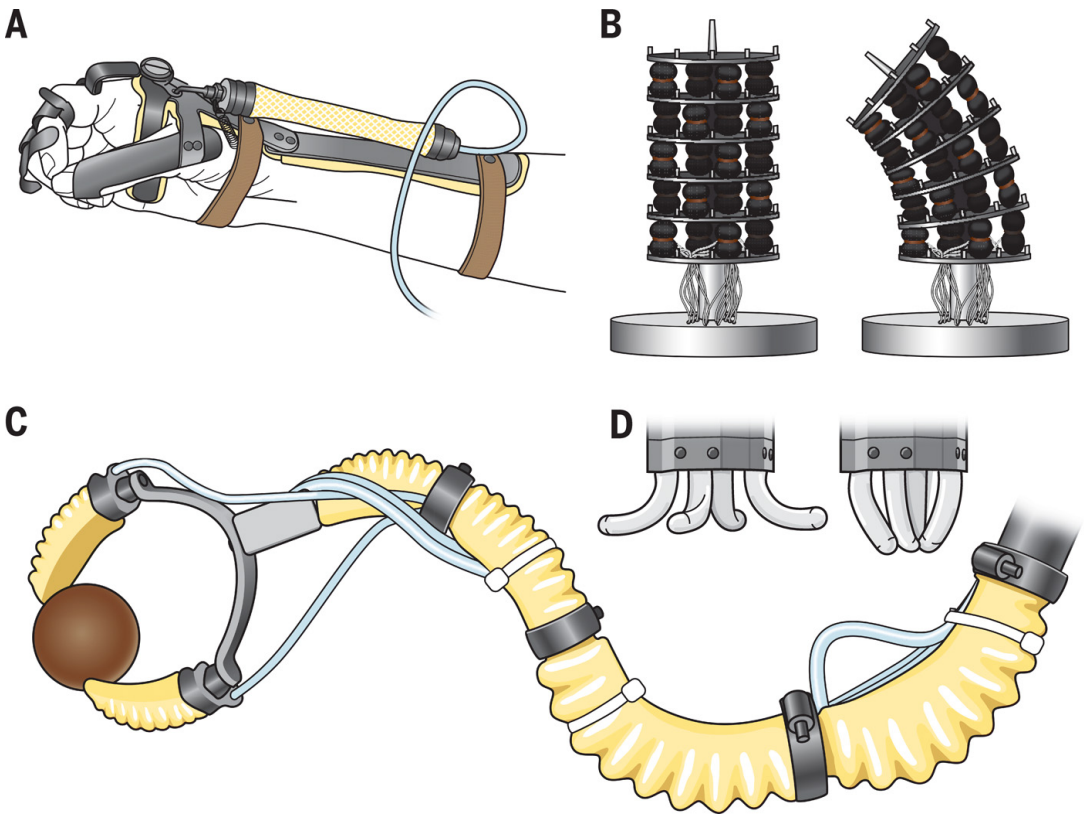

Figure 1.1: (A) The wearable exoskeleton powered by soft artificial muscles, made by McKibben in 1957 for his daughter with a paralyzed hand [21]. (B) The Orm, a soft pneumatic continuum manipulator from 1966 [22]. (C) A soft pneumatic elephant trunk–inspired manipulator from 1984 [23]. (D) A flexible microactuator (12 mm diameter) from 1992 [24]. Figure from [11], reprinted with permission from AAAS. Credit: Kellie Holoski/Science Robotics.

functions by lengthening the body [31], reducing or completely eliminating the need to translate relative to the environment. This form of movement seen in nature across scales and kingdoms, from single-cell pollen tubes [32] and micro-scale hyphae [33] to creeping vines [34] and the proboscises of certain worms [35,36].

Replicating elements of tip growth in robotic systems has two main benefits (Figure 1.2b). First, because only the tip moves, there is no relative movement of the body with respect to the environment which enables easy movement through constrained environments. Second, as the tip moves, the body forms into a structure in the shape

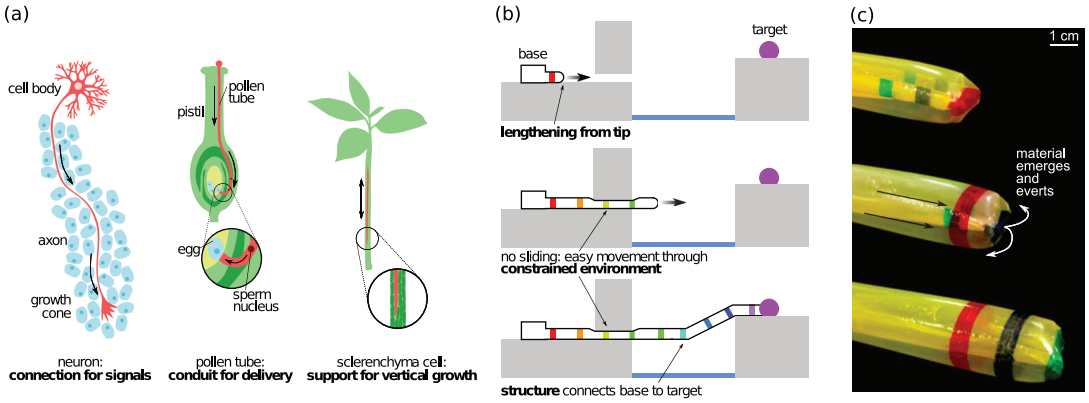

Figure 1.2: The biological inspiration for and basic properties of tip growth, and our implementation of artificial growth via eversion. (a) Examples of biological systems that grow to navigate their environments. (b) Schematic representing growth by tip-extension. (c) Artificial growth created by pressure-driven eversion of a flexible, thin-walled tube. Licensed from Frontiers under CC-BY 4.0.

of the tip's path, which can be used for payload delivery, force transfer or self-support, and physical construction. Unlike locomotion, which depends on the reaction forces and mechanical properties of the environment, growth allows vine robots to transfer forces through their bodies, back to their fixed base. Therefore forces can be generated independent of the contact conditions between the robot tip and the local environment. Tip growth as presented in [26] (utilizing pressure-driven "eversion" (i.e., turning inside out) of flexible, thin-walled material) is the focus of this work.

1.1.2 Soft continuum arms

Continuum arms are those that exhibit a high slenderness ratio (i.e. a small diameter relative to its length) and high degrees of freedom. Soft continuum arms are additionally constructed out of a soft backbone (cast silicone, thin-film plastics or fabrics), and inherit their structural stability via pneumatic or hydraulic pressurization [15,37,38]. Actuation mechanisms can include tendon-driven and pressure-driven techniques, such as pneumatic artificial muscles (PAMs), inverse pneumatic artificial muscles (IPAMs), and series pouch

motors (SPMs). Compared to the rigid robots mentioned above, they are significantly safer to cooperatively operate with and amongst humans. In this work, we focus on PAM-driven soft continuum arms constructed out of thin-film airtight fabrics (such as those described in [39]), including with some helical actuation as described in [40].

1.2 Permissions and Attributions

1. The content of Chapter 1 is, in part, adapted from a collaboration with Laura Blumenschein, Margaret Coad, Elliot Hawkes, and Allison Okamura which originally appeared in *Frontiers in Robotics* [41]. Reprinted with permission under CC-BY 4.0.

2. The content of Chapter 2 is the result of a collaboration with Nicholas Naclerio and Elliot Hawkes. It originally appeared in *IROS 2019* [42]. DOI: `https://doi.org/10.1109/IROS40897.2019.8968137`.

3. The content of Chapter 3 is the result of a collaboration with Nicholas Naclerio and Elliot Hawkes. It originally appeared in *Robotics and Automation Letters* [43]. DOI: `https://doi.org/10.1109/LRA.2021.3072858`.

4. The content of Chapter 4 is the result of a collaboration with Michael Banks, Ervin Kamenar, Alan Cao, Patrick Curtis, Igor Mezić, and Elliot Hawkes. Major findings originally appeared in *Science Robotics 2023* [44]. DOI: `https://doi.org/10.1126/scirobotics.add6864`. Early results were published at *arXiv* [45]. DOI: `https://doi.org/10.48550/arXiv.2011.07939`.

5. The content of Chapter 5 is a collaboration with James Cazzoli, Elliot Hawkes, David Drover, Daenis Camire, Lichy Han, and numerous other physicians, paramedics,

and medical providers. This work is due to be presented at various conferences in 2023, and is preparing for submission for publication in 2024.

Note: In reference to IEEE copyrighted material which is used with permission in this thesis, the IEEE does not endorse any of the Univeristy of California's products or services. Internal or personal use of this material is permitted. If interested in reprinting/republishing IEEE copyrighted material for advertising or promotional purposes or for creating new collective works for resale or redistribution, please go to `http://www.ieee.org/publications_standards/publications/rights/rights_link.html` to learn how to obtain a License from RightsLink. If applicable, University Microfilms and/or ProQuest Library, or the Archives of Canada may supply single copies of the dissertation.

Chapter 2

Analytical Modeling: extracting design insights from closed-form solutions

As my first manuscript in grad school, this work is one of my more humble publications. Yet it is arguably the one I most rely on in my day-to-day life, be it on the specific findings or abstractly. This reflection is I think emblematic of the extreme value to be found in some degree of (hopefully useful) mathematical modeling of a physical system. These efforts unearth the fundamental design variables that inform the dimensions along which the designer has or has not agency, enabling either quick exploit or intelligent avoidance of specific design avenues.

2.1 Background

At this point in 2018 / 2019, we had a relatively primitive understanding of the kinetic nature of environmental interactions of vine robots. Previously, work by Greer et al. [46] and Blumenschein et al. [47] had focused on interaction kinematics and free-space kinetics, respectively, but left unexplored the quantification of interaction forces during both glancing and head-on collisions with the environment. My work was an effort to synthesize and extend the two, enabling the development of a composite model of growth forces required to traverse a constrained path.

This effort unearthed a variety of design insights based on this modeling - how material properties affect performance, how path planning enables design contraints, and how design choices enable new capabilities. As such, while just a conference paper published in my first year, it both set the intention for my work in grad school, and enabled ongoing, thoughtful review of design choices in future projects.

2.1.1 Abstract

Soft, tip-extending devices, or “vine robots,” are a promising new paradigm for navigating cluttered and confined environments. Because they lengthen from their tips, there

is little relative movement of the body with the environment, and the compressible nature of the device allows it to pass through orifices smaller than its diameter. However, the interaction between these devices and the environment is not well characterized. Here we present a comprehensive mathematical model that describes vine robot behavior during environmental interaction that provides a basis from which informed designs can be generated in future works. The model incorporates transverse and axial buckling modes that result from growing into obstacles with varying surface normals, as well as internal path-dependent and independent resistances to growth. Accordingly, the model is able to predict the pressure required to grow through a given environment due to the interaction forces it experiences. We experimentally validate both the individual components and the full model. Finally, we present three design insights from the model and demonstrate how they each improve performance in confined space navigation. Our work helps advance the understanding of tip-extending, vine robots through quantifying their interactions with the environment, opening the door for new designs and impactful applications in the realms of healthcare, research, search and rescue, and space exploration.

2.2 Introduction

In contrast to traditional rigid robots, which are well suited for strength, precision, and repeatability, soft robots easily adapt to changing environments without complex mechanisms and control schemes [38,48]. Tip-extending, vine-inspired robots, or "vine robots," are a particularly exciting new class of soft robots that can lengthen like a vine to navigate challenging environments. Various skin-eversion robots have been presented [25,49–52], with the most recent showing the ability to lengthen by thousands of percent, steer autonomously, and move at rates comparable to animal locomotion [26]. These pneumatic robots are composed of a thin-walled membrane, inverted inside itself, such

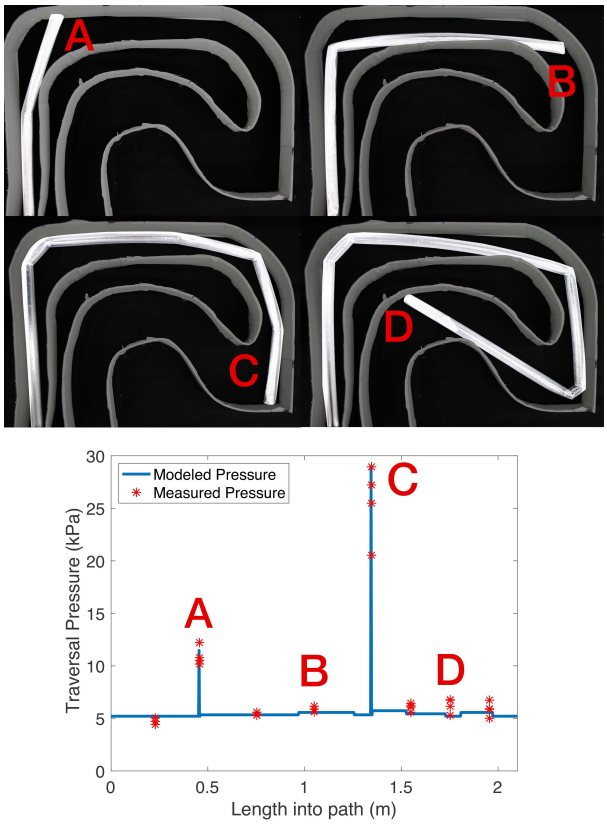

Figure 2.1: Characterization of the environmental interactions of a soft tip-extending robot. *Top:* Sequence of photos showing the extending "vine" robot navigating a constrained, tortuous path. *Bottom:* The required pressure to cause growth as a function of position along path. Letters correspond to positions shown in images.

that when pressurized, new material passes out through the tip, allowing it to "grow." This characteristic behavior eliminates the need for friction between the robot body and its environment in order to progress along its path. Further, because the tube remains largely stationary with respect to its surroundings, there is little sliding with respect to the environment, and the robot can squeeze through tight spaces. Finally, it is able to passively buckle around difficult obstacles with minimal force applied to the environment, avoiding the control complexity of other continuum robots while ensuring the safety of both the device and its surroundings [53–55]. These advantages have led to further work on vine robots including active steering [46], medical applications [56], archaeology [57], and burrowing [58].

While these demonstrations show the potential of vine robots, a systematic and rigorous formalization of the principles underlying vine robot behavior is lacking. Toward this goal, the contributions of this paper are: i) a refinement of the model for vine robots moving in free space as initially presented by Blumenschein et al. [47], ii) a new model of vine robots moving in constrained spaces that characterizes environmental interaction forces on the robot, and iii) implementations of design insights derived from this model that show substantially improved performance over previous vine robot designs.

What follows is a description of the analytical model we developed, followed by a results section that validates the model. We then present three design implications in real systems inspired by our analysis. We conclude with a discussion of the strengths and limitations of the current investigation, as well as the planned next steps.

2.3 Modeling

The goal of this section is to present our mathematical models describing the individual components governing the behavior of vine robots as they move through unconstrained and constrained environments. The modeling will provide the required pressure to extend based off the varying interaction forces produced by contact with its environment, dictated by the morphology and materials of the robot body and the shape of the path through which it is passing. We begin with a description of the device moving through an unconstrained environment, where we refine the model previously presented by Blumenschein et al. [47]. We then build upon this to develop a new model that considers the constrained case where sharp turns and obstacles are present.

2.3.1 Extension in an Unconstrained Environment

The physics governing the growth of pressure-driven, tip-everting devices in unconstrained environments can be described by two basic components: a path dependent term and a path independent term. This mathematical description was introduced in Blumenschein et al. [47], inspired by the Lockart-Ortega equation describing plant cell growth. The contribution of this section is to better characterize the effect of large amounts of total curvature on required growth pressure.

The basic equations from Blumenschein et al. [47] can be expressed as follows:

$$\begin{aligned} (PA)_{evert} &= (PA)_{ind} + (PA)_{dep} \\ \text{where :} \quad (PA)_{ind} &= YA + (\frac{1}{\phi}v)^{\frac{1}{n}}A, \\ (PA)_{dep} &= \mu_s wL + \sum_i Ce^{\frac{\mu_c L_i}{R_i}}, \end{aligned} \tag{2.1}$$

where the subscripts *evert*, *ind*, and *dep* indicate eversion pressure (i.e. pressure required to grow from the tip), the path-independent terms, and the path-dependent terms, respectively. P is the internal pressure, Y is the yield pressure required to evert body material, A is the device's cross-sectional area, ϕ is the material extensibility, v is the tip velocity, n is a power term close to unity, μ_s is the length dependent friction coefficient, w is the normal force exerted per unit length by the internal robot tail (i.e. the length of robot body inverted inside itself), L is the length of the soft robot body, C is a curve-fit constant, μ_c is the curvature dependent friction coefficient, L_i is the length of robot tail experiencing the ith instance of curvature, and R_i is the radius of said curvature.

For this work, we are interested in paths less than 5 m long and average growth speeds less than 0.05 m/s. Accordingly, certain terms dominate in both the path independent and path dependent equations in (2.1), rendering others negligible. In the path dependent case, the curvature component exponentially increases, overpowering the linear

length dependent friction force, allowing us to neglect it. Further, with a growth velocity under 0.05 m/s, the velocity term constitutes roughly 5% of the yield term in the path independent equation, allowing us to also neglect it. As such, the general solution in (2.1) simplifies to:

$$(PA)_{evert} = YA + \sum_i Ce^{\frac{\mu_c L_i}{R_i}}. \tag{2.2}$$

To add to this work, we characterize the C coefficient in the path dependent term. Blumenschein et al. used an experimental setup that required a multi-parameter best fit that found values for both C and μ simultaneously. Unfortunately, this resulted in nonphysically large variations in μ and accordingly inaccurate values of C. To address this challenge, we note that the curvature dependence term is based on the capstan equation,

$$T_{out} = T_{hold}\, e^{\mu\theta}, \tag{2.3}$$

where T_{out} is the output tension after a curve, T_{hold} is the input tension before the curve, and θ is the angle of the curvature experienced. The C coefficient corresponds to T_{hold}, but is not readily measurable in the case of normal extension of the robot, given its very small magnitude. This tension is due to the frictional force of the tail inside the body of the device before the curve. In order to estimate this capstan coefficient, we systematically vary this input tension with known loads and yield values, determine the exponential parameter, then solve for the capstan coefficient when no load is applied. Section 2.4.1 describes our experimental setup for this characterization.

2.3.2 Extension in a Constrained Environment

Fundamental to the operation of vine robots is movement through constrained environments where movement is impeded by obstacles. Due to the axial stiffness of the materials generally comprising vine robots, body buckling becomes the only appreciable form of reconfiguration around obstacles or in paths with turns. Self-buckling, or buckling caused by the forces the growing robot applies to the environment, occurs in two modes: axial and transverse. The pressure required to cause these self-buckling modes can be much higher than during growth in unconstrained environments, meaning we must consider an additional, higher pressure when the device is required to pass through a tight curve or around an obstacle. We present an appropriate model here.

The simplest buckling mode is that of the transverse case, where buckling occurs due to loading perpendicular to the direction of growth. These deflections have been shown to be predictable [46], however in a kinematic model the internal pressure of the robot and the forces applied to the environment were not considered. Hammond et al. [59], among others [60,61], have shown that this restorative internal moment is simply

$$M_{int} = \pi P R^3 = F_{tr} L, \tag{2.4}$$

where M_{int} is the restorative moment due to internal pressure, r is the device radius, P is the internal pressure, F_{tr} is the transverse load applied, and L is the unconstrained length. In the case of a vine robot navigating a closed path, the force F_{tr} is produced by internal pressure and its magnitude is a function of the angle of incidence with its path boundary. Taking a moment balance about the nearest constrained point along the body of the robot, illustrated by Figure 2.2, and assuming quasi-equilibrium just prior to the point of buckling yields:

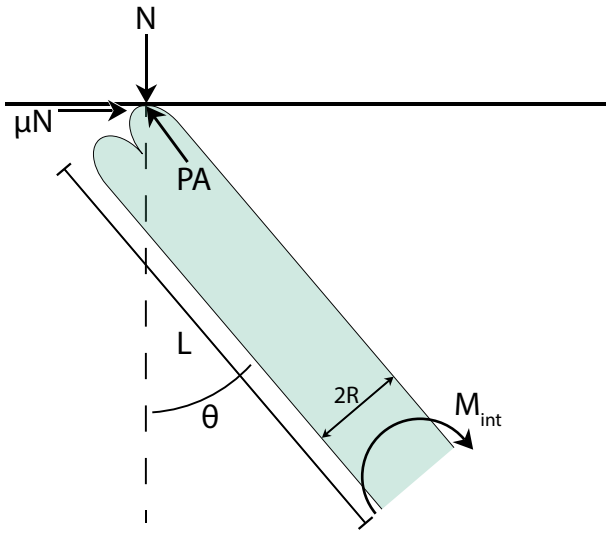

Figure 2.2: Illustration of free body diagram used to determine relationship in (2.6).

$$M_{int} = NLsin\theta - \mu NLcos\theta, \tag{2.5}$$

where N is the normal force generated by an interaction with the path and L is the unsupported length. Realizing N is a function of internal pressure, (2.5) reduces to a simple geometric relationship:

$$\frac{R}{L} = \frac{sin\theta - \mu cos\theta}{cos\theta + \mu sin\theta}, \tag{2.6}$$

where θ is taken to be the angle of incidence with respect to the surface normal and μ is the coefficient of friction between the device and its boundary.

However, this relation simply represents the smallest value of the ratio of radius to unsupported length at a given angle, and as such can be treated as a lower angle bound. This allows for a conditional requirement to be developed: for a given robot radius and unsupported length, transverse buckling will occur at any angle of incidence larger than that which satisfies the equality in (2.6), denoted θ_{min}.

The other mode of buckling encountered in constrained paths is axial buckling. Axial

buckling mechanics for soft, inflated bodies differ markedly from those of traditional, rigid beams. While rigid body axial buckling is easily expressed through the Euler equation, the compressibility of air and the large ratio of tensile to compressive strength of polymer films is not captured in this model.

Here we invoke the work of Fichter [62], who presents a Euler-inspired, linearized axial buckling model for inflatable beams derived from a virtual work approach. This theory characterizes the inflatable beam critical load F_{cr} (i.e., the load that causes a complete loss of tension in one side of the beam and thus wrinkling) as the ratio product of beam stiffnesses (Euler buckling stiffness and shear stiffness, $P + G\pi rt$) to the sum of beam stiffnesses in a purely axial loading condition, expressed as:

$$F_{cr} = \frac{EI\frac{\pi^2}{L^2}(P + G\pi Rt)}{EI\frac{\pi^2}{L^2} + P + G\pi Rt}, \tag{2.7}$$

where, E is Young's Modulus, I is the second moment of area of the inflatable beam, L is the unconstrained length of the member, P is the force due to internal pressure, G is the shear modulus, r is the radius of the cylinder, and t is the wall thickness. When the everting robot extends into an obstacle, there is not an external load applied to the beam, but rather there is an interaction force produced by the robot attempting to lengthen. Thus the critical load becomes the force produced by internal pressure:

$$P_{cr}A = \frac{EI\frac{\pi^2}{L^2}(P_{cr}A + G\pi Rt)}{EI\frac{\pi^2}{L^2} + P_{cr}A + G\pi Rt} \quad where \quad F_{cr} = P_{cr}A \tag{2.8}$$

Solving this equation for critical buckling pressure, P_{cr}, generates a second degree polynomial. Isolating P_{cr} via the quadratic equation and taking the right-half plane solutions yields

$$P_{cr} = \frac{1}{2}\left[\sqrt{\left(\frac{G\pi Rt}{A}\right)^2 + \frac{4EGI\pi^3 Rt}{A^2L^2}}\right] - \frac{G\pi Rt}{2A}. \tag{2.9}$$

From this equation, we immediately see that resistance to buckling decreases with larger unsupported free lengths and lower elastic and shear moduli. As well, while not as readily apparent, upon plotting P_{cr} with varying R, we see smaller device diameters similarly lower resistance to buckling. Experimental validation of this relationship is presented in Section 2.4.2.

2.3.3 Full Model for Tortuous Path with Self-buckling

With the models from Sections 2.3.1 and 2.3.2, we are prepared to write a single equation for the case of a tortuous path with turns that produce both axial and transverse self-buckling. To form this full model, we estimate the direction of the contact normal between the tip of the device and the path. At larger contact angles, transverse buckling occurs and the device will follow the obstacle with it's tip [46]. When the angle between the surface normal and the direction of growth, S, falls below θ_{min} (see (2.6)) axial self-buckling occurs instead. When axial buckling occurs, we add the self-buckling pressure from (2.9) to the predicted pressure on a smooth path from (2.2):

$$P_{evert} = \frac{F_y}{A_{cs}} + \sum_i Ce^{\frac{\mu L_i}{R_i}} + \left\{ \begin{array}{l} P_{cr,i} \text{ for } S < \theta_{min}, \\ 0 \text{ otherwise.} \end{array} \right\}. \tag{2.10}$$

Here the effect of curvature is applied based on the summation of curvatures experienced by the remaining inverted tail, and buckling pressure only influences growth pressure at the leading instance of curvature producing a surface normal contact angle less than θ_{min}.

Tracking the remaining inverted tail is completed by creating a piecewise relationship between total device length and starting device length, knowing for each increment in robot body length there is a corresponding increment or decrement in tail length (for example, as the robot grows the tail length will first increase, matching the length of grown robot until half the material is deployed, and then will decrease until no tail remains inside the robot). While this composite model is only an approximation, future sections will show it usefully captures the observed basic behavior of the device (see Section 2.4.3).

2.4 Results

This section presents experiments verifying both the individual elements of the model ((2.10)) as well as the model as a whole, which predicts growth pressure as a function of device materials and morphology, and the shape of the path traversed.

2.4.1 Characterization of Capstan Coefficient

To characterize the capstan coefficient and expand upon the model presented by Blumenschein et al. in (2.2), we first determined the yield pressure inherent in our robot. Blumenschein et al. showed that yield force (force required to evert material from the tip), while dynamically complex, is a constant dependent on material, with yield pressure a function of cross sectional area. As such, multiple devices were tested with varying tail lengths, with pressure slowly increased until the device sustained tip growth.

These values were recorded using a Dwyer Instruments 626 Series pressure transmitter (0-205 kPa range, 0.25% full scale accuracy), and the minimum, maximum, and mean values were found to be 2.301, 4.036, and 3.210 kPa, respectively, based on 27 trials with a standard deviation of 0.509. These tests were conducted in both horizontal and

vertical orientations with little variation, likely due to tail weight contributing negligibly to the relatively high-force required to unfurl the tip material; rather, the range of values measured appeared to be mainly dependent on material condition at the tip. Thus, both vertical and horizontal orientation test values were used in averaging the yield pressure.

Next, we tested the pressure required to grow with various resisting tensions applied to the tail of the device. Two values of T_{hold} which were expected to dominate the latent tension produced by the loose tail were chosen. These values were produced by two masses (15 g and 20 g) suspended from the tail. A 9.25 cm rigid cylinder was cantilevered from a table with its axis parallel to the ground. The masses (first 15 g then 20 g) were adhered to the fully everted tip of the device, which was then completely inverted. With the axis of the device vertically oriented, such that the mass would produce a pure tension in the tail, wrap angles, in radians, between π and 4π, incremented by π, were tested (see Figure 2.3 for an illustration of the experimental setup). In each case, the pressure was slowly increased to the point of sustained tip growth, with pressure measurements recorded using the same Dwyer Instruments 626 Series pressure transmitter.

Four tests for each mass, at each wrap angle, were conducted, followed by the same regimen for a device with zero added mass. Figure 2.4 shows these results graphically, alongside the model presented in (2.10), while Table 2.1 presents the average value of each trial.

The exponential parameter, μ_c in (2.10) was determined in the first two cases by using the known values of T_{hold} and Y via curve fit in Matlab. This produced a value for μ_c of 0.222 in the 15 g case, 0.245 for 20 g, producing a mean value of 0.234 and a 9.25% difference between the two. Using this average value for μ_c and the measured values for Y, the value of T_{hold} was the subsequently determined to be 0.0824 N.

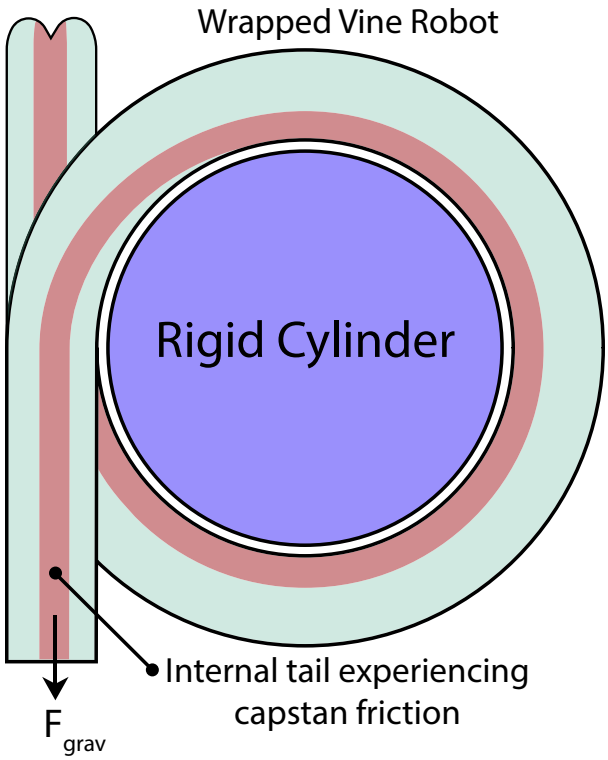

Figure 2.3: Illustration of capstan coefficient experimental setup. In this drawing, the suspended mass would be found in the lower left of the sketch noted as F_{grav}.

Table 2.1: Wrap Test Results (kPa)

Wrap Angle (rad)	π	2π	3π	4π
20 g mass	5.882	9.145	14.917	20.106
15 g mass	4.615	5.828	8.543	13.101
0 g mass	3.552	4.900	6.387	9.076

2.4.2 Validation of Self-buckling Model

Transverse buckling in vine robots occurs when a transverse interaction force produces a moment about the nearest supported point that exceeds that produced by internal pressure, as expressed in (2.4). Knowing that this force is similarly produced by internal pressure, no additional pressurization is expected to produce a transverse buckle, but instead the geometric relation shown in (2.6) need be satisfied. To verify this, a robot with a diameter of 2.4 cm was grown into a barrier at four different unsupported lengths

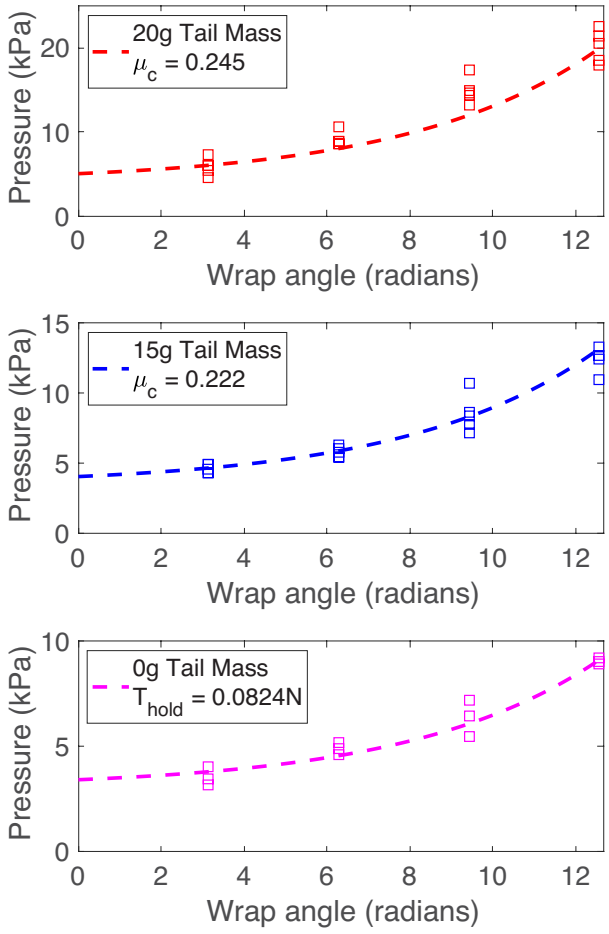

Figure 2.4: Three wrap tests, conducted with varying tail weights, with wrap angles ranging from π radians to 4π radians. *Top and middle:* Here, known tail masses give a known T_{hold}, allowing a single parameter fitting to yield values for μ_c. *Bottom:* Using the average value of μ_c found from the two cases above, we perform a single parameter fitting to yield the value of T_{hold} for no tail mass.

across four different angles.

In each case, the robot was secured at the specified buckle lengths (15.24, 22.86, 30.48, and 38.10 cm) oriented to the test angle with respect to the surface normal. Pressure was increased to just above the yield point and the robot was allowed to grow into a barrier. A success was recorded in the event of a natural buckle at no increased pressure, and a failure when no buckle occured. These results are presented in Fig. 2.5, alongside the theoretical minimum angle as predicted by (2.6).

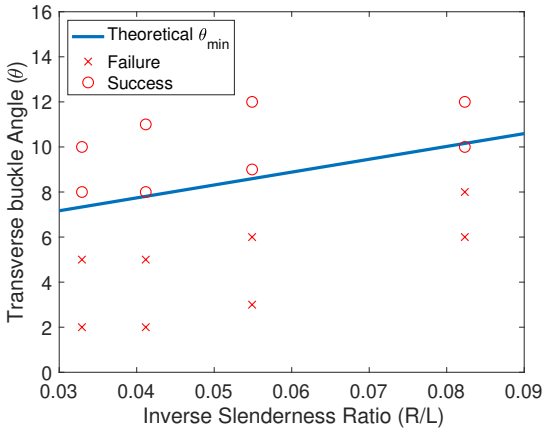

Figure 2.5: Experimental results of geometric conditions required to achieve transverse buckling. Unsupported length increases from right to left. The model from (2.6) is shown as the blue line.

The predicted axial buckling pressure in (2.9) depends on the Young's and shear moduli of the material, the device diameter, and the the length of the buckle section. The literature value of Young's modulus of LDPE used in this model was 303 MPa, alongside a shear modulus of 206 MPa [63,64].

Inserting these measured quantities into (2.8), and formulating (2.10) with zero curvature, expected values for critical pressure, P_{cr}, were developed for body lengths ranging from 25 cm to 76 cm and a device diameter of 2.4 cm. The robot body was inverted, constrained at the buckle length in question, pressurized to the point of slow, sustained growth, and allowed to grow into a barrier perpendicular to the direction of growth. Pressure was then slowly increased until the point of buckling, with measurements recorded using the pressure transmitter introduced in Sec. 2.4.1. This test was repeated four times for each length.

The results of these tests are displayed graphically in Figure 2.6, alongside the modeled behavior curve from (2.10), and average values are presented in Table 2.2. As seen in Figure 2.6, at large body lengths the device tracks closely with modeled values, however, at small body lengths the observed quantities begin to show higher variation.

Table 2.2: Critical Buckling Pressure (kPa)

Buckle Length (cm)	25.4	38.1	50.8	63.5	76.2
$P_{cr,ave}$, *measured*	27.689	15.763	9.993	6.170	4.654
P_{cr}, *predicted*	29.418	14.738	9.472	7.011	5.668

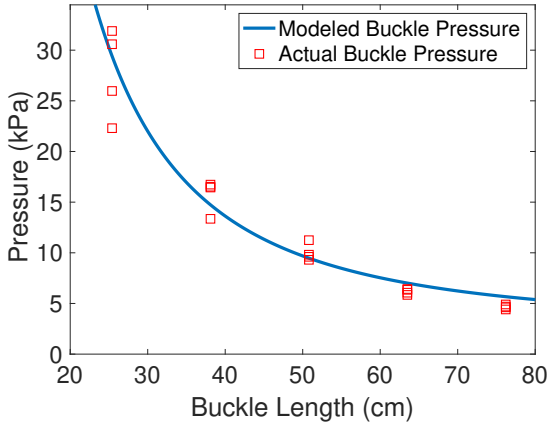

Figure 2.6: Experimental results of pressure required for axial buckling versus free length. The model from (2.10) is shown as a blue line.

2.4.3 Validation of Composite Model in a Constrained Path

The outcomes of Sections 2.4.1 and 2.4.2 were then combined to create a discretized path traversal model. Using (2.10) as the governing equation for the behavior of our device, a script was developed in Matlab to predict behavior. The shape of the path was discretized into a series of nominally straight sections interrupted by short curved sections. The instances of curvature were treated as point sources with known wrap angle. To track the amount of tail experiencing curvature, a simple linear relationship was developed relating initial device length to tail length reduction, knowing each unit increase in device length produces a unit decrease in remaining inverted tail (note: the vine robots in this investigation utilized a loose inverted tail, as opposed to the tail reel some vine robots employ [59]). The free length of the device, required for the critical buckling pressure in (2.10) and the transverse condition in (2.6), was estimated

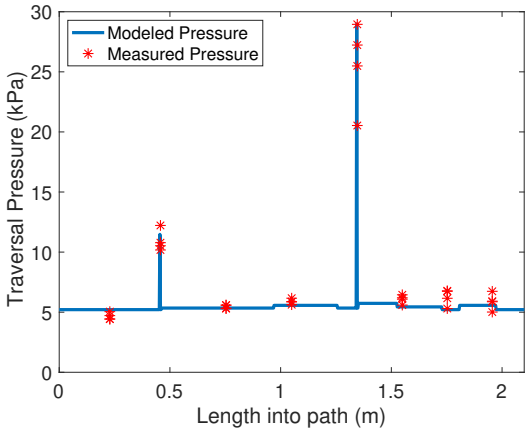

Figure 2.7: Experimental validation of the composite model, as also shown in Figure 2.1. The expected pressure produced by the composite model is shown by the blue line.

by the distance between curves. This composite model produced a tip location-specific pressure estimate to traverse the entire path. The value of S from (2.10) was estimated by estimating the obstacle tangent at the point of contact and measuring the resulting contact angle.

A rigid path was created for evaluation out of foam-core board. An arbitrary path was designed to include both axial and transverse buckling events, as well as to accumulate curvature. Using foam-core board as the substrate, 7.5 cm tall sections of foam-core was then used to form the outline of the path, and a clear acrylic sheet was used to enclose it. After construction, physical measurements for the path were input into the discrete model, and four tests were conducted to validate its accuracy. The device was inserted into one end of the physical model, and pressure was slowly increased until the point of sustained growth. Measurements were taken along straight lengths approximately every 20 cm, and peak pressure was recorded in instances of buckling. Fig. 2.7 shows the outcomes of each of these trials, overlaid on the predicted values created by the discrete model from (2.10) across the course presented in Fig. 2.1.

2.5 Design Implications

The model presented in (2.10) provides insights on how different design parameters of a vine robot affect its ability to navigate a given path. Below, we examine three such insights, as well as provide comparative tests for each.

2.5.1 Increased Membrane Compliance

The effect of membrane compliance on pressure reduction has as of yet not been investigated. To date, vine robots have been designed using a membrane material for which the modulus was selected to be high enough that negligible axial extension would occur while in operation. Such stiffness similarly meant that negligible bending occurred before buckling. While these materials are useful for creating free-standing structures [26], we see from the results of Sec. 2.3, that decreasing this modulus can have advantages when navigating a tortuous path. Examining (2.9), we see that the modulus of elasticity of the membrane increases the required pressure to buckle. Further, a lower modulus allows additional bending to occur in the body before buckling.

Such bending changes the tip contact angle, and can enable transverse buckling to occur in a situation that initially would have resulted in axial buckling. Critically, as can be seen in (2.6), transverse buckling requires no additional pressure to initiate, provided its geometric condition is met. We thus constructed two robot bodies out of anisotropic ripstop nylon - one with increased compliance, one traditionally rigid - and compared their ability to navigate the same tortuous path.

Each robot was constructed out of $50\,\mu m$ thick, silicone impregnated ripstop nylon fabric. By varying the thread orientation, compliance can be built in to the robot body. In the rigid case, the grid pattern was arranged parallel to the longitudinal axis, and at 45° to take advantage of the fabric bias [65] in the compliant case; this modification allows

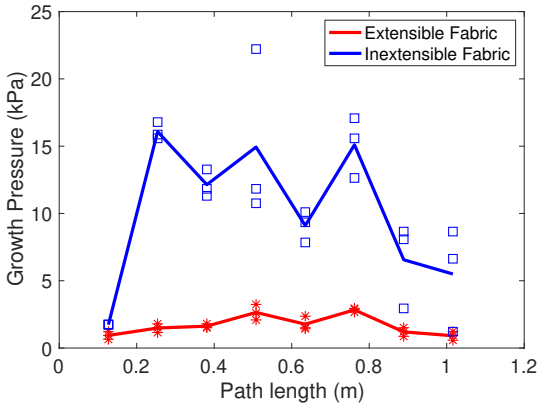

Figure 2.8: Effect of membrane compliance for traversing a path consisting of all axial buckling events. The solid lines denote the mean value for each case.

for variable strains when subjected to the same forces. As can be seen in Figure 2.8, the device built from axially elastic fabric performs significantly better than the inelastic, reducing the maximum pressure required to navigate the same path by a factor of nearly 7.

While these results are exciting, they are only preliminary and there is yet work to be done to fully characterize their behavior. Specifically, measuring their mechanical properties and verifying their behavior with the model presented are the immediate next steps, as the effect of a low material modulus may eliminate the axial consideration in (2.10) due to the significant bending produced prior to axial buckling.

2.5.2 Decreased Scale

The effect of scale on a vine robot's ability to navigate a constrained environment has not been previously investigated. Accordingly, we examine (2.10) and note that the diameter of the robot body has conflicting effects on different terms. A smaller diameter increases the internal pressure required to evert [47], however, a smaller diameter decreases the angle required for a transverse buckle to occur and, while not immediately clear in (2.9), a small diameter similarly reduces the pressure required to create an axial

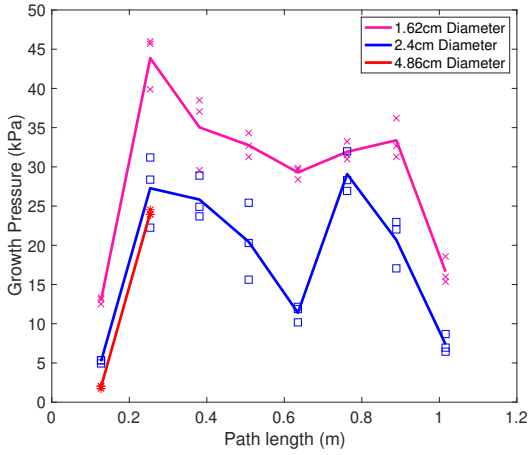

Figure 2.9: Effect of diametral scaling for traversing a path consisting of all axial buckling events. Solid lines denote the mean value for each case. Note: the 4.86 cm scale burst at the first buckle.

buckle. From this insight we conclude that, for a given path, the design objective should be to minimize device radius to the furthest extent possible, informed by maximum allowable pressures within the path. To investigate this, three different diameter devices were subjected to the same path and their traversal pressures were recorded, with results found in Figure 2.9. What was found is a balance exists between growth pressure and buckle pressure, wherein an optimal scale can be found. Specifically, growth pressure goes with r^2 whereas buckle pressure goes with r, and burst pressure goes with $1/r$ (as hoop stress goes with r). The 4.86 cm robot exceeded its burst pressure at the first buckle, while the 1.62 and 2.4 cm robot were both successful, and the 2.4 cm variant traversed at the lowest gauge pressure. It is similarly worth noting the 1.62 and 2.4 cm robot completed the path at roughly the same percentage of burst pressure ($\sim$65%).

2.5.3 Decreased Internal Tail Length

The most pernicious element of the model provided in (2.10) for navigating closed, tortuous paths is the pressure required to overcome capstan friction. The exponential

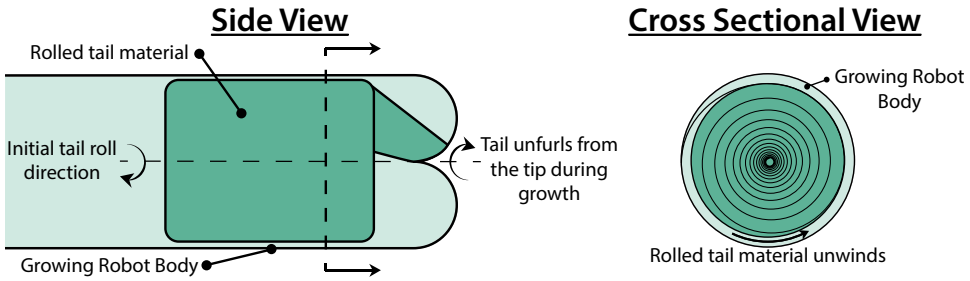

Figure 2.10: Illustration of method used to evaluate effect of reducing internal tail length. The Side View shows how the unfurling "pulls" the tail roll along, and the Rear View expresses the rolling method.

nature of the capstan component quickly approaches the burst pressure of these devices, and as such puts a strict limit on the lengths of tortuous paths accessible. Figure 2.4 verifies this relationship. As such, we investigate the impacts of eliminating this tail friction by rolling the inverted material into a tight wind, allowing it to 'ride' along with the tip of the device as it grows, illustrated in Figure 2.10. While there are many conceivable methods to store this tail material, such as S-folds, bellows, or simply stuffing the material at the tip, the rolled configuration was chosen for its ease in preparation using mechanical means.

Figure 2.11 highlights the effect of eliminating the tail for navigating tortuous paths. Two vine robots traversed a path constrained between concentric cylinders. The first robot was tested with a traditionally inverted tail, wherein the robot body is forced through the core of its body. In the second case, the robot body was first tightly rolled up, and the remaining 15 cm were inverted over the rolled material. As the body was inflated, the roll unwound at the tip of the device as it grew.

The traditional vine robot exhibited an exponential increase in growth pressure and burst after three complete revolutions, while the rolled tail robot extended through its full length to six revolutions with near constant pressure. It must be noted, however, that having the rolled tail ride along at the tip affects the dynamics of tip eversion and growth, thereby increasing the pressure required to do so. These results are exciting, and

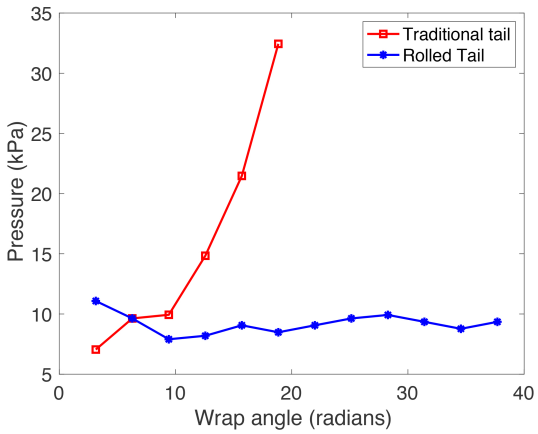

Figure 2.11: Wrap test showing effect of reduced internal tail length.

continued exploration can commence in this area.

2.6 Discussion and Conclusion

Vine robots are an exciting new paradigm in the field of soft robotics, as their unique growth modality opens the door to a wide array of applications. The aim of this work was to better understand their various passive behaviors and lay a foundation upon which future work towards active and autonomous operation and control can be built.

The characterization of the two buckling conditions, as well as the effects of scale, compliance, and capstan friction elimination will allow for more than traversal pressure prediction - it will inform the design as these robots are deployed across the applications introduced in Section 2.2. Further, the fundamental understanding of the forces at play in creating body deflections offers insight into design requirements for creating mechanical components capable of manipulating, articulating, and shape locking these robots, from which unique active/passive hybrid system can be designed.

While our initial results are promising for predicting the macroscopic behavior of these robots in constrained environments, the model presented fails to capture some modes,

such as the coupling between buckles in close proximity. Future investigations can be conducted to refine our generalized model to capture these behaviors. Further, to date the working fluid examined has been exclusively air, and the question of using water to drive growth is another open topic for inquiry.

In this work, we presented a mathematical model of the interaction between a soft, tip-extending vine robot and its environment. Our experimental results confirm this model and show that it can predict the effect of environmental contact forces on the behavior of the robot. Importantly, the model can inform the design of robots tailored to specific environments. The model suggests that increasing membrane compliance, containing the tail in the tip, and intelligently choosing the diameter of the robot will allow it to most easily navigate constrained environments. This work contributes to the field by providing a more fundamental and informed starting point for the development of new soft, tip-extending vine robots for navigating difficult environments with varied requirements, ranging from navigating through rubble during search and rescue missions to more delicate applications such as medical endoscopy.

2.7 Acknowledgment

Thank you to Laura H. Blumenschein for her helpful advice.

Chapter 3

Design: applying modeling insights towards novel capabilities

As a direct consequence of the findings in Chapter 2, we sought to develop technical components inspired by the design insights uncovered in that effort – namely, overcoming the length limit of base-station-controlled vine robots traversing tortuous paths. At approximately the same time, I was considering ways to overcome some of the workspace limitations inherent to constant-curvature vine robots. This two-pronged design inspiration led me to the so-called steering-reeling mechanism (SRM) design, that enables tip-based length control and localized deformation control. In cases such as search and rescue, where one might encounter a combination of constrained and unconstrained paths in close proximity, this sort of design overcomes some of the limitations in traditional constructions.

3.1 Background

Traditionally, soft robotics has sought to produce the "fully soft" system, but as perspectives such as those in [11], softness for softness' sake is likely an inappropriate design constraint. For instance, while the fully-soft arm such as in [66,67] may have utility in environments wherein contact forces need to be controlled, they sacrifice dexterity in terms of workspace access. Simultaneously, the base-located retraction present in [59,68] necessarily requires all curvature the body experiences to result in exponential capstan friction that inhibits growth length in tortuous paths. Thus, the SRM was born: a single, rigid, mechanical system that lives inside the vine robot body and enables both tip-based length control (via the internal reeling mechanism), and localized trajectory control (via the internal steering mechanism). This hybrid system, while a divergence from the "fully soft" ethos, provided novel capabilities for vine robots inspired by the mathematical modeling done previously.

3.1.1 Abstract

Continuum robots have high degrees of freedom and the ability to safely move in constrained environments. One class of soft continuum robot is the "vine" robot. This type of robot extends from its tip by everting or unfurling new material, driven by internal body pressure. Most vine robot examples store new body material in a reel at their base, passing it through the core of the robot to the tip, and like many continuum robots, steer by selectively lengthening or shortening one side of the body. While this approach to steering and material storage lends itself to a fully soft device, it has three key limitations: (i) internal friction of material passing through the core of the robot limits its length in tortuous paths, (ii) body buckling as the robot's body material is re-spooled at the base can prevent retraction, and (iii) constant curvature steering limits the robot's poses and object approach angles in a given workspace. This work presents a hybrid soft-rigid robotic system comprising a soft vine robot body and a rigid, mobile, internal steering-reeling mechanism (SRM); this SRM is equipped with a reel for material storage, a bending actuator for steering, and is capable of actuating the robot at any point along its length. This hybrid configuration increases reach along tortuous paths, allows retraction, and increases the workspace. We describe the motivation for the device, generate its mathematical models, present its methods of operation, and verify experimentally the models we developed and the performance improvements over previous vine robots.

3.2 Introduction

The field of robotics began with rigid robots, whose powerful and precise movements make them invaluable for manufacturing [38,48]. However, unstructured, sensitive environments such as Fukushima can provide serious challenges [69]. Soft robots' ability to deform and adapt to their environment offer an alternative approach to navigating

complex real-world environments.

One such variety, "vine" robots, are of particular interest for negotiating complex environments. First presented in 2003, skin-eversion robots have taken many forms [25,49–52]. Our work is inspired by a more recent design by [26], capable of navigating cluttered environments autonomously [46], or via teleoperation [57], burrowing through loose media [58], creating deployable structures [70], and achieving complex shapes through intelligent design [71]. Made of a thin-walled membrane inverted inside itself, these robots "grow" when inflated, passing new material through the body to emerge at the tip to achieve extension. Their bodies do not move relative to their surroundings, reducing environmental interaction forces, making them promising candidates for a variety of applications from medical to search and rescue. However, there are three key limitations to many of the current vine robots that we seek to address in this work.

First, internal friction of body material passing through the core of the robot grows exponentially with the total path angle, limiting the robot's length in tortuous paths [42,47]. Since most vine robots store their body material in a reel at the base [59,68,72], body material has to pass through the entire length of the body from the base to the tip, accumulating friction along the way.

Second, while simply re-spooling material onto the reel at the base can retract the body, the tension in the internal body material causes buckling for long bodies. Ref. [68] identified that this behavior can be prevented by reducing the tension in the internal body material via a tip-based, tethered motor; while retraction is greatly improved, the length restrictions imposed by the internal body material and additional wiring still limit the robot's achievable length.

Finally, constant curvature steering limits the possible poses and tip orientations of the robot, restricting its reachable workspace. Most vine robots have been steered by selectively lengthening or shortening one side of the robot via tendons or artificial

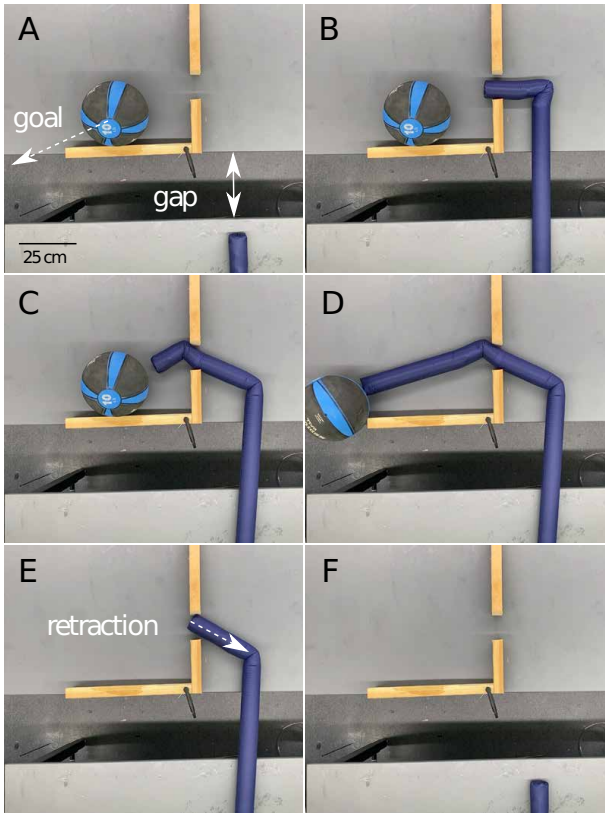

Figure 3.1: Overhead view of the presented robot (A) navigating across a gap wider than the internal mechanism (SRM) is long, (B) turning acutely into an opening, (C) turning again to steer at a target object (4.5 kg exercise ball), (D) pushing the ball off of the table, and (E-F) retracting back to its starting location.

muscles [67,71,73,74]. While this allows entirely soft devices, it restricts turning to approximately constant curvature deformation, reducing its ability to navigate some obstacles. A number of attempts have been made to overcome this limitation, such as tendon actuation coupled with pneumatic shape locking [67]; discrete, reversible body stiffness modulation [72] and mechanical interlocks [26]; and active and programmable heat sealing [75].

What follows is a description of our design concept to address these limitations, a mathematical description of the various behaviors of this device, and the details of our design informed by this modeling. We then verify the models, and present experimental data showing an increase in tortuous path length, an integrated retraction ability, and an

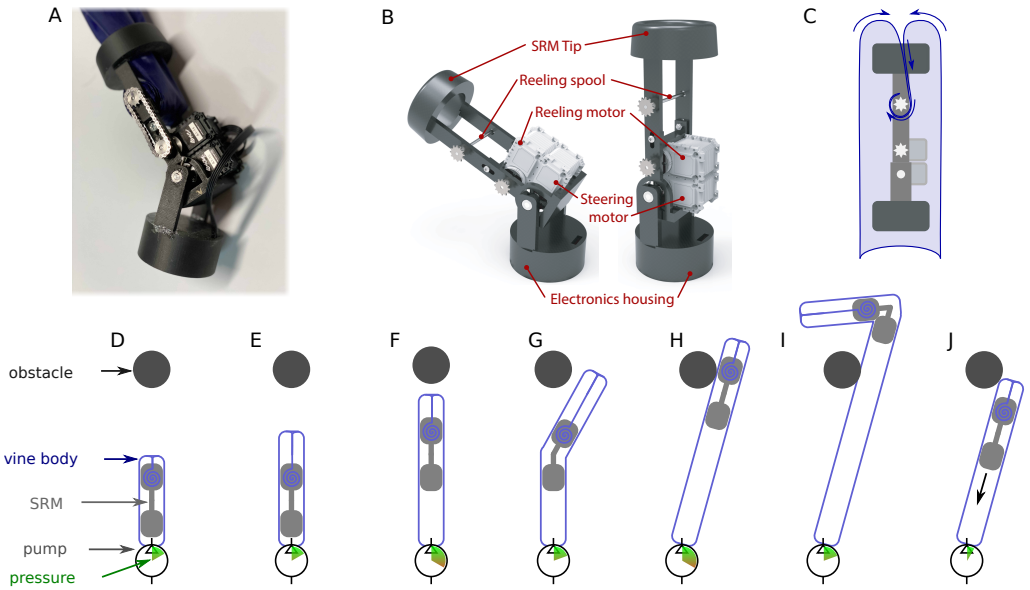

Figure 3.2: The SRM (A) controls both the steering and reeling of the external vine robot. Internal actuators enable both steering (B) and length control by reeling (C). The SRM (D) extends the tip of the robot by unreeling new body material (E) while the internal pressure (shown on gauge at bottom) is low. To move the SRM forward to a desired point, the reel is locked and the body pressure is increased so that the friction between the SRM and the robot body is overcome. This allows the everting body to pull the SRM towards the tip of the robot (F). The SRM then bends to steer around an obstacle and unreels more material (G). The reel is again locked and pressure increased to pull the SRM towards the tip of the robot (H), where it makes a new bend (I). It then retracts by reeling in vine body material (J) while it is located at the tip.

expanded workspace. We conclude by discussing the potential impacts and future work planned for this new design.

3.3 Concept

To address length, buckling, and steering limitations, we present a hybrid soft-rigid robotic system (Fig. 3.1 and 3.2) comprising a soft vine robot body and a rigid, mobile, internal steering-reeling mechanism (SRM). The SRM is designed to fit inside the vine robot body with sufficient radial clearance to easily allow for sliding and for air to inflate the entire vine robot body, and comprises two segments connected by a revolute joint

that can control the vine robot body in two ways. First, it controls robot length by spooling in or out body material that is connected to a reel on the forward or distal segment of the SRM. The proximal tip of the vine robot body is reeled on the SRM spool after passing through the SRM tip as shown in Fig. 3.2A. The remainder of the body is everted around the exterior of the SRM as shown in Fig. 3.2C. Second, it controls direction by rotating the two sections of the SRM relative to one another to cause a bend in the robot body. The steering motor can bend and hold the robot 120° in both directions from the nominal, straight state. This allows point deflections at any point along the robot, creating two arbitrary length segments provided the overall body length constraints are satisfied.

Operation of length and direction control with the SRM is as follows. As shown in Fig. 3.2D, when the internal pressure of the vine robot is low and the spool is fixed, the SRM remains in place due to a small amount of friction between the SRM and the inside of the body. As the spool unreels material (Fig. 3.2E), the robot extends while the SRM remains stationary. When the internal body pressure is increased beyond a threshold pressure, the body everts and pulls the SRM forward (Fig. 3.2F). The SRM then uses the steering motor to create a bend in the body and steer around an obstacle (Fig. 3.2G). Pressure is reduced to keep the SRM in place by friction while the spool is unreeled to lengthen past the obstacle. To advance the SRM again, the reel is locked and pressure is increased to overcome friction, allowing body eversion to pull the SRM toward the tip (Fig. 3.2H). Once the SRM is at a desired location, another turn can be made (Fig. 3.2I). Finally, the robot can retract by reeling in body material while body pressure is low (Fig. 3.2J). Via a series of reeling and unreeling behaviors with high or low pressures, it is possible to achieve any length robot body with the SRM positioned at any location, and from this location it can retract completely to the base by continuously reeling in body material.

The proposed hybrid vine robot concept allows for: i) greater lengths when growing through tortuous paths—total angle of path is no longer bounded due to tail friction, and instead by the length of the robot itself, (ii) retraction regardless of length—the robot can retract at any length when the SRM is moved to the tip, and (iii) a larger workspace—orientation at a given point grows from a single angle for previous designs to a continuous range of up to 115 degrees.

3.4 Modeling

This section introduces the mathematics that represent the individual elements of the presented concept in comparison to previous vine robots. Our modeling is broken down into three sections: length limitations, retraction, and workspace analysis. This modeling is used to analyze the elements present in Section 3.5, Design, and verified experimentally in Section 3.6, Results.

3.4.1 Length Limitations

The length of a vine robot is limited by the length of the body material on its spool and internal friction. Robots that store body material on a reel at their base pull new material through their body to extend. In straight growth, friction is relatively low, however it increases exponentially with total curvature. This friction, known as capstan friction, is described in [47] as

$$F_{int} = \sum_{i} C e^{\mu_c \theta_i}, \tag{3.1}$$

where C is a configuration tension, μ_c is the coefficient of friction in curved growth, and θ_i is the angle of the i^{th} bend. Due to is exponential nature, this friction is very limiting in

tortuous paths. The presented concept circumvents this limit by spooling body material at the tip, but is instead bounded by the amount of material that can be fit on the SRM for a given robot diameter.

To understand this volume limitation, we model the spooled tail as a simple Archimedes spiral with a constant rate of radial expansion, described by

$$r = \alpha a + b, \tag{3.2}$$

where r is the distance from the center of the spiral to its outermost edge, α is the total swept angle of the spiral, a is a constant such that $2\pi a$ is the separation between two layers of the spiral (i.e. folded tail material thickness), and b is the spiral offset (i.e. the radius of the spooling bar). To understand the limits on robot length, L, we solve for the arc length of the spiral in terms of r and the parameters a and b, denoted $\alpha(r)$, with

$$L = \int_{b}^{r_{max}} \sqrt{(\alpha(r))^2 + \left(\frac{d\alpha}{dr}\right)^2}\, dr \tag{3.3}$$

Using the substitution $u = r - b$, this integral is solved for the maximum length of the robot, L_{max}, as

$$L_{max} = \frac{1}{a}\left[\frac{(r_{max}-b)}{2}\sqrt{(r_{max}-b)^2+1} + \frac{1}{2}\ln\left(r_{max} - b + \sqrt{(r_{max}-b)^2+1}\right)\right] \tag{3.4}$$

where r_{max} is the radius of the robot body. In our robot, b is much smaller than αa, meaning the second term of (3.2) will be negligible. We note that (3.4) shows that L grows with the square of r, yielding nonlinear length increases per unit increase in diameter. As well, the same formulation given in (3.4) can be applied in terms of α,

such that the length of the robot can be controlled in closed loop with a retraction motor encoder.

3.4.2 Retraction, Steering, and SRM Movement

In this section, we first describe the forces required to retract and steer such that we develop the parameters to guide our choice of reeling and steering motors, as described in Section 3.5. Then, we describe the conditions that determine whether the SRM moves or remains stationary.

Force for Retraction

Past retraction work [68] has shown that the force required to invert a vine robot is equal to one half the force produced by pressurization plus a zero pressure offset term (a material-dependent constant that represents the force required to invert or evert material, independent of pressure). Since this new design incorporates an internal component with mass, we modify the formulation given in [68] to incorporate the friction between the robot body and the SRM, becoming

$$F_R \leq \frac{PA}{2} + F_I + F_{fric} \tag{3.5}$$

where P is the internal pressure, A the cross sectional area, F_I the material dependent constant, and F_{fric} the friction between the SRM and the robot body. Equation (3.5) is an inequality due to the fact that friction may or may not be present, depending on the retraction condition (the SRM may not be retracting from the tip, and may not be moving relative to the robot body).

Using relationships (3.2) and (3.4) to determine the maximum radius of the spool, r_{max}, for a given robot length, we can use (3.5) to predict the theoretical maximum

torque, τ_R, required to retract the robot, which occurs when the spool is at its largest and the SRM is at the tip. Assuming orthogonality at the point of spooling, we have

$$\tau_R = r_{max} \times F_R = \left(\frac{1}{2} P_{max} A + F_I + F_{fric}\right) r_{max}, \tag{3.6}$$

where P_{max} is the maximum pressure commanded to the robot. This model helps in sizing the reeling motor.

Limits on Revolute Joint

Similar to Section 3.4.2, we need to understand the forces involved, here for bending of the body, to develop the specifications for the bending motor. Previous work [59,60] showed that the internal restoring moment, M_{int} produced by an inflatable beam under transverse loading is

$$M_{int} = \pi P r^3, \tag{3.7}$$

where P is internal pressure and r is the beam radius. The torque requirement for the bending motor is thus

$$\tau_B \geq M_{int,max} = \pi P_{max} r^3 \tag{3.8}$$

where τ_B is the minimum bending motor torque for a maximum operational pressure P_{max}. We see in (3.7) that the internal moment is nominally independent of deflection. This implies that so long as the motor torque exceeds the minimum specification given in (3.8), the revolute joint can achieve any bending angles the geometry of the SRM allows.

SRM Movement

Next, we describe the relationships that govern when the SRM moves versus remains stationary (shown in Fig. 3.2). It is the balance of three primary forces that determines whether the SRM moves: the tension force on the tail $PA/2$, the inversion/eversion force F_I, and the friction force between the SRM and the inside of the body F_{fric}. The last force can vary depending on the configuration of the SRM, where a straight SRM will have a lower friction force than a bent one. There are two common ways these forces relate, either

$$\frac{PA}{2} > F_{fric} + F_I, \quad \text{or} \quad \frac{PA}{2} < F_{fric} - F_I. \tag{3.9}$$

In the first case, the pressure is relatively high, and the body will evert, pulling the SRM with it. In the second case, the pressure is relatively low, and the SRM will stay in place and can retract the body if the tail is reeled. There is a third, less common case for moderate pressures, in which $PA/2$ is within $\pm F_I$ of F_{fric}. In this case, retraction of the motor results in motion of the SRM forward, but no retraction of the body.

3.4.3 Workspace Analysis

In this section, we explore the two-dimensional space that this robot can achieve when using the proposed actuation modality, and compare and contrast that to the workspace of many previous vine robots that are constrained to a constant curvature of the body.

To date, vine robots have often been actuated by pneumatic artificial muscles (PAMs) or motor-driven tendons, resulting in continuous, distributed deformation along the length of the body. Significant work has been focused on modeling the kinematics of these robots, such as [67,73,74,76]. Most notably, for a given position in the workspace, these devices are limited to only one approach orientation. This section outlines how the proposed design improves upon this access.

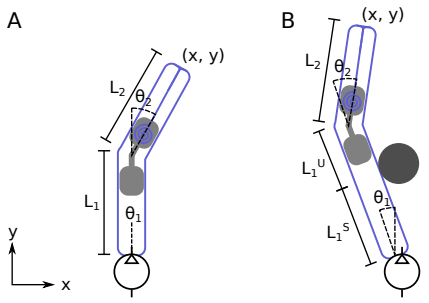

Figure 3.3: Geometry of SRM-robot system with (A) and without (B) an obstacle interaction.

Obstacle-free PRP Kinematics

In this investigation, the kinematics are described by a modified prismatic-revolute-prismatic (PRP) planar rigid robot, as shown in Fig. 3.3. Essentially, our robot can extend straight from its base, bend at the current location of the SRM, and extend straight from the mechanism to its tip. Williams and Shelley [77] provide the kinematics for this class of planar manipulators, and show the PRP combination to be simply described by

$$E = \begin{bmatrix} x \\ y \end{bmatrix} = A + L_1 e^{j\theta_1} + L_2 e^{j\theta_2}, \tag{3.10}$$

where (x, y) represents the global frame position, $\phi = \theta_1 + \theta_2$ represents the tip orientation in the base frame, A is a global position offset, L_i is the length of the ith segment, and θ_i its the orientation in the ith frame where $i = 1, 2$.

We note that, for our robot, θ_1 will be zero when there are no obstacles in the workspace (Fig. 3.3A). With this θ_1 known, θ_2 is simply the desired tip orientation or approach angle, ϕ.

The lengths L_1 and L_2 are subject to constraints determined by the length of the overall robot, the SRM design, and the robot configuration. Fig. 3.3 shows the kinematic quantities described in this section, and gives insight into the length constraint. In the zero or one obstacle case, this constraint is described by $L_1 \in [0, L_{max}]$, and $L_2 \in$

$[0, (L_{max} - L_1)/2]$ such that $L_1 + L_2 \leq L_{max}\, \forall L_1, L_2$. This is due to the fact that at least one half the remaining total body length must be internal to the vine robot to connect to the SRM. That is, for a particular L_1, the remaining body material is $L_{max} - L_1$, but this material must be split between the everted, external body, and the internal material attached to the SRM, yielding the constraint $L_2 \leq (L_{max} - L_1)/2$.

N Obstacle PRP Kinematics

If the robot instead grows around multiple obstacles successively, the analysis can be extended to a multi-link robot. Generally, the robot can be described as functionally having $n+1$ prismatic links, where n is the number of obstacles with which it interacts. In these cases, the kinematics given in (3.10) can be extended with n links of known lengths and angles, and the length constraint given above can also be generalized by cascading the above relationship into $n+1$ segments.

When a single obstacle support occurs, θ_1 is known and constant. We then cut L_1 into the supported length and the unsupported length, denoted L_1^s and L_1^u, respectively, with $L_1 = L_1^s + L_1^u$. The length constraint then becomes $L_1 \in [L_1^s, L_{max}]$ and $L_2 \in [0, (L_{max} - L_1)/2]$ (Fig 3.3B). For n obstacles, we recognize θ_i, $i \in [1, n]$, is known and constant, and that each obstacle interaction defines the length of that link to be L_i^s, $i \in [1, n-1]$ (because the uncontrolled links between obstacles will take the shortest possible path). Thus, we can extend the length constraint to become $L_n \in [L_n^s + \sum_{i=1}^{n-1} L_i, L_{max}]$, $L_{n+1} \in [0, (L_{max} - L_n)/2]$. Once each prismatic joint length and its associated angle is defined, the generalized kinematics become

$$E = \begin{bmatrix} x \\ y \end{bmatrix} = A + \sum_{i=1}^{n} L_i^s e^{j\theta_i} + L_{n+1} e^{j\theta_{n+1}}. \tag{3.11}$$

It is important to note here that the robot remains fully defined, as each object

interaction in a given series can occur at only one angle in the global frame, with the lengths of each supported link known.

Reachable Workspace

Finally, (3.11) allows us to determine the reachable workspace. The nominal workspace (i.e. with no obstacles) can be described by $\mathcal{W}_\circ = \{(x,y)|\theta_1 = 0, \theta_2 \in \Theta_2, L_1 + L_2 \leq L_{max}\}$, where Θ_2 is set by the robot joint limits. When obstacle support occurs, we utilize the length and angle constraints given in the previous section. From this formulation we can generalize the obstacle interaction subspaces as $\mathcal{W}_i = \{(x,y)|\theta_i \in \Theta_i, \theta_{i+1} \in \Theta_{i+1}, \sum_i^{i+1} L_i \leq L_{max}\}$, where Θ_i is the obstacle support angle in the local frame and Θ_{i+1} defines the range of joint angles. Finally, we can describe the total workspace, $\mathcal{W}_t$, as $\mathcal{W}_t = \mathcal{W}_\circ \bigcup_{i=1}^{n} \mathcal{W}_i$.

Fig. 3.4A shows a representative workspace with no obstacles present. The limits of the motion of the SRM's bending actuator are set to $\pm 105^o$, according to the design of the device, and the total length of the robot material is set to unity with L_i described as a percentage of total length. Interestingly, the further distal the SRM and thus the reel of material, the further the reach of the robot, as described by the length relationships above. That is, in the case where $L_1 = 0$ (green), the robot body material must extend from the reel internally to the tip and back to the base externally. However, for the case where $L_1 = 66$, the internal material only needs to reach from the SRM to the tip, as depicted in Fig. 3.3. Fig. 3.4B shows how the workspace changes when the robot interacts with an obstacle. Since the robot body is able to anchor on an obstacle, the SRM is able to travel forward while the base angle, θ_1, remains locked. This means the robot can reach further in the direction beyond the obstacle than when the obstacle was not present.

The robot can also achieve new approach angles when anchored to the obstacle. Fig.

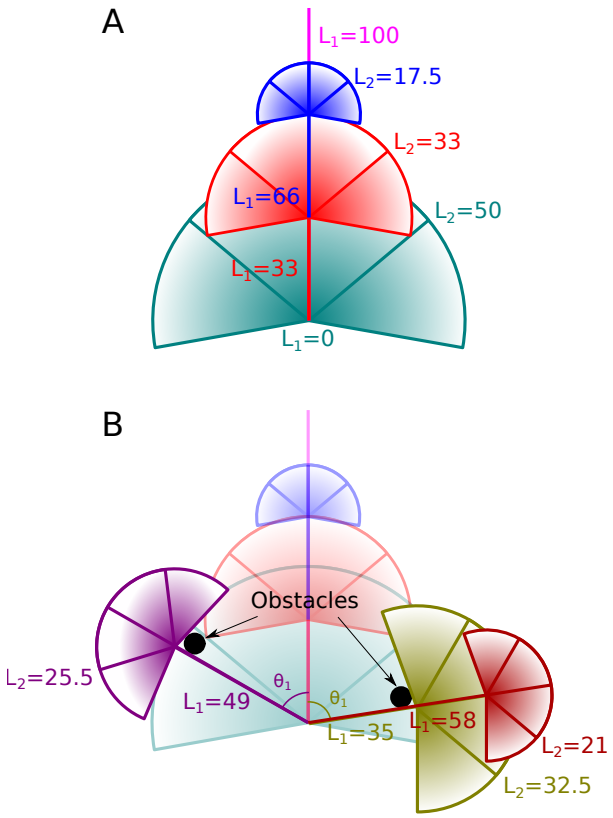

Figure 3.4: Theoretical workspace for the robot. While the robot's actual length is 2.4 m, lengths here are represented as relative percentages. (A) With no obstacles present, the robot is able to grow forward and make a single turn at various lengths, L_1. The behavior is similar to a PRP planar manipulator. (B) With the addition of obstacles, the robot can hold a new base angle, θ_1, to open up new tip orientations in the workspace.

3.5 presents the range of tip orientations at each point within the workspace for the case of one obstacle. While many areas of the workspace can be reached with over ninety degrees of tip orientations for our robot, we note that a constant curvature robot can only reach most areas with a single approach angle, besides near the obstacle, where two discrete angles are possible [73].

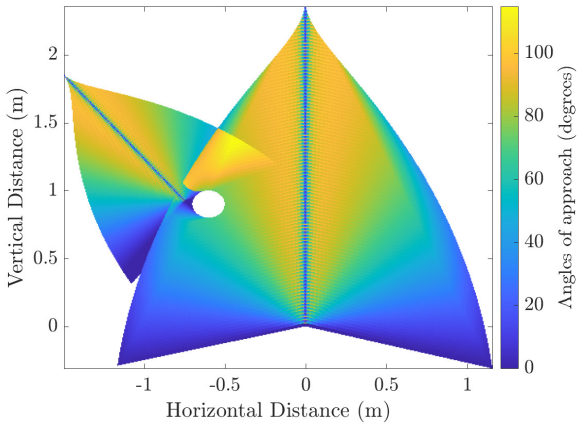

Figure 3.5: Theoretical heatmap of tip orientations for a workspace that includes a single obstacle.

3.5 Robot Design

3.5.1 Parameter Selection and Scaling

To chose the parameters for our robot, we begin by choosing an arbitrary desired length, which we set to 2.4 m. From this, we used (3.4) to determine that the maximum spool diameter is required to be 42 mm to hold this amount of material. This recognizes that the tail material must fold at least once to fit inside the robot because the half circumference width of a “lay flat" state is wider than the diameter. After including the dimensions of the drivetrain and SRM frame, we found that the minimum robot diameter is 68mm. This in turn allowed us to use (3.6) to calculate the required reeling motor torque to be 0.30 Nm using the value of F_{fric} reported in Section 3.6.3. We then used (3.8) to calculate the required steering motor torque to be 0.84 Nm.

More generally, we describe how these parameters scale. First, we note that from (3.4) we know that the maximum length the robot can achieve grows as the square of the spool radius. Since the spool must fit inside the robot, this also means length grows as the square of robot radius. Next, we note that the required motor torque to retract the robot body grows as the cube of the radius (3.6), and the motor torque required

to steer the body also scales as the cube of radius (3.8). Since motor torque scales with volume ($\sim r^3$), these three scaling laws suggest that a larger robot will be able to grow proportionally longer, and that the required relative size of the internal motors will remain the same regardless of scale.

3.5.2 Fabrication

With these specifications, we built a hybrid robot, composed of two parts, the soft robot skin and the rigid SRM that rides inside the robot skin as shown in Fig. 3.2.

The skin is made of a 71 μm thick silicone-urethane impregnated ripstop nylon fabric (Rockywoods Fabric) tube with an 75 mm diameter, and 2.5 m length. The tube is made by from a strip of fabric using a lap joint, bonded with room temperature vulcanizing silicone adhesive (Smooth-on Silpoxy) as in [39]. The 70 mm diameter SRM is made of two 3D printed Markforged Oynx (chopped carbon fiber-impregnated nylon filament) frames connected by an actuated hinge joint. The 150 mm long distal segment contains a reel of up to 3m of vine robot skin and the bending mechanism, while the 80 mm long proximal segment houses the batteries and wireless transmitter; when assembled, the entire SRM is 215mm long. The vine body material reel is a 3mm diameter steel rod mounted to the frame perpendicular to the length of the robot body. Given the required torque, we chose an XYZrobot Smart Servo a1-16 motor with a rated torque of 2.5 Nm; its output drives the reel via a small steel chain. The joint of the robot is rotated by a second, inline XYZrobot Smart Servo a1-16 motor, also rated to 2.5 Nm, and the joint can achieve rotations up to 120° in the positive right-hand direction, and 105° in the negative right-hand direction (with the difference due to geometrical constraints imposed by the actuator's construction). The motors are powered by three 500mAh, 3.7V lithium-polymer batteries, controlled by an Adafruit Feather M0 interfaced with

915 MHz radio. When fully assembled SRM has a mass of 337.5g.

3.6 Results

Here we discuss testing of length limitations and the reachable workspace of our robot.

3.6.1 Length Limitations

We first present test results comparing the performance of our robot to a vine robot with the reel at the base on a tortuous path. Second, we test our model of the relationship among spool angle, spooled material radius, and robot length.

Increased Length Along Tortuous Paths

From (3.1), for previous vine robot designs with the reel in the base, we expect the internal pressure to increase exponentially with the total angle of a tortuous path, as the tail pulls through the inside the curved body. In contrast, for the presented robot, we predict a near constant pressure across length. To test this, we measured the pressure to grow for a robot in a serpentine path, constrained by a series of pegs in two rows, 30 cm apart with a peg spacing of 28 cm. Two robots of roughly equal diameter—one with base spooling, one with an SRM—were tested. Each robot was placed in the test set up around a given number of pegs, then the pressure was increased until growth occurred. To bend around the first peg required a turn of 90°, and an additional 180° for every subsequent peg, up to a total path angle of 630°. The test was repeated five times with each robot design. The results presented in Fig. 3.6 show that at a 0° path angle, the pressure required to grow the vine robot with the reel at its base is similar, or slightly lower, than required for the SRM. As path angle increases, the pressure to grow with the SRM remains constant, but increases exponentially for the robot with the reel at

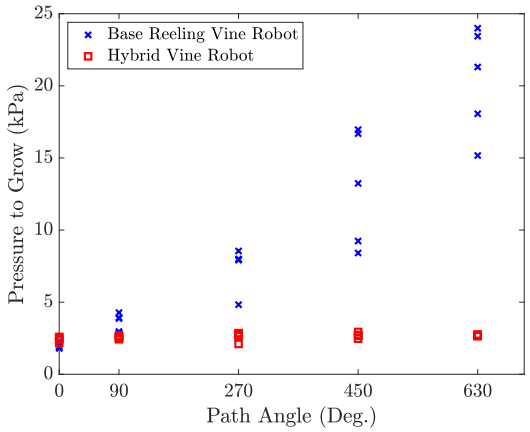

Figure 3.6: Pressure required to grow through tortuous paths. With the body material reeled at the base, as is common in previous vine robots, the pressure to grow increases with path angle. In contrast, for the presented robot with the body material reeled in the SRM, the pressure to grow remains roughly constant when the SRM is near the tip.

its base, as expected by (3.1). Thus, the presented design is only length-limited by the constraints imposed in Section 3.4.1.

3.6.2 Spool Geometry

First, we sought to determine the value of a in (3.2), which is nominally the thickness of material in each wrap of the tail divided by 2π. Since the flat tail material is wider than the diameter of the robot (equal to half the robot circumference), it must fold at least once to fit on the reel, meaning a must be at least $4t/2\pi$, with t being the thickness of one layer of material. In reality, a will be larger than this, due to wrinkling and air gaps. To determine a experimentally, we reeled the tail while measuring the angle of the reel and its radius (Fig. 3.7). The actual packing density was 57.2% of the theoretical limit.

Second, using the measured a, we compared the predicted length versus spool radius from (3.4) to experimental data (Fig. 3.8). While trends match, the model slightly underestimates the actual length of material on the reel, possibly because the material

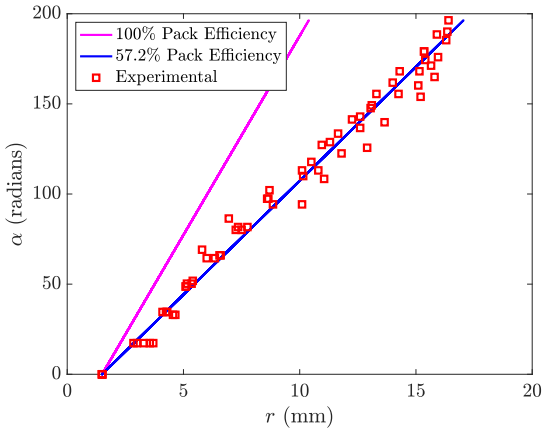

Figure 3.7: Experimental results used to determine the actual value of a for (3.2). A best fit line (blue) suggests that the value of a is approximately 57.2% of the theoretical packing density limit (magenta).

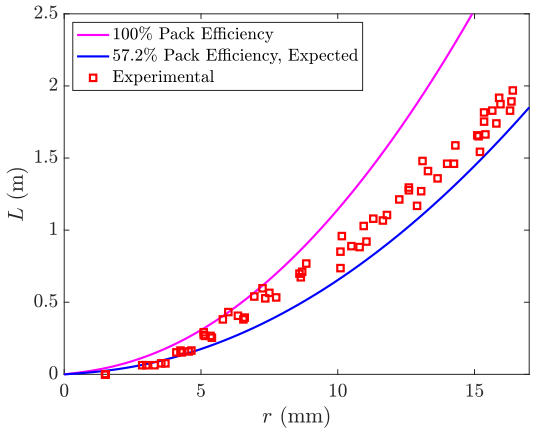

Figure 3.8: Experimental testing of the spiral model (3.4) shown with the expected curve (blue) using the value of a from Fig. 3.7, as well as the theoretical limit with perfect packing.

is not perfectly straight on the reel.

3.6.3 SRM Movement

In this section, we determine the bounds on (3.9) in Section 3.4.2 to understand the expected behavior of the SRM at various pressures. We ran five trials each to determine F_{fric} and F_I, using a Mark-10 100 N push/pull force gauge. To determine F_{fric}, the SRM was detached from the vine robot body and pulled along a strip of body material with

the force gauge just until sliding occurred, with the peak force recorded. The average value was found to be $0.65\,N$, with a standard deviation of $\pm 0.05\,N$. A similar test was conducted to determine F_I; with the tail of the material attached to the force gauge, it was pulled until inversion just began, recording the peak force. The average value was found to be $0.30 \pm 0.05\,N$.

Applying (3.9), we predicted that the SRM would be pulled to the tip at pressures exceeding $0.41\,kPa$. To verify this expectation, tail material was spooled off of the SRM at zero pressure and it was positioned in the center of the robot body. Pressure was slowly increased, and the measurement was recorded when sustained movement was observed. The average pressure across five tests was found to be $0.39 \pm 0.04\,kPa$.

We note that this pressure limitation greatly slows the operation of the device, and future work is planned to incorporate a braking device into the design such that this feature of controllable SRM position and relative motion may be better utilized in the robot's operation.

3.6.4 Workspace

To help verify our model of the robot workspace, we grew the robot in a series of tests while recording position in the plane via an overhead video camera. We first tested reachable workspace with and without obstacles. The results of these experiments are shown in Fig. 3.9. While small discrepancies exist, the expected trends are observed: in the no-obstacle case, lateral reach is reduced as the SRM moves more distally (Fig. 3.9A), and the addition of obstacles extends the workspace in the region beyond the obstacle (Fig. 3.9B). We then tested the range of tip orientations at three target points in the workspace for a single obstacle case, with results shown in Fig. 3.10. Again, the expected trends are observed. Limited tip orientations are found at the extent of

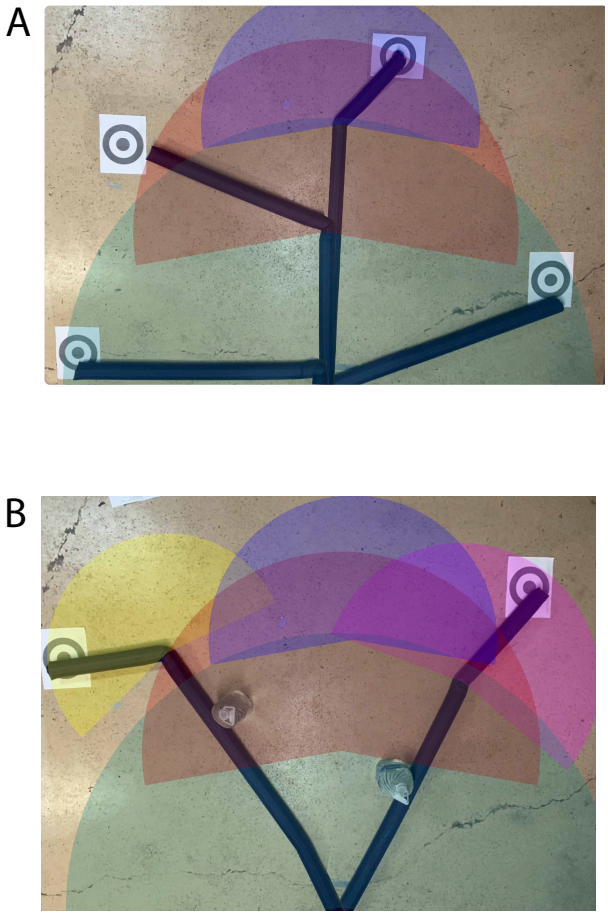

Figure 3.9: Experimental validation of theoretical workspace. (A) No obstacles. (B) With two obstacles. Reachable workspace arcs at each bending position, from (3.11) are overlaid.

the workspace (bottom right target), close to 80 degrees of tip orientations are available away from the obstacle (leftmost target), and almost 130 degrees are achievable near the obstacle (middle target). While the model presented in Fig. 3.5 predicts approximately 110°, accounting for the asymmetry in the actual device in the model yields exactly the results observed.

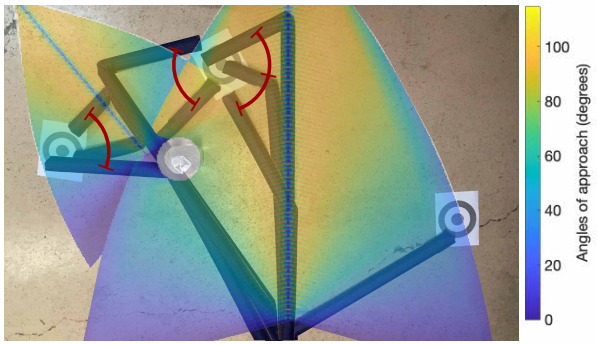

Figure 3.10: Experimental validation of theoretically achievable tip orientations when there is a single obstacle in the workspace. A heat map of achievable tip orientations as modeled in Fig. 3.5 is overlaid.

3.7 Discussion and Conclusion

We have presented a hybrid soft-rigid robot, comprising a compliant vine robot and a rigid internal steering and reeling mechanism (SRM). This new design overcomes three key limitations of past constant curvature vine robots with base-mounted reels: length restrictions due to internal friction, retraction bounds on free robot lengths and poses, and workspace limitations due to constant curvature kinematics. We have shown that incorporating an SRM in a vine robot eliminates length restrictions caused by friction, enables retraction in any pose, and increases the achievable angles of approach by orders of magnitude.

These improvements may advance the performance of vine robots in real-world applications. For example, the improved workspace could enable robots to better navigate difficult archaeology sites [57], aircraft interiors, or nuclear facilities. Reduced internal friction by tip spooling could also enable vine robots to access more tortuous paths, such as the small intestine, machinery, or animal burrows. The SRM however, reduces growth speed and limits the vine robot's ability to squeeze through gaps smaller than the diameter of the SRM. The additional weight also makes it more difficult to span gaps.

The development of the SRM offers many opportunities for future work. Adding

an additional bending actuator in the same SRM would enable three dimensional steering. Further, with some modification, additional SRMs could be incorporated to create multiple bends in multiple planes at multiple locations along the body. The thoughtful introduction of an end effector such as [26,57,78] would also expand the robot's usefulness. In addition, exploring the limits of down scaling the tip spool design would be useful for small-scale applications.

Chapter 4

Data-Driven Modeling, and Control: breakthrough performance of a soft robot arm

In late 2019 I was working to understand the dynamic model of a soft robot, inspired by the early work of Nathaniel Agharese at Stanford that culminated in [79], that might enable the closed-loop control of some of the concepts that were under development. However, after my experience with closed-form modeling in Chapter 2, we began to realize that pen-and-paper modeling of soft robots was perhaps a sub-par method to enable control of these sytems in both autonomous and semi-autonomous capacities. Supported by some collaborators at UCSB, we decided to pursue a data-driven approach instead of closed-form.

This effort resulted in compelling findings over a multi-year period. First, we showed that even in open-loop, the Koopman method could provide compelling results. Specifically, we realized that time-delay KOT, even with significantly reduced model order, was a candidate method for extending the capabilities of soft robotics into new domains (Sec. 4.2). This inspired us to build a closed-loop system that sought to examine the limits of what this approach could enable. The end result was a highly data-efficient algorithm that implemented closed loop control with only a linear-quadratic regulator (LQR) architecture, simultaneously performing on two arms with notable morphological differences, and enabling such dynamic tasks as catching and throwing a ball, as shown in Sec. 4.3.

4.1 Background

Beginning my collaboration with Drs. Michael Banks and Igor Mezić, we collectively sought to test the capability limits of the burgeoning machine learning method known as Koopman Operator Theory (KOT), in many ways reinvented by Dr. Mezić in [80,81]. This approach had been shown applicable by Bruder et al. in [82–85], but confined to small deflections and in closed loop. In our mind, the most important underlying question

should not be towards the objective of obtaining accurate control, but rather accurate non-linear, data-driven modeling. If proven capable, and if we understood how to best develop such a model, then more advanced control capabilities would be likely unlocked. After constructing the most nonlinear soft arm we could, we showed that time delays as the only observable could capture the dynamics so well, that highly non-linear pose reconstruction could be completed with as few as 7 Koopman modes (essentially, the eigenvectors of the Koopman adjoint).

We then extended this insight into closed-loop control, utilizing a minimized model and a Static Koopman Operator (as described in [86]) to enable LQR control of the previous robot arm, as well as another built for this continuation. Ultimately, we showed, to the best of our knowledge, this architecture produced the first real-time control of inertial soft robot behaviors in the stabilizable subspace (although, Thuruthel et al. [87] showed this control in the reachable worspace previously), among other compelling behaviors.

This chapter synthesizes both works, and thus contains some overlap.

4.2 Early Work

4.2.1 Abstract

Soft robots promise improved safety and capability over rigid robots when deployed in complex, delicate, and dynamic environments. However the infinite degrees of freedom and highly nonlinear dynamics of these systems severely complicate their modeling and control. As a step toward addressing this open challenge, we apply the data-driven, Hankel Dynamic Mode Decomposition (HDMD) with time delay observables to the model identification of a highly inertial, helical soft robotic arm with a high number of under-

actuated degrees of freedom. We further show that Koopman spectral analysis gives us a dimensionally reduced basis of modes which decreases computational complexity without sacrificing predictive power.

4.2.2 Introduction

While soft robotics has garnered significant attention in the past decade and grown into a standalone research topic, one of the prevailing challenges the field faces is the problem of modeling and control. The high degrees of freedom, material non-linearity, underactuation, and inherent hysteresis of many of these technologies has precluded the development of closed form, dynamic models that easily lend themselves to traditional control strategies [8,38,48]. Instead, a variety of methods have been introduced in an attempt to address this challenge.

A majority of investigations to this end have relied on simplifying assumptions, such as the (piecewise) constant curvature ((P)CC) approach, as found in for example [67,73,74, 88–90]. Most of these approaches focus on developing mappings from the actuator space (actuator pressure, tendon tension) to the configuration space (curvature, arc length) and finally to the task space (euclidean position and angle). While this approach is macroscopically effective at predicting general deformations, it fails to adequately capture the time evolution of relevant quantities. As such, others have sought to build closed-form dynamic models, compensated with controllers based on feedback linearization [91], sliding mode control [92], and domain restriction [93]. However, due to the infinite degrees of freedom of these systems, closed form models are inherently inaccurate. Moreover, the intrinsic non-linearity often ensures control systems be domain restricted or themselves non-linear.

Owing to these difficulties, a number of groups have turned to data-driven approaches

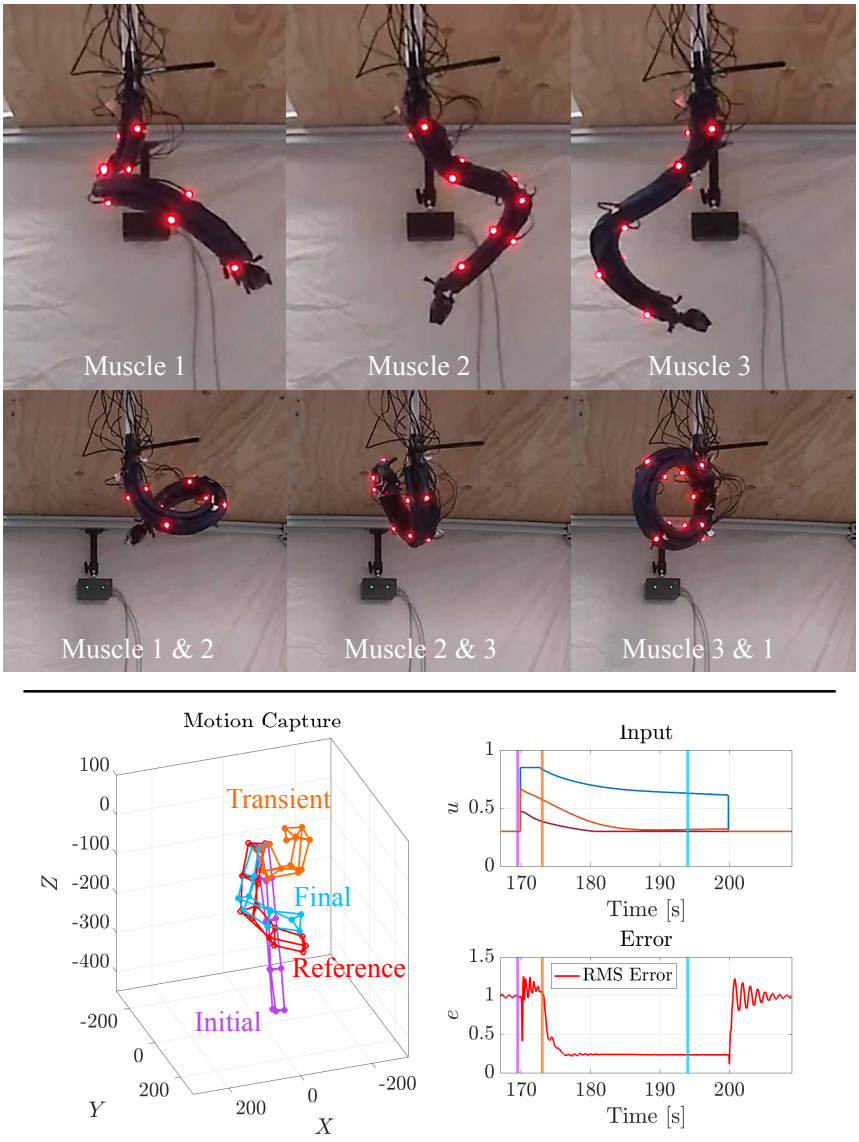

Figure 4.1: *Top:* The steady state pose of the helically actuated, inertial soft arm with an input to individual and pairs of lengthwise artificial muscles. *Bottom:* With a linear model constructed via data-driven, Koopman operator theoretic Hankel Dynamic Mode Decomposition (HDMD) and reduced in dimensionality to $n = 35$ using Koopman mode analysis, we use the Linear Quadratic Regulator (LQR) optimal control algorithm to control the robot from an initial position (purple) through a dynamic transient pose (orange) to its final pose (blue), closely aligned with the target position (red). Plots of the commanded inputs and RMS error are shown, at right.

for producing linear system representations. Numerous attempts to apply various machine learning methods span the last decade, as in [94–98], for example. In each of these

investigations, the overarching aim has been to fit a high dimensional linear operator to the input-output dynamics of a soft robot arm. While they have shown much higher efficacy than many of the closed-form approaches above, they yet require immense amounts of data to converge, and their models don't necessarily intuit any physical characteristics of the system. As such, they often produce very large linear systems with limited domains of applicability. To overcome these limitations, a relatively new attention paid to a century-old approach in dynamical systems theory has opened new avenues to accurate, dynamically relevant models. This approach, Koopman Operator Theory (KOT) [99], has been shown to be more effective than other data-driven methods for soft robotic modeling and control [84]. However, KOT applied to soft robotics is still in its infancy and has yet to be utilized to its full theoretical potential.

This work aims to advance the state-of-the-art in KOT applied to soft robotics through the analysis of Koopman modes. We do so by implementing HDMD on a tip-loaded, inertial soft robotic arm exhibiting both bending and twisting (Fig. 4.1). Using the spatial positions of 15 motion tracking points and their time delays as observables, HDMD captures the fundamental physics of our system [100]. KOT enables us to weigh the relative importance of each of the system's fundamental modes to the dynamics we are interested in. We then project the resulting model onto a reduced basis of the most important Koopman modes. This approach enables us to substantially reduce the order of the model without significant loss of controllability. Notably, we do so with no pre-optimization of observables or extensive data postprocessing, and with training data on the order of 10^4 samples.

What follows is a description of our soft robotic arm, an introduction to KOT and the details of our modeling approach, our experimental setup and data acquisition methods, and our results.

4.2.3 Soft Robotic Arm Design

Due to the difficulty of the problem at hand, one approach is to simplify the testbed to simplify the modeling. Instead, to understand the limitations of the KOT based modeling, we sought to produce a difficult-to-analyze soft arm. This manifested in the concurrent objectives of: fast response times, highly non-linear deformation, and a highly inertial and underactuated system.

We created a pneumatic system capable of generating low-latency, agile actuation over a wide range of inputs. This design was fabricated with lightweight 50 micron thick silicone-impregnated ripstop nylon (sil-nylon), and actuated via three lengthwise fabric artificial muscles of the same material, as presented in [39]. The main body was fabricated to a 2 cm diameter using a silicone adhesive (Smooth-On Sil-poxy) with the fiber reinforcement aligned axially. The three 1.25 cm diameter muscles were similarly constructed, however their fiber weave was oriented with a 45° offset with respect to the main body's axial direction. The mass of the arm with three muscles is a mere 12 g. The input valves that supply the air to the muscles were chosen to enable at least 60 L/min of flow at 200 kPa to ensure high power input. Additionally, the exhaust valves through which the air leaves empty to vacuum to increase the speed of the robot.

To achieve a complicated, non-linear actuation pattern, the muscles were axially aligned on the body with a slight offset, varying among the muscles, to produce different helical deformations from each (Fig. 4.1, *Top*) as described in [40]. To achieve extreme curvature, the main body was fixtured to a workbench and the muscles were affixed under pretension.

Finally, to create a highly inertial system with deformations not directly controlled by the muscles, a 40 g mass was adhered to the tip of the robot.

4.2.4 Control System Modeling via Koopman Operator Theory

Much of this process is captured in Sec. 4.3.5, but is repeated here for clarity. The standard method of representing dynamical systems involves defining a state space M with states $x \in M$ that evolve according to the discrete-time dynamical system

$$x^+ = T(x). \tag{4.1}$$

Here T is the possibly nonlinear state transition function $T : M \to M$.

The non-linearity of soft robot dynamics limits the availability of suitable state-space control algorithms. We instead turn to an operator-theoretic perspective of dynamics of observables [99]. Observables are real-valued functions defined on the state space $f : M \to \mathbb{R}$. The set of all possible observables forms a vector space that is usually infinite dimensional. The Koopman operator $\mathcal{K}$ is defined by

$$\mathcal{K}f \coloneqq f \circ T.$$

This operator describes the evolution of observables as the states move along orbits dictated by (4.10). Even though the underlying state space system is nonlinear, the operator $\mathcal{K}$ is linear. The process of approximating this operator with a finite dimensional matrix is described in Section 4.3.5.

We are interested in describing the Koopman operator for systems of the form $x^+ = T(x, u)$ where $u \in \mathcal{U}$ are user specified inputs. We follow the process outlined in [101] to build this generalization. The first step is to define the space of all input sequences $l(\mathcal{U}) = \{(u_i)_{i=0}^{\infty} | u_i \in \mathcal{U}\}$ where $\mathcal{U}$ is the set of admissible inputs. The discrete-time dynamics T now act on the extended state space $S = M \times l(\mathcal{U})$. Given observables

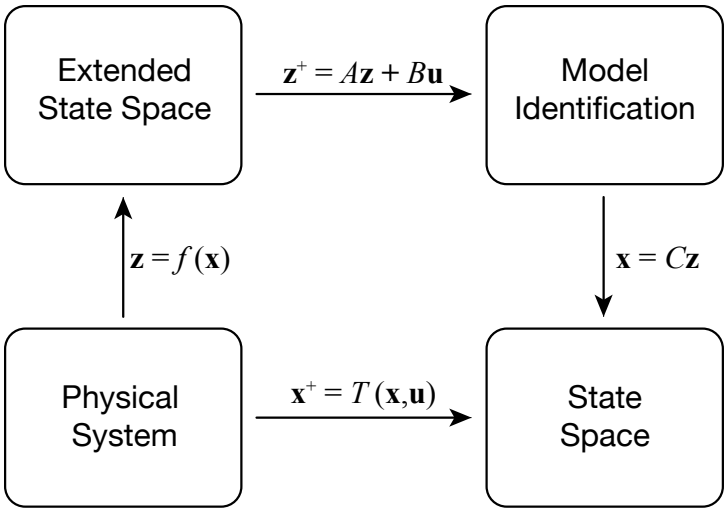

Figure 4.2: Description of Koopman lifting process and reduction to a state space representation. If the (possibly nonlinear) map $T(\mathbf{x}, \mathbf{u})$ is known, a state space representation can be immediately developed. If not, a linear evolution of observables $\mathbf{z}$ can be projected onto the state space after learning the relationship $\mathbf{z}^+ = A\mathbf{z} + B\mathbf{u}$.

$g : S \to \mathbb{R}$, we now define the corresponding Koopman operator

$$(\mathcal{K}g)(x, (u_i)_{i=0}^{\infty}) \coloneqq g(T(x, u_0), (u_i)_{i=0}^{\infty}) \tag{4.2}$$

We seek a finite dimensional linear input/output system which approximates the action of $\mathcal{K}$ on a finite set of chosen observables.

Approximation of Koopman Operators for Control Systems

The Koopman operator in its fully infinite dimensional form is not practically realizable, so we seek a finite dimensional approximation. Under certain conditions, the Hankel Dynamic Mode Decomposition (HDMD) [100,102] provably converges to the Koopman operator in the limit of infinitely many observables and data snapshots [103]. The practical considerations behind our choices of observables and generation of training data are discussed in 4.2.6. The following exposition on the HDMD algorithm is closely based on [101], and is shown in Fig 4.2.

Given K measurements of the system $x_j^+ = T(x_j, u_j)$, we build the following data matrices:

$$X \coloneqq [x_1 \ ... \ x_K], \quad X^+ \coloneqq [x_1^+ \ ... \ x_K^+], \quad U \coloneqq [u_1 \ ... \ u_K]. \tag{4.3}$$

We then choose a vector of m observables

$$\mathbf{f}(x) = [f_1(x) \ ... \ f_m(x)]^T. \tag{4.4}$$

Next, we build the lifted data matrices

$$X_{\texttt{lift}} \coloneqq [\mathbf{f}(x_1) \ ... \ \mathbf{f}(x_K)], \quad X^+_{\texttt{lift}} \coloneqq [\mathbf{f}(x_1^+) \ ... \ \mathbf{f}(x_K^+)]. \tag{4.5}$$

We seek to approximate the action of the extended Koopman operator (4.13) as follows:

$$X^+_{\texttt{lift}} = AX_{\texttt{lift}} + BU \tag{4.6}$$

In order to approximate A and B, we recast this equation as a minimization problem

$$\min_{A,B} \|X^+_{\texttt{lift}} - AX_{\texttt{lift}} - BU\|_F \tag{4.7}$$

which has the solution

$$[A \ B] = X^+_{\texttt{lift}} \left(\begin{bmatrix} X_{\texttt{lift}} \\ U \end{bmatrix} \right)^\dagger \tag{4.8}$$

where † is the Moore-Penrose pseudoinverse. The A and B matrices form a dynamical system relevant not to states in the state space but to an extended set of states formed

by the vector of observables $z = \mathbf{f}(x)$. The resulting system is

$$z^+ = Az + Bu. \tag{4.9}$$

We are often interested in the spectral properties of the Koopman operator because they give us physical information about the multiple coupled time-dependent processes inherent to our system. HDMD can be used to approximate the discrete part of this spectrum [103]. We seek the triplet $(\lambda_i, \phi_i(x), \mathbf{v}_i)$ of Koopman eigenvalues, eigenfunctions, and modes, respectively. The eigenvalues and Koopman modes are simply the eigenvalues and eigenvectors of the HDMD matrix A. The resulting modes also form a convenient basis onto which we can project our dynamics. Computation of the eigenfunctions requires $\mathbf{w}_i$ which are the eigenvectors of the conjugate transpose of A. After these are normalized so that $\langle \mathbf{v}_i, \mathbf{w}_j \rangle = \delta_{ij}$, the eigenfunctions are given by the complex inner product $\phi_i(x) = \langle x, \mathbf{w}_i \rangle$.

4.2.5 Experimental Setup and Methods

Setup and Training

To apply the approach presented in Sec. 4.2.4 to our robot described in Sec. 4.2.3, we built a $1.8\,\mathrm{m} \times 1.8\,\mathrm{m} \times 1.5\,\mathrm{m}$ frame using T-slotted aluminum, with the top face 2/3 covered with plywood to support our robot and driving circuitry. A hole was cut into the plywood through which a rigid pipe extension was passed, that included through-holes for the pneumatic tubing. The robot body was affixed to this pipe extension, and tubing routed to the muscles. The pressurization of the muscles is controlled by six Clippard DV-2M-12 proportional valves, with three each for input and exhaust, one input-exhaust pair attached to each muscle. The main body is held at a constant pressure of 100 kPa

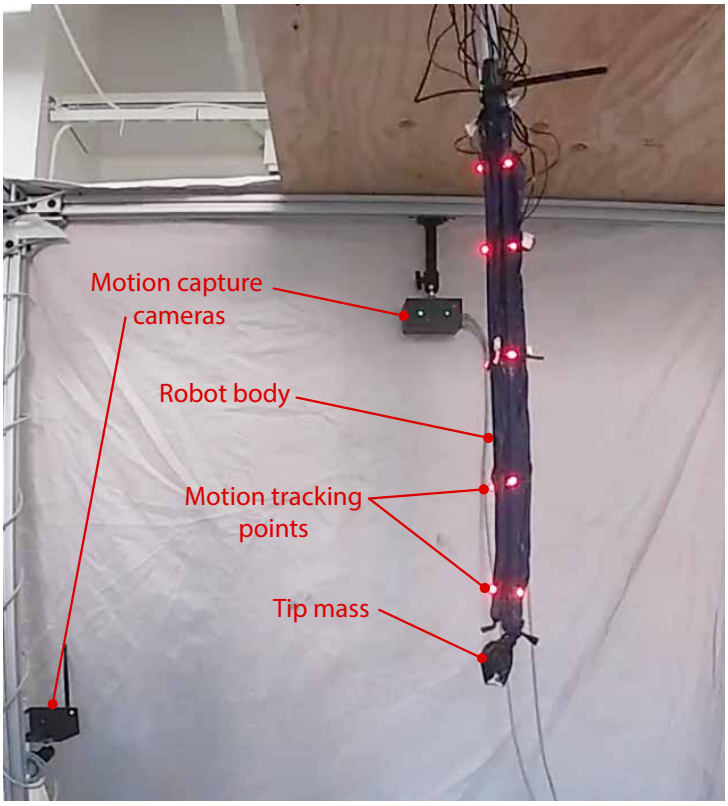

Figure 4.3: Experimental setup, with the robot in an unactuated state.

throughout testing, while the muscles are each controlled in a range of 0-200 kPa.

In order to train our model, we produced inputs that would allow the robot to explore the entire space of configurations that are relevant to our control scenarios. The training inputs were required to be within the bounds $u \in [0.3, 0.85]$ (values given as a percentage of duty cycle), which is the active region for the valves. In the first of two training regimes, 150 randomly generated Gaussians were superimposed to create a smoothly varying signal that was sufficiently random to guarantee that the robot would explore the entire state space slowly and without overshoot. In the second regime, step inputs of random height were commanded to produce massive overshoot and settling to multiple input-modified equilibria. The exhaust signal, v, was defined by $1 - u$. These inputs were then deployed to a Raspberry Pi Model 4B. A trigger signal was also defined to

synchronize the Raspberry Pi and our motion capture system.

Information about the position and shape of the manipulator is gathered via motion capture (PhaseSpace Impulse X2E) with fifteen LED trackers and eight cameras. Five LEDs are attached along the axis of each muscle. This entire process is described in Fig. 4.3.

After 30 minutes of training data were acquired, they were segmented into training sets and verification sets. The model was trained on half the data, while the other half was used for reconstruction and validation.

4.2.6 Results

Here we present the results of our application of the modeling described in Sec. 4.2.4 to the soft robot arm introduced in Sec. 4.2.3.

Koopman for Prediction

We perform a convergence study on the reconstruction power of our Koopman models as a function of the number of snapshots for a range of observables. This process allowed us to develop a dictionary of observables suitable for our system. Given a particular choice of observables and number of training samples, we build the corresponding linear input-output system with A, B, and C matrices. This linear model is applied to $N = 27000$ samples of verification data. These particular samples are not included in the training data in order to give us a fair evaluation of the predictive power of our models. The linear system produced via (4.8) and (4.9) evaluate the evolution of these initial conditions over a single time step. The single-step reconstruction error is given by

$$e_i = \frac{\|x_i^{+,\,\texttt{predict}} - x_i^{+,\,\texttt{actual}}\|_F}{\|x_i^{+,\,\texttt{actual}} - x_i\|_F}.$$

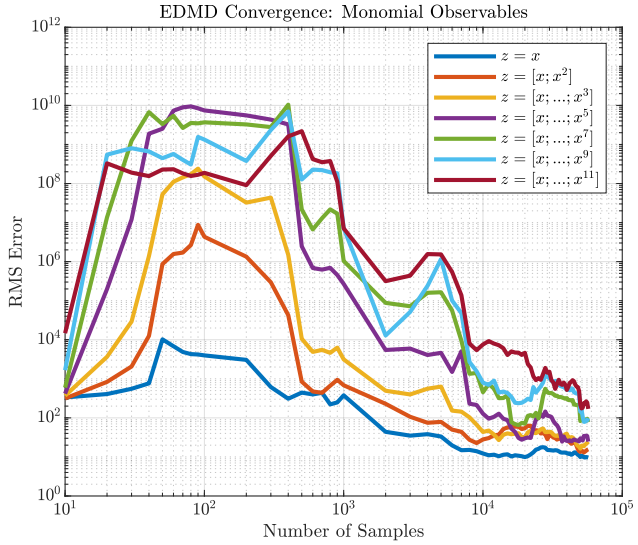

Figure 4.4: The error $e_{\texttt{RMS}}$ vs number of time samples for a range of monomial observables. Here x indicates a column vector of the positions of all 15 motion tracker points. The extended state $z = [x; ...; x^i]$ is formed by stacking the element-wise powers of x from x^1 up to and including x^i. We see a decrease in predictive power as the order of monomials increases.

where $x_i^{+,\,\texttt{actual}}$ is the evolution of x_i measured by the motion capture system and $x_i^{+,\,\texttt{predict}}$ is the evolution predicted by the HDMD model. We use the root mean square (RMS) of the individual e_i errors to score our model:

$$e_{\texttt{RMS}} = \sqrt{\frac{1}{N}\sum_{i=1}^{N} e_i^2}.$$

Choice of Observables We tested two different choices for observables. First, we used the set of monomials ranging from order 1-4, as described in [83], as well as additional monomials up to order 11. We found that these basis functions performed poorly for our highly inertial, non-linear system (Fig. 4.4). As can be seen, prediction diverges with increasing monomial power, likely due to the higher order of error propagation.

Second, we tested time delay observables. Fig. 4.5 shows the results of this analysis, with the opposite trend observed compared to Fig. 4.4. We believe this is due to the

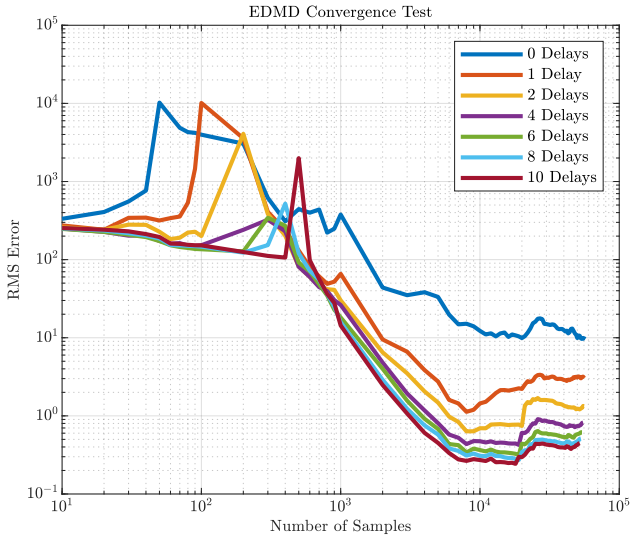

Figure 4.5: The error $e_{\texttt{RMS}}$ vs number of time samples for a range of time delay observables. The extended state with i delays is formed by stacking the current time sample of x on top of the previous i samples. We see a steady increase in predictive power as the number of time delays increases. Given a certain colored line in this figure, the corresponding monomial-based model with the same number of observables is given by the same color in Fig. 4.4. For the rest of the paper, we take 10 time delays.

fact that the momentum of the robot exists in the span of the time delays. We use 10 time delay observables for the rest of our analysis.

Selection of Koopman Modes Fig. 4.6 shows the eigenvalues λ_i of the resulting HDMD matrix. These eigenvalues approximate the eigenvalues of the Koopman operator and are shown with bubble sizes scaled with respect to their respective approximate Koopman mode powers $|\phi_i(\mathbf{x})|$ which are evaluated for every x in the training data and averaged. The eigenvalues corresponding to low mode power often correspond to modes associated with measurement noise. Often, these modes can be removed from the model with the added bonus of reducing the dimension of the model. To do this, we build a matrix whose column vectors are the N Koopman modes we wish to keep $V = [\mathbf{v}_1 \ ... \ \mathbf{v}_N]$. We then project our state space matrices onto the basis of Koopman modes $\tilde{A} = V^{-1}AV$

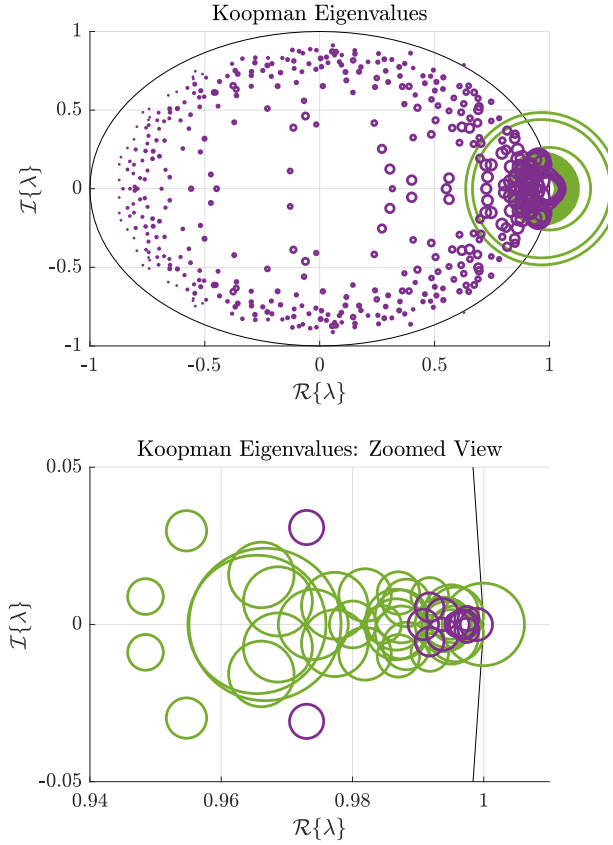

Figure 4.6: Koopman eigenvalues λ_i scaled by their mode powers $|\phi_i(z)|$ averaged over all of the training data. *Top:* The entire distribution of Koopman eigenvalues. *Bottom:* Zoomed in view of the distribution of eigenvalues. The 35 eigenvalues with the largest mode power are given in green.

and $\tilde{B} = V^{-1}B$. The green eigenvalues in Fig. 4.6 represent the 35 modes with the largest mode power. The corresponding reduced order model produced the controller that successfully executed the static reference tracking problem in the bottom part of Fig 4.1.

4.2.7 Discussion

Here we show that Koopman Operator approaches are a viable path of investigation towards soft robot modeling. We present an approach to produce an approximate, low

order model with relatively little data, minimal computational cost, and no *a priori* understanding of the input-output dynamics of the system. This approach is also amenable to traditional linear control schemes, such that existing strategies can produce viable control laws for these highly nonlinear, inertial, and underactuated systems (see Sec. 4.3). Much work is yet to be done in understanding the optimal, minimal selection of modes to achieve the desired behavior. The next section seeks to advance the construction of our models to simultaneously reject noise and capture faster dynamics, and to implement closed loop control to understand the edges of behaviors this robot can be commanded to display.

4.3 Continuation Into Closed-Loop Control

The next logical step from the preceding section is to advance the system into a closed-loop architecture. This was done over a period of years and on two soft arms instead of one – the first arm being a more stable version than that previously presented, and the second arm being recycled from the previous chapter. Using modeling insights from Sec. 4.2, such as time-delay only observable performance and reduced order modeling capability, we developed a system that used only two time delays, a static koopman operator (such as described in [86]), and LQR. The resulting manuscript was published in *Science Robotics* [44].

4.3.1 Abstract

Soft robots promise improved safety and capability over rigid robots when deployed near humans or in complex, delicate, and dynamic environments. However, infinite degrees of freedom and the potential for highly nonlinear dynamics severely complicate their modeling and control. Analytical and machine learning methodologies have been applied to model soft robots, but with constraints: quasi-static motions, quasi-linear deflections, or both. Here, we advance the modeling and control of soft robots into the inertial, nonlinear regime. We control motions of a soft, continuum arm with velocities ten times larger and accelerations forty times larger than those of previous work, and do so for high-deflection shapes with over 110 degrees of curvature. We leverage a data-driven learning approach for modeling, based on Koopman Operator Theory, and we introduce the concept of the static Koopman operator as a pregain term in optimal control. Our approach is rapid, requiring less than five minutes of training, is computationally low-cost, requiring as little as 0.5s to build the model, and is design agnostic, learning and accurately controlling two morphologically different soft robots. This work

advances rapid modeling and control for soft robots from the realm of quasi-static to inertial, laying the groundwork for the next generation of compliant and highly dynamic robots.

4.3.2 Introduction

The automation and robotics revolution has transformed manufacturing and heavy industry, leading to higher throughput, repeatability, and quality across numerous sectors [1,2]. Unfortunately, robots are most often relegated to cages and isolated sections of manufacturing sites due to the inherent danger they present to human operators through their fast-moving, heavy, and rigid structures. Efforts towards allowing these robots to perform safely with human collaborators have focused on software control, but absolute guarantees of safety are not possible [3–6].

In contrast, soft robots are safe by construction due to their low stiffness and mass, but modeling and control of these systems is challenging [8–10,12–14]. This is due to their inherent nonlinearity, high dimensionality, and the imprecise measurement of their position in space. Past work has sought to overcome these obstacles through a variety of modeling methods, each of which constrains the design of control implementations. The majority of these modeling approaches fall into two categories: analytical Reduced Order Modeling (ROM), and machine learning (ML).

In soft robot ROM for control, the aim is to develop an analytical model based on simplifying assumptions such as (piecewise) constant curvature ((P)CC) deformations [97,98,104,105]. For an approximately constant-curvature system, this approach allows for the accurate prediction of dynamics given appropriate estimation of parameters. However, developing these analytical models is nontrivial and labor intensive, and each model applies only to the single system that was modeled. These models

tend to be valid only in a neighborhood around the equilibrium point where the system has been linearized [105]. Controllers based on ROM models have been applied to soft robots in the past, but these have yet to achieve the real-time control of fast, inertial motions [87,106,107].

In the ML modeling of soft robot dynamical behaviors, many neural net-based approaches exist. Most of this work focuses on the development of predictors using neural nets such as Long Short Term Memory (LSTM) [108,109] or recurrent neural networks [87,107]. These methodologies generate highly accurate predictors of the dynamics. However, training these systems has a high computational cost. Moreover, their structure is nonlinear, requiring specialized control algorithms [12]. One example is a feedforward neural net controller which has been successfully coupled to a model-free closed-loop controller and applied to a high-deflection, yet quasi-static soft arm [110,111]. Additionally, there are approaches which leverage a neural-net-based dynamical model in closed-loop control [87,106]. However, neural net approaches to soft robot modeling have not yet resulted in the closed-loop control of high-speed, inertial and nonlinear dynamics.

Koopman Operator Theory (KOT) [99] is an alternative modeling paradigm, introduced to the field of ML and data-driven modeling in the early 2000s [80,112]. KOT-based ML has two qualities that make it attractive strategy for soft robot control: it is data-driven, eliminating the need for complicated analytical models, and it identifies a globally linear model, allowing for fast and efficient control design. The Koopman operator is a representation of a dynamical system in terms of the evolution of observables on a function space. Although the evolution of a dynamical system on state space may be nonlinear, its evolution in function space - described by the potentially infinite dimensional Koopman operator - is always linear. This is in contrast to a state-space linearization, which builds a linear approximation of the nonlinear dynamics only valid in a small region of the workspace. The Koopman methodology has been applied to con-

trol systems, with the majority of work combining a Koopman operator approximation method, Dynamic Mode Decomposition, with control (DMDc) [100,102,103,113–115]. In particular, model predictive control (MPC) is commonly used [101]. When DMDc and MPC are applied to soft robots, [83–85,116] the control is accurate, but only shown so in quasi-static control in a low-deflection regime (approx. 18 dergrees of curvature). It is important to note that simple linearized models are likely to work at these low deflections because the full nonlinearity of the dynamics may only be explored at high deflections. In fact, references [83–85] show imperfect yet functional controllers using purely state-space linear MPC, suggesting the quasi-linearity of these systems.

In addition to MPC, the combination of the Koopman operator and the Linear Quadratic Regulator (K-LQR) optimal control scheme has shown promise in rigid robot applications [117,118] and the control of fluid dynamics problems [119]. Notably, Mamakoukas et al. [120] show promise in a 1-DoF soft robotic fish application employing a similar Koopman structure.

Even with these many advances in the field, existing soft arm control implementations [82–85,120] have yet to be demonstrated in the inertial, non-linear regime. In order to compare with other works, we introduce the following definitions of the "inertial regime" and "nonlinear dynamics." We define the inertial regime for soft arms to be when the inertial force experienced by the tip F_{tip} is of the order of its weight $F_{\text{tip}} = ma_{\text{tip}} \approx mg$, meaning $a_{\text{tip}} \approx g$. Here m is the mass of the tip of the arm, a_{tip} is the acceleration of the tip during closed-loop control, and $g = 9.81\frac{m}{s^2}$. We define nonlinear dynamics to be motions that fail to be adequately captured by a state-space linearization. Thus, an open challenge remains: modeling and control of inertial dynamics in highly nonlinear soft robots.

In this work, we advance modeling and control of soft, continuum arms into the inertial regime. Previous work has considered quasi-static motions, with accelerations

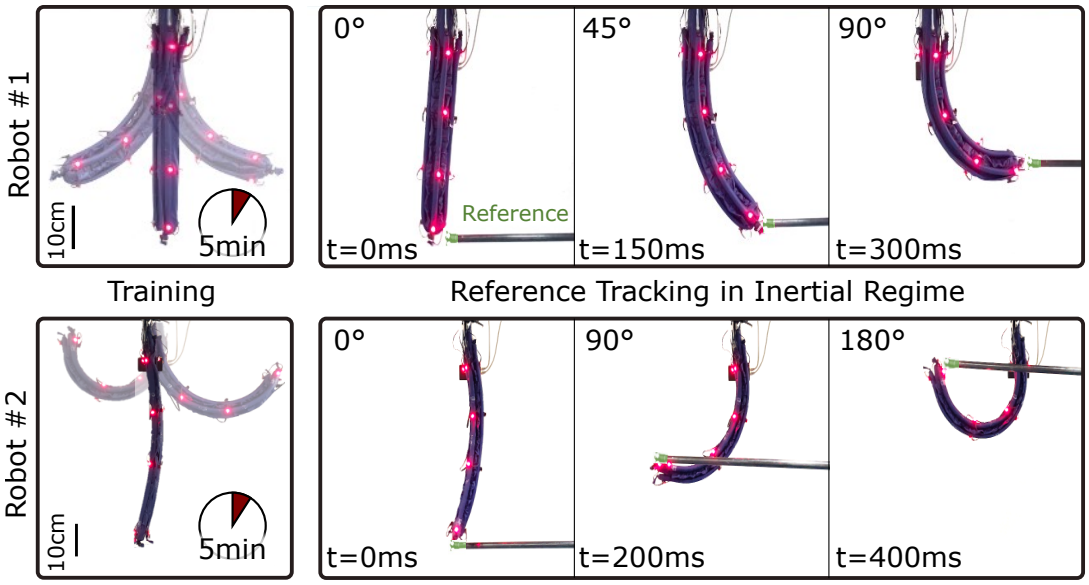

Figure 4.7: **Inertial, nonlinear soft arm control.** Using a combined static and dynamic Koopman framework, we achieve the closed-loop control of soft robotic arms exceeding 10x the tip speed, 40x the tip acceleration, and 6x the angular displacement of existing soft arms. This achievement brings soft robotics into the inertial, nonlinear regime. Only five minutes of training is required to achieve an optimal controller capable of high-deflection, high-accuracy closed-loop tracking of a reference (the tip of a pole moved rapidly by a human). The same methodology is applied to both a low-slenderness-ratio, four-muscle arm (Robot #1) and a high-slenderness-ratio, three-muscle arm (Robot #2). Both arms achieve their highest deflection in under half a second.

below $0.03g$. Our work demonstrates movements in closed-loop control with accelerations greater than $1g$ (see Table 4.1). We control these inertial movements in a highly nonlinear, high-deflection regime across two variations of our soft arm, each with different dimensions, numbers of actuators, and workspaces. The first demonstrates curvatures up to 110 degrees (Robot #1) and the second up to 180 degrees (Robot #2) (Fig. 4.7).

This capability is enabled by the introduction of the static Koopman pregain, which maps held inputs to converged robot configurations. After being learned from data, we use it as a pregain term in the LQR implementation. The static Koopman pregain greatly increases the accuracy of static pointing tasks and improves the stability of dynamic tasks.

We show our approach requires minimal training and low computational cost, both

for determining the model and controlling the robot. Collecting our training data takes less than 5 minutes and the computation of the model takes less than a second, as opposed to the long training times required by many neural net-based approaches. Our approach estimates both the static and dynamic control Koopman operators, enabling the use of low latency, efficient optimal control methods; this enables real-time tracking of fast-moving reference positions, even if field-deployed on a low-power microcontroller.

Table 4.1: **Comparison with existing soft, coninuum arms shows advances in speed, acceleration, and deflection during closed-loop control.** This work demonstrates a 10x increase in reference tracking tip speed **[Speed]** and a 4x improvement in tip deflection angle **[Deflection]** and advances closed-loop control of soft robot arms into the inertial regime $a_{\text{tip}} > g = 9.81\frac{m}{s^2}$. The acceleration **[Accel]** of the soft arm's tip a_{tip} is computed using the centripetal acceleration of soft arms for which circular reference tracking data is available. The distance from the base to the tip of each arm is also given **[Length]**. Note that closed-loop deflection data does not include the large-deflection open-loop tests present in some works. Acronyms: LQR - Linear Quadratic Regulator, RNN - Recurrent Neural Network, ROM - (analytical) Reduced Order Model, PCC - Piecewise Constant Curvature, MPC - Model Predictive Control, LSTM - Long Short-Term Memory, TRPO - Trust Region Policy Optimization, GPR - Gaussian Process Regression, TO - Trajectory Optimization, FFC - feedforward compensator, SM - sliding mode, AF - analytical feedback, R1: Robot #1, R2: Robot #2.

Robot	**Length** $[m]$	**Speed** $[\frac{m}{s}]$	**Accel** $[\frac{m}{s^2}]$	**Deflection** $[deg]$	**Model**	**Control Method**
This Work	0.37	1.52	11.6	R1: 110 R2: 180	Koopman	LQR
[87]	0.4	0.15		21	RNN	TO
[111]	0.3	0.12	0.065	45	None	NN FFC
[121]	0.3	0.1	0.1	20	ROM	SM
[116]	0.15	0.094	0.29	18	Koopman	MPC
[98]	0.38	0.09	0.032	27	PCC ROM	AF
[106]	0.44	0.05		19	LSTM	TRPO
[82]	0.25	0.035	0.012	7	Koopman	MPC
[85]	0.7	0.03	0.032	8	Koopman	MPC
[107]	0.22	0.002	0.0016	11	RNN	GPR

4.3.3 Results

In this section, we first outline our approach that enables modeling and control in the inertial, nonlinear regime, yet requires relatively little training data and low computational power. Next, we systematically test the speed and accuracy of the resulting closed-loop controller in a series of circular reference tracking tests. The soft arm is further tested in a tip-tracking test with a rapidly changing, user-defined reference position designed to test the soft arm's responsiveness to changes in commands in real time. Lastly, we test our methodology on the dynamic catching and throwing of a ball. This leverages the inertial dynamics of our soft arm to demonstrate its effectiveness in real-world tasks.

Dynamic and Static Koopman Operator Optimal Control

The successful real-time control of a soft arm in the inertial and nonlinear regime requires both a model that captures these dynamics and a control methodology that adapts to the motion of the robot in real time. We achieved this by building a controller which leverages both the dynamic and static Koopman operators of the soft arm system. The Koopman operators describe the evolution in time of functions defined on the robot configurations and inputs. These functions are called observables, and the approximation of the Koopman operators involves training on data which is augmented by a chosen basis of observables. The data is collected through a series of training experiments, performed by commanding step inputs with randomly distributed magnitudes. This training data is partitioned into dynamic and static components which are used to train the two separate Koopman operators (see Section 4.3.5). Both the training and model computation processes are fast, requiring only 5 minutes (approximately $18,000$ samples at 60Hz collection rate) for training data collection, and the matrix pseudo-inverses used

in the model construction take less than a second on an ordinary laptop computer.

The observables used to train the dynamic Koopman model are time delayed measurements of the position of motion tracking points placed on the soft arm. This turned out to be sufficient to build a linear model of its nonlinear dynamics. Previous work considered adding a single time delay to hundreds of monomials [82]. However, inspired by the fact that, for ergodic systems, the limit of infinitely many time-delay observables results in DMD's convergence to the true Koopman operator [100,102,122], we included only time-delay observables. Our results show that time-delay-only observables are sufficient to capture the dynamics of this nonlinear system (see Supplementary Fig. A.2), and that without time delays, the eigenvalues in the high-frequency and dissipative regions of the unit circle and their corresponding Koopman modes are missing (Fig. 4.8). This time-delay-only approach avoids the added computational cost of many monomial observables, andalso eliminates the large tails associated with monomials which magnify noisy measurements far from the origin. We express this dynamic Koopman operator as a pair of matrices A and B giving the uncontrolled and controlled dynamics, respectively. These can be used to build the Koopman-LQR controller described in Section 4.3.5.

The resulting feedback controller is able to command the soft arm to follow a fast-changing reference position, but suffers from steady state error. Introducing integral control (for example, Linear Quadratic Integral Control) is one of the commonly used approaches to minimizing steady-state error [123]. This method, however, is sensitive to measurement noise and requires a trade-off between speed of response and tracking accuracy. As a consequence, the implementation for our goals of highly inertial tasks resulted in poor tracking performance outside of the quasi-linear and quasi-static regimes. Instead, we address the steady state error by introducing a static Koopman pregain, a control concept we developed for the current work. The static Koopman operator was first formally described in our recent modeling work [86], but no connection to control

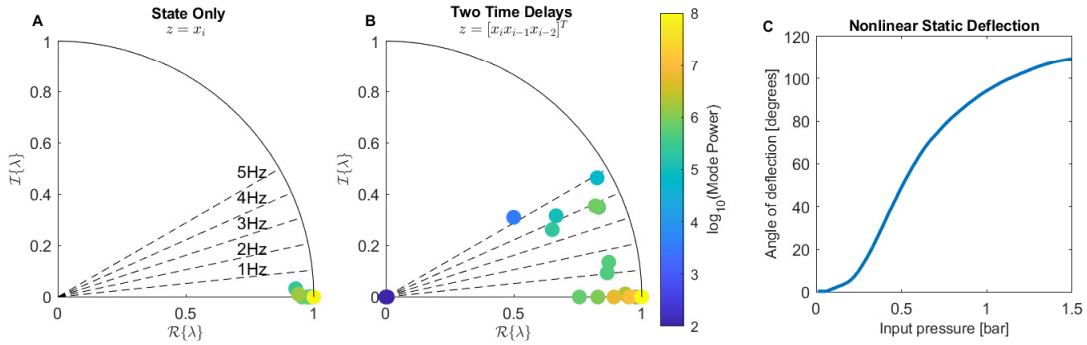

Figure 4.8: **Nonlinear and Inertial Dynamics of the Soft Arm.** The eigenvalue plots for Koopman models with state only (**A**) and state plus time delay observables (**B**) are shown. The dashed radial lines signify sections of the unit circle corresponding to modes with $1 - 5$Hz dynamics. The eigenvalues are shaded corresponding to the logarithm of their maximum achieved mode power evaluated over the training data (see Section A.1). Using state-only observables results in a simple linearized model which does not capture any transient dynamics. The addition of two time delay observables allows the modeling of dynamics up to 5Hz. This is the model we choose for our experiments. (**C**) Presentation of the input-output nonlinearty of the system, which exhibits a sigmoidal deflection response. Modeling this nonlinearity is essential for acceptable reference tracking performance in the high-deflection regime.

design was made. Unlike the dynamic Koopman operator, this operator is a map between functions defined on two different spaces. In our application, the static Koopman operator is used to map functions defined on the space of inputs to functions defined on the space of robot configurations. We learn this operator from the static partition of the training data so that static positions in the workspace of the soft arm correspond to the values of the inputs required to reach those positions after all transient motions dissipate. This operator is then used as a pregain term that augments the LQR controller. Sensor noise is known to cause tracking issues in soft robots attempting to perform real-time tracking of aggressive control inputs [13]. Our control structure mitigates this problem by balancing the noise-sensitive dynamic Koopman LQR term with the sensor-agnostic static Koopman pregain.

The construction of the controller and the computation of the optimal input are also

fast processes which have low computational overhead. The solution of the Riccati equation involved in computing the LQR control gain takes less than a second, and computing the optimal input at a given time step only requires two small matrix multiplications. This is easily achievable in real-time on a low-cost microcontroller.

Closed-loop circle-tracking in inertial, nonlinear regime

With our control architecture in place, we first sought to characterize the performance across a range of deflections and soft arm speeds in a planar circular reference tracking (smooth changes in reference position). We commanded the soft arm's tip to trace out circular paths in the X-Y plane with three radii (100mm, 180mm, and 220mm) and six frequencies ($0.1, 0.3, 0.5, 0.7, 0.9$, and 1.1Hz), as shown in Fig. 4.9. The same controller was used for all references, as described in Section 4.3.5.

These results show that the soft arm tracks the reference with consistent performance throughout the full range of deflections and speeds tested (Fig. 4.9, *left*, Movie S2). The fastest and highest deflection circle-tracking result demonstrates a tip speed of 1.5m/s, a speed-to-length ratio of 3.23s^{-1}, and a tip acceleration of 11.6m/s^2 in closed-loop control. This is approximately an order of magnitude faster and forty times higher acceleration than any soft continuum arm of which we are aware (see Table 4.1). Importantly, the system was trained exclusively on step inputs, and as such the model had no *a priori* knowledge of the control objective nor had it been trained on circular behaviors.

Additionally, we show that the relative contribution of the dynamic Koopman LQR input versus the static Koopman pregain increases with increasing speed and deflection (Fig. 4.9, *right*). For relatively low speeds and deflections, the dynamic Koopman LQR input is quite small, and the static Koopman pregain dominates. As accelerations increase and inertia becomes non-negligible, the dynamic component increases in magnitude to compensate for the static term's inability to account for inertial effects. This suggests that

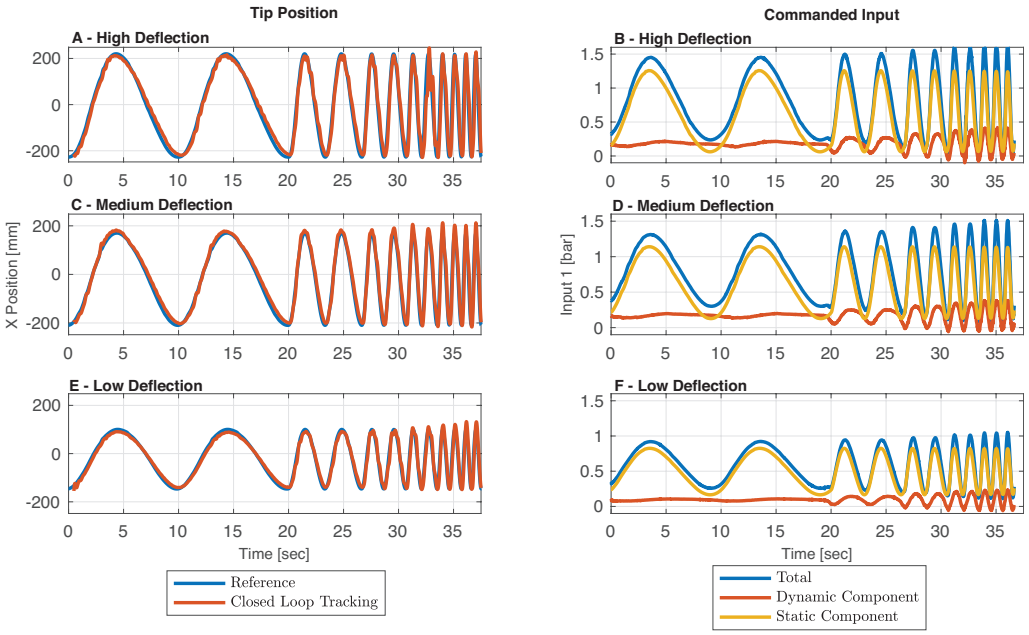

Figure 4.9: **Closed-loop reference tracking experiments show the soft arm's ability to track in real-time**. The soft arm tracked circular reference trajectories in the X-Y plane with frequencies ranging from 0.1 to 1.1 Hz (0.2 Hz step) at: (**A**-**B**) high, (**C**-**D**) medium, and (**E**-**F**) low deflections. Plots **A**, **C**, and **E** show the X positions (red) over time compared to their respective references (blue). The Y and Z positions are shown in Supplementary Fig. A.3. Plots **B**, **D**, and **F** show the relative contributions of the static Koopman pregain (yellow) and dynamic Koopman LQR (red) to the total input (blue). At quasi-static speeds, only the static Koopman pregain is required for effective performance (i.e. the quantity $x - x_{ref}$ is approximately zero); as inertial effects increase, the LQR component increases its contribution to maintain performance. Only the commanded inputs to one of the four side muscles is shown, but the results are similar for all muscles.

for any soft robot performing a non-inertial task, the incredibly simple static Koopman pregain could be sufficient for control.

Closed-loop, real-time reference-tracking in inertial, nonlinear regime

We next sought to characterize the controller performance for a less structured and more challenging control objective: tracking a real-time, user-defined reference. To do so, we commanded the controller to decrease the euclidean distance between the tip of the soft arm and a motion tracker point located on the tip of a pole. A human operator

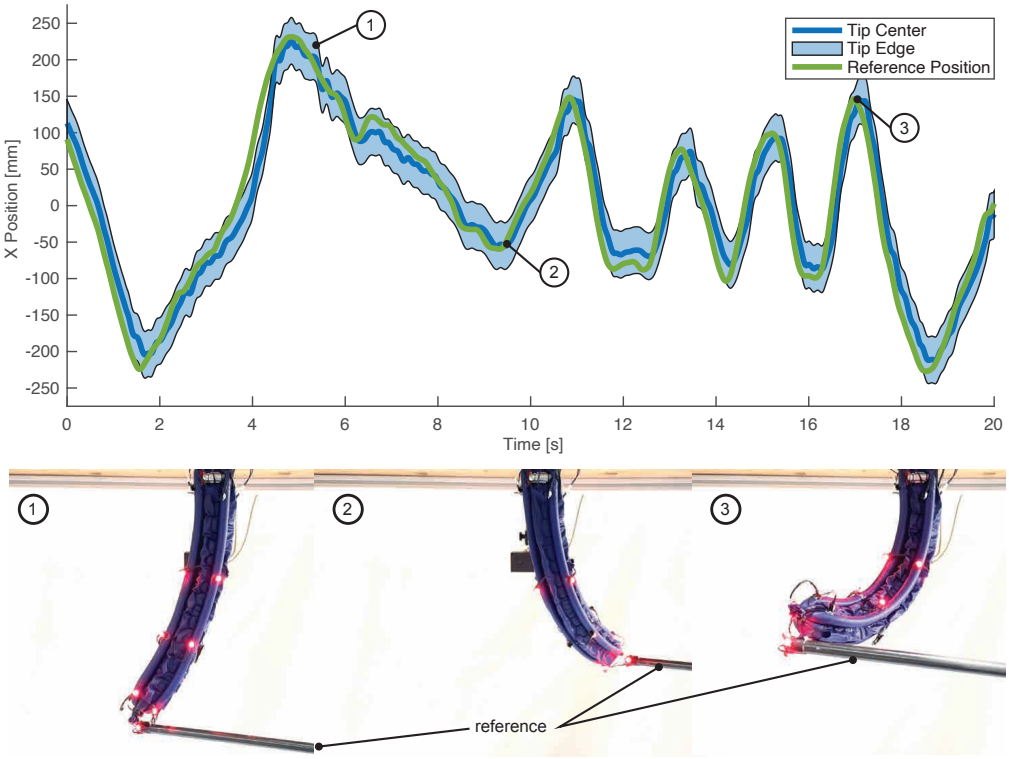

Figure 4.10: **Performance of our controller subjected to a series of arbitrary reference positions spanning the high-deflection workspace.** (**A**) The X position of the soft arm tip is shown as it tracks a moving reference commanded randomly by an operator. Contact between the green lines and blue band indicates points where the soft arm is touching the reference marker. (**1-3**) show images of the soft arm performing this behavior. Of note, the robot rarely loses contact with the moving reference.

moved the pole across random trajectories within the reachable workspace of the soft arm. Throughout the test, the robot remains in contact almost continuously while achieving speeds exceeding 0.7m/s (as shown in Fig. 4.10 and Movies S1 and S4).

To demonstrate the generalizability of our approach for different soft arms, we also tested our approach on a morphologically different second arm. The second arm is longer, more slender, and has three instead of four side muscle. This results in larger curvatures and a helical actuation pattern, as discussed in Section 4.3.5. Despite these differences, no changes were needed in the learning and control algorithm, aside from

updating the number of inputs. This second system was exposed to 5 minutes of step input training data, the model and controller were calculated and deployed, and the system was commanded to again track the tip of the user-operated pole. Results of this test are shown in supplementary materials (Movie S5), and stills from the testing are shown in Fig. 4.7.

Dynamic Throwing and Catching

With the viability of our method shown in the above characterization tests, we finally demonstrated how its capabilities translate to sample robotic tasks. We challenged our soft continuum arm in two ways: first, to catch a ball swinging through the air as we demonstrate in Fig. 4.11, and second, to receive an object from an operator, and to throw it into a reference bin as shown in Fig. 4.12. Both tests are shown in Movie S3. The catching component of this demonstration is similar to the ball catching performed by a two-link arm with a soft joint [124], but here completed with a fully soft continuum robot arm.

4.3.4 Discussion

We presented a data-driven framework for the modeling and control of inertial and nonlinear soft robots. We used Koopman Operator Theory to enable the application of linear control methods to this highly nonlinear, inertial system. We introduce a Koopman-LQR with static Koopman pregain capable of accurately controlling two different soft robots that exhibit high deflections and inertial motions. Advancing the state of the art, the proposed method allows the construction and deployment of both a model and optimal controller from less than 5 minutes of training data - to the best of the authors knowledge, the shortest in soft robotics (Fig. 4.13). Compared to existing MPC-

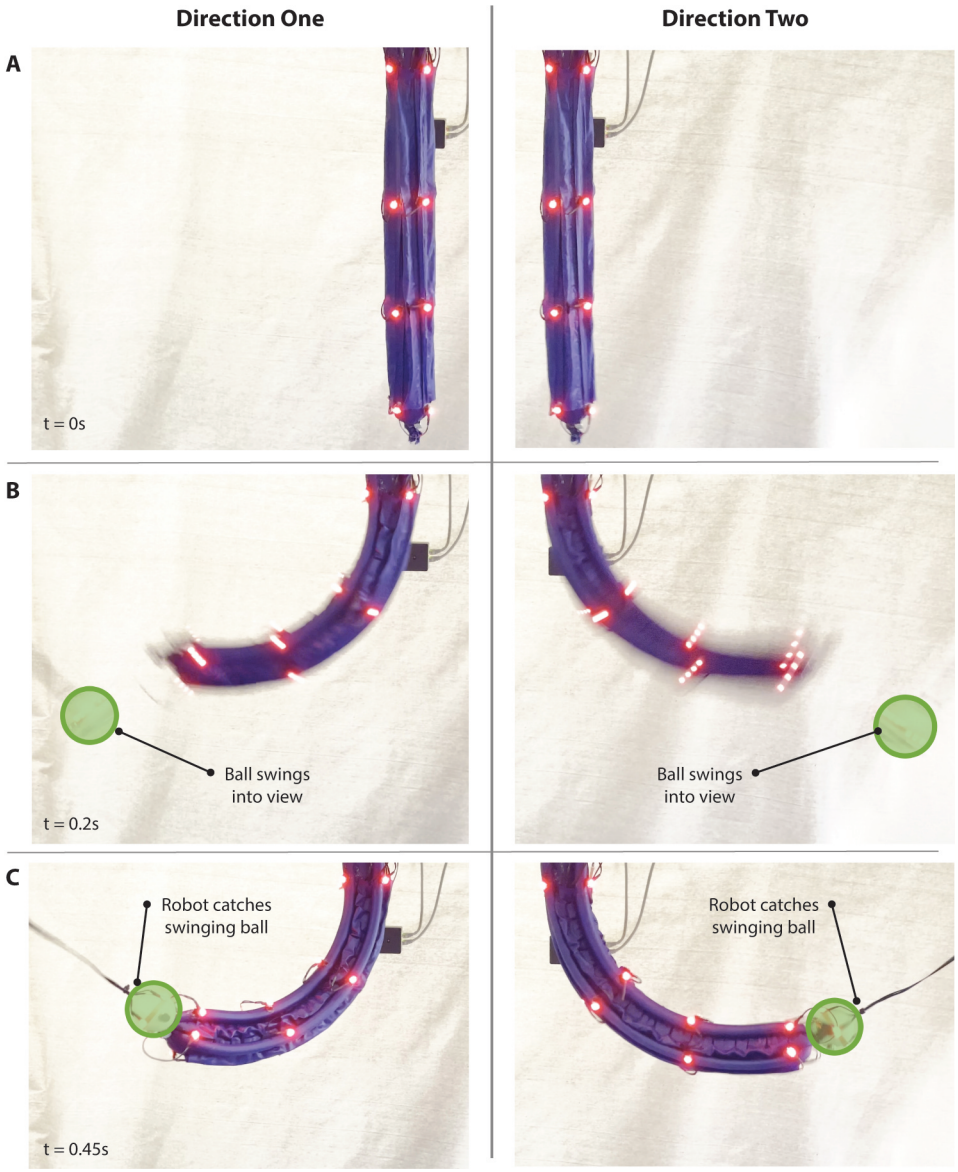

Figure 4.11: **Performance of our controller when attempting to minimize error on an arbitrary trajectory (catching a swinging ball).** (A) The soft arm stays in the neutral position while the ball is outside the workspace. (B) Once visible, the soft arm rapidly responds to reach the ball (outlined swinging into the workspace). (C) The soft arm tip intercepts the ball and catches it (with small magnets on both the soft arm tip and swinging ball.)

based controllers, K-LQR is computationally less expensive and can be deployed on a simple microprocessor, enabling cheap and scalable use in a variety of environments outside the research laboratory. Despite its simplicity, our controller allows our soft arm

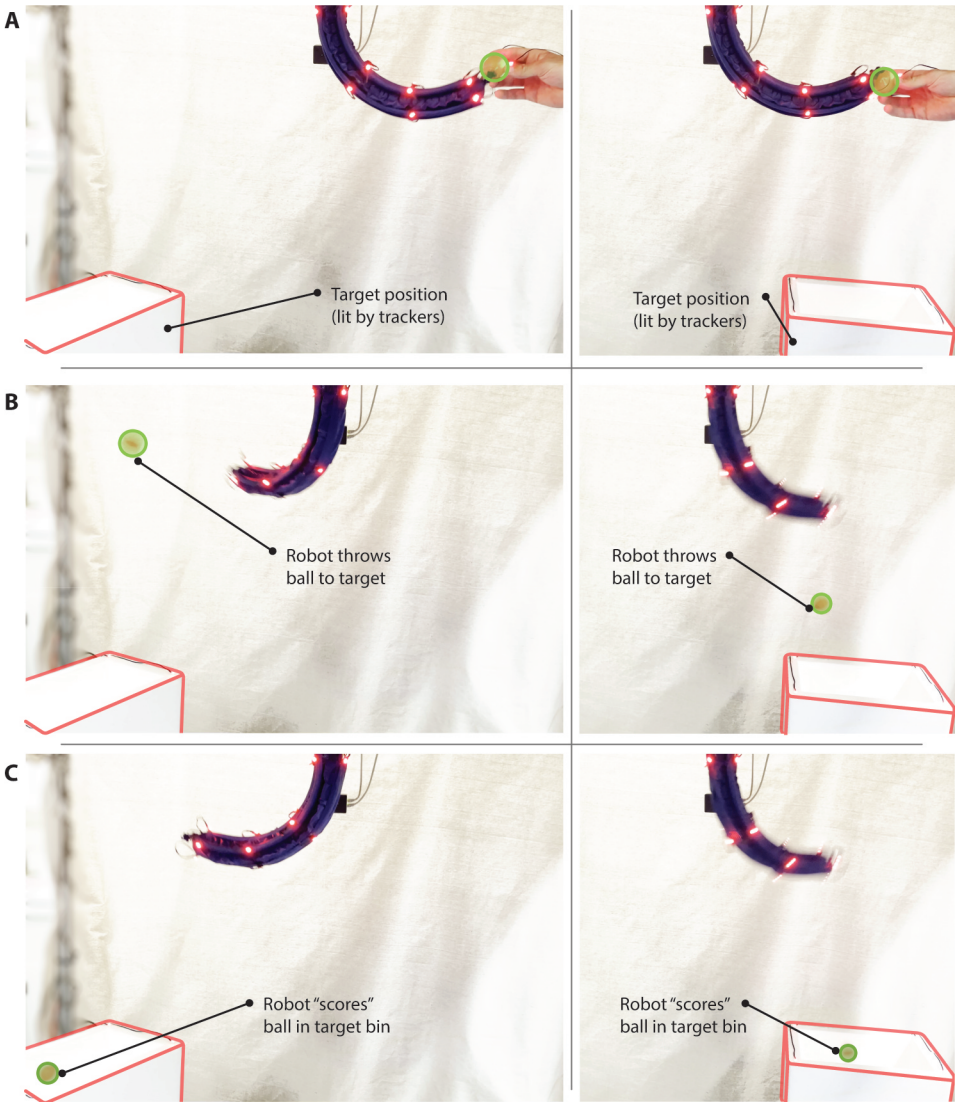

Figure 4.12: **Demonstration of implications of the developed methodology: completing example tasks** (A) The soft arm identifies the objective and approaches it (operator's hand). (B) After the operator's hand is removed and the ball is supported by the soft arm, the objective changes to the bin (lighted bin in bottom left and right, respectively). The soft arm now flings the ball at the objective. (C) The ball successfully enters the bin in two different, arbitrary locations, achievable only by working in the inertial regime.

to undergo controlled accelerations substantially greater than previous examples, even exceeding $1g$ (Table 4.1).

Although the presented demonstration of our modeling and control approach focused

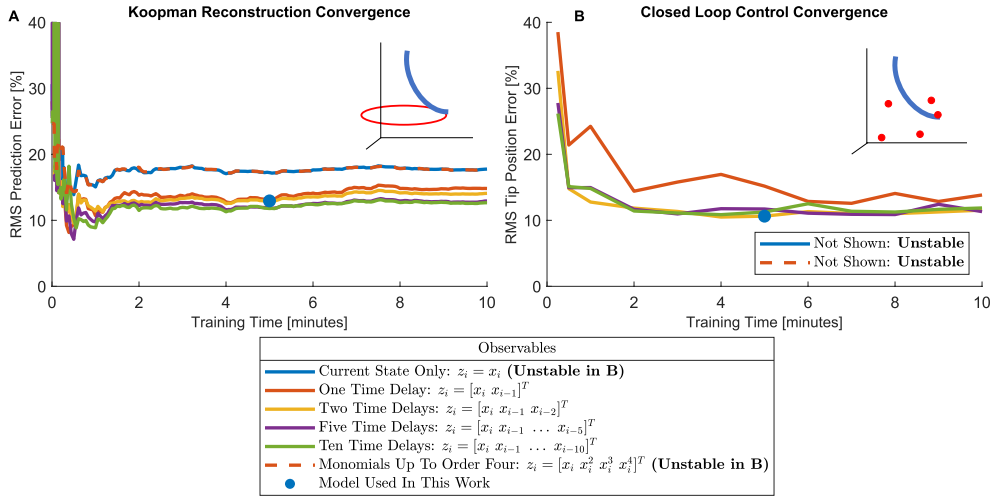

Figure 4.13: **Convergence of the Koopman model and control system.** (**A**) The dynamic Koopman model requires the addition of five time delay observables and only one minute of training data to reach minimum prediction error. To determine this error, the single-step prediction error of the dynamic Koopman model is collected for all points as the soft arm moves on a circular path in the X-Y plane (inset), and the root-mean-square (RMS) average is taken. For comparison, a Koopman model using monomials of the state up to order four gives no improvement over the state only model. This reconstruction is performed on a model trained on zero sinusoidal trajectories. (**B**) In closed-loop control, the combination static/dynamic Koopman controller requires only five minutes of training data and two time delays to reach minimum prediction error; accordingly, we use this controller design for every experiment. Each controller was commanded to move the soft arm's tip to a sequence of points in the workspace of the soft arm, and the average RMS error for all these points was calculated. Using zero time delays resulted in the soft arm being unable to stabilize at any reference position, so that line is not shown.

on soft robots, its implications could be much broader. The approach's ability to explore the dynamical features of a complex, nonlinear, inertial system could offer advantages in modeling and control of myriad robotic systems. Further, its speed, versatility, low computational cost, and ease of use potentially expand the accessibility of robotics to new user groups. As such, we believe our approach has the potential to make field-deployable, dynamical, soft robotic systems notably closer to realization.

4.3.5 Materials and Methods

Here, we first introduce Koopman Operator Theory, the mathematical underpinning of our modeling effort. In Section 4.3.5, we describe a practical method to build the model for our control system from data. In Section 4.3.5 we describe how this model is embedded into a real-time feedback controller. Our modeling and control insight is the addition of a static Koopman operator pregain described in Section 4.3.5. The design and fabrication of our soft arms, and a description of the pneumatic circuitry that drive them is then presented. A block diagram detailing the full training process, modeling, and control architecture is given in Supplementary Fig. A.4.

Koopman Operator Theory

The state space representation of a dynamical system involves defining an n-dimensional state space manifold M with states $x \in M$ and discrete-time evolution given by

$$x^+ = S(x). \tag{4.10}$$

Here S is the possibly nonlinear state transition function $S : M \to M$ and x^+ is the time-shifted state. In our application, $M = \mathbb{R}^n$.

This nonlinearity is often critical to modeling a system in state space, but it complicates the design of control algorithms. We instead turn to an operator-theoretic perspective of dynamics of observables [99]. Observables are complex-valued functions defined on the state space $f : M \to \mathbb{C}$. We will restrict ourselves to real-valued observables $f : M \to \mathbb{R}$. The set of all possible observables forms a vector space that is usually infinite dimensional. The Koopman operator $\mathcal{K}$ is defined by

$$\mathcal{K}f \coloneqq f \circ S. \tag{4.11}$$

This operator describes the evolution of observables under the action of the dynamics (4.10). Even though the underlying state space system is nonlinear, the Koopman operator $\mathcal{K}$ is always linear [80,86,99,112]. This is true without restriction on the dynamics or observables.

We want to exploit this linearity to enable the design of an efficient optimal control scheme. This requires extending the Koopman framework to systems of the form $x^+ = S(x, u)$ where $u \in \mathbb{R}^p$ is a p dimensional vector of user-specified inputs. In full generality, the Koopman operator for systems with input acts on observables of the form $f : M \times \mathcal{U} \to \mathbb{C}$ where $\mathcal{U}$ is the space of all control sequences indexed by time $\bar{u}(\cdot) : \mathbb{N} \to \mathbb{R}^p$. We redefine the state transition function to include inputs $S : M \times \mathbb{R}^p \to M$ and introduce the left shift operator $T : \mathcal{U} \to \mathcal{U}$ which simply chooses the next input in a sequence $(T\bar{u})(k) = \bar{u}(k + 1)$. When the observables are defined on both the states and inputs, their Koopman evolution is given by

$$(\mathcal{K}f)(x, \bar{u}(\cdot)) \coloneqq f(S(x, \bar{u}(0)), T\bar{u}(\cdot)). \tag{4.12}$$

Elements of $\mathcal{U}$ are infinite dimensional, which puts the observables $f : M \times \mathcal{U} \to \mathbb{R}$ on an infinite dimensional domain, so they cannot be manipulated on a computer. We introduce the simplifying assumption that knowing only the input at the current time step is enough to predict the future dynamics. We can now define observables of the form $f : M \times \mathbb{R}^p \to \mathbb{R}$. This results in a Koopman operator $\mathcal{K}$ defined by

$$(\mathcal{K}f)(x, u) \coloneqq f(S(x, u), u) \tag{4.13}$$

We seek a finite dimensional linear input/output system which approximates the action of $\mathcal{K}$ on a finite set of chosen observables. This process is described in Section 4.3.5.

Approximation of Koopman Operators for Control Systems: DMDc

We follow the process outlined in [101]. The Koopman operator in its fully infinite dimensional form is not practically realizable, so we seek a finite dimensional approximation. The first step is to choose some finite dictionary of observables $\{g_j(x,u)\}_{j=1}^{m+p}$. We choose m observables which are functions of purely the states, p which are functions of the inputs, and none which are coupled functions of both the states and inputs

$$\{g_j(x,u)\}_{j=1}^{m+p} = \{f_j(x)\}_{j=1}^{m} \cup \{h_j(u)\}_{j=m+1}^{m+p}. \tag{4.14}$$

It is simple to allow arbitrary input observables, but we only deal with the case where $h_j(u) = u_j$. This decoupling restricts our choices of observables, but it allows us to define a vector of observables $z(x) = [f_1(x) \cdots f_m(x)]^T$ called the lifted state which allows us to represent our dynamics as a linear input-output system

$$z^+ = Az + Bu. \tag{4.15}$$

Here A and B are the state transition and input matrices, respectively. This simplification has the benefit of enabling the later use of the fast and efficient linear optimal control methods described in Section 4.3.5, while still capturing the dynamics of the system as demonstrated in Fig. A.2.

The states are retrieved from the observables using the output equation

$$x = Cz \tag{4.16}$$

where C is the output matrix.

Here, we outline the approximation of the matrices A, B, and C using a process called

extended dynamic mode decomposition with control (EDMDc) [101]. When restricted to time delay observables, we call this Hankel-DMDc or HDMDc. We want to approximate these matrices using K measurements of the states $\{x_1, ..., x_K\}$, time-shifted states $\{x_1^+, ..., x_K^+\}$, and inputs $\{u_1, ..., u_K\}$ collected from experimental data. First, we build data matrices whose columns are the data vectors

$$X \coloneqq [x_1 \ ... \ x_K], \tag{4.17}$$

$$X^+ \coloneqq [x_1^+ \ ... \ x_K^+], \tag{4.18}$$

$$U \coloneqq [u_1 \ ... \ u_K]. \tag{4.19}$$

Next, we build the lifted data matrices using our chosen vector of observables $z(x)$

$$X_{\text{lift}} \coloneqq [z(x_1) \ ... \ z(x_K)], \tag{4.20}$$

$$X_{\text{lift}}^+ \coloneqq [z(x_1^+) \ ... \ z(x_K^+)]. \tag{4.21}$$

The desired matrices A and B satisfy the equation

$$X_{\text{lift}}^+ = AX_{\text{lift}} + BU. \tag{4.22}$$

In order to approximate A and B, we recast this equation as a minimization problem

$$\min_{A,B} \|X_{\text{lift}}^+ - AX_{\text{lift}} - BU\|_F \tag{4.23}$$

which has the solution

$$[A \ B] = X_{\text{lift}}^+ \left(\begin{bmatrix} X_{\text{lift}} \\ U \end{bmatrix} \right)^\dagger \tag{4.24}$$

where † is the Moore-Penrose pseudoinverse. Since we prescribe our first n observables to

be the states $x \in M$, we can compute the output matrix using a partial identity matrix

$$C = \begin{bmatrix} I_{n\times n} & 0_{n\times m-n} \\ 0_{m-n\times n} & 0_{m-n\times m-n} \end{bmatrix}. \tag{4.25}$$

The action of the matrices A and B on the lifted state via Equation 4.15 approximates the action of the Koopman operator $\mathcal{K}$ in Equation 4.13. Under certain assumptions, this representation of the Koopman operator converges to the true Koopman operator [103]. True convergence requires infinite data samples which are uniformly distributed in state space and a collection of observables which span an invariant subspace of the Koopman operator's underlying function space. We discuss our method of generating training data in Section 4.3.5.

Koopman-LQR (K-LQR)

To date, similar investigations have used model predictive control (MPC) to control their soft robotic systems [83–85]. Using predictions of the dynamics and a tunable prediction horizon, this architecture calculates input sequences which move the system toward a desired reference position. This enables the use of explicit input and state constraints, but the real-time constrained optimizations involved in this method demand a high computational overhead.

In our inertial soft arm controller, explicit constraints are less important than keeping computational cost and latency low. For unconstrained linear optimal control problems with quadratic cost, the linear quadratic regulator (LQR) provides an analytical solution which does not require predictions of the dynamics in real time [123]. For our controller, we begin with the application of LQR to the dynamic Koopman representation of a dynamical system (previously demonstrated for a robotic fish [120]), and augment it via

the introduction of the static Koopman term, described in Section 4.3.5.

Here we describe the dynamic Koopman LQR control law. Although originally introduced for linear dynamical systems in state space, LQR can also be applied to a vector of observables z of a nonlinear control system as long as a linear, finite dimensional representation of the Koopman operator (A, B) exists. Given the system

$$z^+ = Az + Bu \tag{4.26}$$

$$x = Cz, \tag{4.27}$$

we define the global cost function

$$J = \sum_{i=1}^{K} \left[(z_i - z_{\text{ref}})^T Q (z_i - z_{\text{ref}}) + u_i^T R u_i \right] \tag{4.28}$$

where $x_{\text{ref}} = C z_{\text{ref}}$ is the desired position and Q and R are diagonal lifted state and input penalty matrices, respectively.

The computation of the minimizing control input is a classical method in optimal control [123] and is given by $u_i = -K(z_i - z_{\text{ref}})$ where the matrix K is the LQR gain. This control law results in steady state errors in much of the soft arm's workspace. This is remedied in the next section by the addition of a pregain term based on the static Koopman operator.

Static Koopman Pregain

Unfortunately, Dynamic Koopman LQR alone resulted in substantial disagreement between reference positions and the resulting states. This is because the nonzero inputs required to hold these positions result in a nonzero input penalty term. Any attempt to decrease the input penalty resulted in system instability. The addition of a pregain term

is a classical method in control theory that addresses this problem. In this section, we introduce a data-driven method to compute the pregain using a static Koopman operator, which we term the static Koopman pregain.

A core assumption of this component of our model is that when held for enough time, all transient dynamics dissipate, and the robot achieves a static pose. Therefore, the set of admissible step inputs u_{static} corresponds to a set of input-mediated fixed points x_{static}. We seek a mapping from the data matrix of step inputs, U_{static}, to the data matrix of stationary states, X_{static}. Ideally, this mapping would be linear to enable us to use fast, optimal control. The Koopman framework usually requires the domain and range to be the same, but this requirement can be relaxed if we consider the static Koopman operator [86]. The static Koopman operator contrasts with the dynamic Koopman operator, which describes the evolution of observables $f : M \to \mathbb{R}$ under the action of the mapping $T : M \to M$. If we define observables on the inputs as $g : \mathbb{R}^p \to \mathbb{R}$, the static Koopman operator $\mathcal{K}_{\text{stat}}$ is defined as

$$\mathcal{K}_{\text{stat}} f(x_{\text{stat}}) = g(u_{\text{stat}}). \tag{4.29}$$

We desire to approximate the action of the static Koopman operator with a finite dimensional matrix G. To do so, we first construct the data matrix U_{static} with unique step inputs as the columns of the matrix. By feeding these inputs to the system and allowing transient dynamics to dissipate, we are left with a unique stationary state, x_{static}; these states represent the columns of X_{static}. The matrix G is then computed using

$$G = U_{\text{static}} X^{\dagger}_{\text{static}}. \tag{4.30}$$

The matrix G serves as a linear mapping from stationary states to inputs.

Finally, we are ready to bias our control law with the addition of a feedforward pregain

term Gz_{ref}, resulting in

$$\begin{aligned} u_i &= -K(z_i - z_{\text{ref}}) + Gz_{\text{ref}}. \\ z_{i+1} &= Az_i + Bu_i \\ x_i &= Cz_{i+1}. \end{aligned} \tag{4.31}$$

This signal is the optimal stabilizing solution taking the present initial state to the desired state, x_{ref}.

As shown in Fig. 4.9, the pregain term $u_{\text{stat}} = Gz_{\text{ref}}$ outweighs the dynamic term $u_{\text{dyn}} = -K(z_i - z_{\text{ref}})$ in most tests. This allows the input penalty weights in the dynamic term to be optimized without fear of sacrificing steady-state error. Also, the static Koopman term provides enough of a steady input to counter the fluctuations caused by measurement noise introduced by the state measurements in the dynamic term. This is the reason our system does not experience the destabilizing effects of noise in fast-moving reference tests described in [13].

Training and Observables

With the mathematical underpinning of our modeling and control methodology described (see Supplementary Fig. A.4), we now turn to the particular choices made to suit our particular robotic applications. Given the soft arms described in Section 4.3.5 we collect training data through a series of experiments, performed by commanding step inputs with randomly distributed magnitudes. The only prior knowledge of the soft arm's dynamics required is an upper bound for the length of time required for the dissipative dynamics to die down while inputs are held. Each step input is held for this amount of time so that the soft arm converges to a steady state, efficiently probing both the dynamic and static response. The data is separated into training and validation sets, and the training data is further partitioned into dynamic and static components which

are used to train dynamic and static Koopman operators (see Section 4.3.3).

Choosing observables is difficult in practice. We choose to implement DMDc with time delay observables (also known as Hankel DMDc) because of their provable convergence as the number of time delays goes to infinity under certain assumptions on the dynamics [100,102,122]. In reality, adding more time delays gives a diminishing return in prediction accuracy (see Fig. 4.13A). A single time delay with hundreds of monomials is used in [82–85], but we find that time-delay-only observables offer better results, with improvements in reconstruction with up to ten observables (See Fig. 4.13A). To create our observables, we use the current measurement of the X-Y-Z positions of the motion trackers x_k and append two time-delayed versions of the same states $z_k = [x_k \; x_{k-1} \; x_{k-2}]^T$. Each time delay looks 1/60 seconds into the past. This proves to be sufficient for closed-loop control. For reconstruction, more time delays give further increases to the model's accuracy, as shown in Fig. 4.13A.

The synergy of step inputs and time delays allows the discovery of system eigenvalues in the important 1 to 5Hz range (the span of natural frequencies of the arm), as shown in Fig. 4.8. Without time delays, these eigenvalues and their corresponding Koopman modes are missed (Fig. 4.8). For comparison to the Koopman model used in [82], we tested the addition of monomial observables was tested up to order 4 with no new dynamic modes of any meaningful mode power learned. Monomial observables also failed to give any improvement to the reconstruction or closed-loop pointing accuracy of the model and controller (Fig. 4.13).

With the goal of minimizing training time and model complexity, we found that up to five time delays and one minute of step input training is best for modeling our system before considering control, but only two time delays and five minutes of step input training is ideal when control is considered. We first compared the prediction ability of different dynamic Koopman models as we varied the number of time delays and

total training time (Fig. 4.13A). The addition of a single time delay substantially reduced error, however additional time delays continued to offer marginal improvements up to five delays. We also found that after only approximately one minute of training, the model reached its minimum error. Second, we built Koopman-LQR controllers as described in Section 4.3.5, augmented with a static Koopman operator as a pregain term, with varied time delays and training time. We then quantified the error with closed-loop control (Fig. 4.13B). In this case, two time delays outperformed one delay, but was comparable to three or more, resulting in our decision to use two delays for control. We also found that after approximately five minutes of training (fifty unique step inputs), the error converged; we used this amount of training time for the remaining experiments. Note: a direct linearization of the system was unstable during controlled motions, suggesting the nonlinearity of the system.

Robot Design

For this investigation, we constructed two distinct soft arms to evaluate the viability of the proposed methodology across nonlinear dynamical systems. For each, we aimed to meet the following objectives: a) high-deflection, nonlinear dynamics for which linearization fails; b) inertial dynamics, for which quasi-static approximations fail; c) enough morphological diversity such that their analytical models would be not readily transferrable.

To this end, the first arm was designed to have four actuators (two antagonistic pairs) longitudinally aligned with the main body to produce planar actuation. This design is behaviorally similar to others present in the literature ([97,98,125]). When fabricated with appropriate pretension, this construction allows for approximately 110° of curvature when fully actuated. With a length of 45 cm and a maximum diameter (main body diameter plus the diameter of the fully inflated muscles) of 6.25 cm, the slenderness

ratio of this device was 7.2 (the ratio of length to max diameter).

The second arm was designed with three actuators, all of which were affixed to the body such that a torsional deflection would be induced when inflated. This produces a helical actuation that is markedly different from that of the first embodiment. With a length of 53 cm and a maximum diameter of 3.8 cm, this device exhibited a slenderness ratio of 13.9. The muscles were affixed with pretensions such that, when fully actuated, this device is capable of achieving approximately 180° of curvature.

For objective a), with an angle of curvature of at least 110° for both arms, the nonlinearity metric is well achieved (See Fig. 4.8). For objective b), both systems were fabricated out of airtight fabric, utilizing fabric pneumatic artificial muscles (fPAMs) as described in [39], which exhibit a fast response time and low hystersis (on the order of 1%), achieving accelerations in excess of g. For c), the factor of approximately two difference in slenderness ratios, the change in actuator numbers, and the inclusion of helical actuation all combine to produce two systems with meaningfully different behavior (see, for example, the model presented in [40] compared to [104]).

Robot Fabrication

Both arms were constructed out of 30 Denier silicone-polyurethane impregnated ripstop nylon (Sil-nylon, Rockywoods Fabrics), actuated by fabric pneumatic artificial muscles (fPAMs) [39] built out of the same material. The main body was fabricated such that one side of the fabric weave cell was parallel to the longitudinal axis, the other perpendicular. This orientation makes the soft arm axially and transversely stiff, but torsionally compliant. The muscles were fabricated such that each side of the cell was offset by approximately 45° with respect to the longitudinal axis, which instead makes the actuator torsionally stiff but compliant axially and transversely. Moreover, when these muscles are inflated, they shorten in the longitudinal direction as a McKibben does, up

to 35% based on the pretensioning induced during adhesion to the main body.

Each of these components was cut from a sheet of fabric, rolled into a tube, and sealed with a lap joint using RTV silicone adhesive (Smooth-on Silpoxy). Once each component was fashioned, a jig was produced to hold the main body and pretensioned muscles in place while the RTV cured. Finally, in between each muscle a fabric sleeve, exhibiting the same fabric bias as the muscles, was attached to the main body to allow for motion capture tracker wires to be routed without occluding the view of the LEDs.

Pneumatic Circuit Design

Each soft arm body was held at a constant pressure of approximately 1 bar for the entirety of testing, supplied by a discrete source. For each muscle of both soft arms, Festo VEAB-L-26-D2-Q4-V1-1R1 proportional pressure valves were used to command individual pressures continuously. These three-port valves were chosen for three reasons: their fast response times (<10ms); accurate response (0.75% full-scale absolute accuracy, 0.4% full-scale repeatability error); and the ability to accept forced exhaust through their third port. However, this accuracy requires a lower flow rate, which precluded the use in the much larger main body (due primarily to persistent leaks). Additional information on the general control circuitry configuration can be found in the Supplemental Information.

4.3.6 Acknowledgments

Funding: This work was supported in part by the National Science Foundation grant no. 1935327 and the ARO-MURI W911NF1710306: From Data-Driven Operator Theoretic Schemes to Prediction, Inference, and Control of Systems. Part of the work performed by Ervin Kamenar was funded via Fulbright foundation. **Author Contributions:** D.A.H. designed the robots and test apparatus, wrote the manuscript, prepared videos, and performed experiments. M.J.B. designed the modeling and control algorithm, prepared figures, and wrote the manuscript. E.K. designed the electronics, performed experiments, and wrote the manuscript. A.C. ran experiments, performed analysis, and prepared figures. P.C.C performed experiments. I.M. advised the design of the modeling and control algorithm, the paper, and experiments. E.W.H. advised the design of robot, wrote the manuscript, and advised the paper and experiments. **Competing Interests:** The authors disclose no conflicts of interest. **Data and Materials Availability:** All (other) data can be found in the Supplementary Materials or at `https://doi.org/10.5281/zenodo.8184777`

Chapter 5

Ongoing Projects: Semi-autonomous, Soft Robotic Airway Management

A significant component of my work over the past 5 years has heretofore gone unpublished. Not exactly chronological, this project has gone through fits and starts as I focused on the preceding chapters. However, while it has traditionally been relegated to just a side project, it is finally blossoming into its own concern. That concern is soft robotic medical devices, specifically soft robotic airway management.

5.1 Background

This work began in 2019, when an anesthesiologist from Stanford, Dr. David Drover, reached out to my Ph.D. Advisor, Elliot Hawkes, with a question: can soft robotics address a critical unmet need in airway management? This inquiry set into motion an ongoing collaboration with Dr. Drover, that has led us through every airway mannequin known to man, drawn us north, south, and east in search of a large sample of cadaver airways, and ultimately fostered the founding of our small startup, Vine Medical.

While this project is still far from "done," it has gone through a fascinating evolution from inception to its current embodiment. Of all my projects in graduate school, this is the first that stacks nonlinearities - both of the system and of the environmental substrate - with a very small margin for error. Ultimately, it has proven to be my most difficult challenge yet: attempting to develop a single, semi-autonomous, universal intubation system that competes with experts in terms of success rates and success times.

This chapter describes the detailed engineering that has gone into the device over the past 4 years, and describes some of the open questions that are on the horizon.

5.1.1 Abstract

For over a century, medical practitioners have struggled with the challenge of intubation. Evolution has designed an airway that effectively rejects foreign objects - the glottic

structure is easily covered by the protective epiglottis, located anterior to the esophagus and hidden behind the soft palate; and the highly sensitive vocal cords are controlled by the vagus nerve, reacting to minor stimulus at very low levels on consciousness [126].

As such, proper airway management demands the provider have a simultaneous breadth and depth of expertise to properly visualize the glottic structure, identify the cords, and deliver a semi-rigid tube around the nearly 270 degrees of curvature that defines the upper airway. Such a feat can be difficult to achieve in a controlled operating room, and this difficulty only compounds as the environment becomes more dynamic, including everything from the emergency department to the battlefield. As such, anesthesiologists with decades of experience are widely seen as the airway experts but few sites of care have access to such skill – in the OR, most first-pass intubation failures occur during "unanticipated difficult airway" cases (present in ∼3% of cases [127,128]), yet with lower expertise and less structure outside the OR, failure rates are much higher: approximately 35% in the prehospital setting and 15-20% in the emergency room (ER) [129–132], with up to 33% of failed intubations resulting in complications ranging from hypoxia to cardiac arrest [133–136].

The presented work addresses this problem by leveraging recent innovations on tip-growing, soft systems, and presents an autonomous, soft, self-contained and self-deploying endotracheal tube. The Origin ETT to date has: in anatomically-correct mannequins, achieved a first-pass intubation success rate of 94%, competing with the skill of anesthesiologists in the operating room; in fresh-frozen cadavers, achieved 84% first-pass intubation success rate, rivaling emergency medicine doctors using video laryngoscopy. Yet critically, it reaches these performance benchmarks in the hands of medical laypeople. Thus, the presented device for the first time enables the deployment of a definitive airway, in any circumstance, in the hands of any provider.

5.2 Introduction

Artificial airways are an integral component of care in both the operating room (OR) and in emergency medicine. Currently, providers have two choices: a definitive, infraglottic airway (IGA) via an endotracheal tube (ETT) or tracheostomy tube; or a non-definitive, supraglottic airway (SGA), such as the larnygeal mask airway (LMA) or laryngeal tube (LT). In most sites of service, the IGA is the "gold standard" of care for its ability to both prevent aspiration, and deliver reliable ventilation more repeatably than an SGA. Amongst IGAs, ETT intubation is overwhelmingly preferred due to its minimally invasive nature compared to tracheostomy and cricothryoidotomy tubes [137].

Current intubation techniques involve visualization and manual guidance of the ETT into the trachea, but placement requires anatomical knowledge and skill, often only possessed by anesthesiologists with decades of experience, and is often complicated by circumstantial difficulties in emergent scenarios [129–131,133,138–140]. In the OR, most first-pass intubation failures occur during “difficult airway” cases (present in $\sim$3% of cases [127,128]), yet in less controlled environments outside the OR, failure rates are much higher: approximately 35% in the prehospital setting and 15-20% in the emergency room (ER) [129–132], with up to 33% of failed intubations resulting in complications ranging from hypoxia to cardiac arrest [133–136]. Even more alarming is the fact that military medics have largely forsaken intubation, relying on the SGA or invasive airway access to provide emergency ventilation [141].

Technological attempts to address the challenge of intubation have relied upon improved visualization tools such as the video laryngoscope and the video stylet. But while these devices aid in improving glottic view, they still require advanced anatomical knowledge and well-honed technique to effectively pass them through the airway to facilitate intubation. As a consequence, the benefits of such devices tend to befall the experts, not

the novices [133,139,140].

Such limitations are exactly the motivation for the field of soft robotics. Instead of rigid devices that, while repeatable, are prone to circumstantial and operator misuse or failure, soft systems embody a mechanical intelligence that offloads a significant amount of user skill and fosters resilience. Here, we present the world's first soft robotic intubation system. By leveraging vine-inspired tip-growth [26], in which a soft tube extends from its tip into complex shapes driven only by a low internal air pressure, we have designed a system that is nearly provider agnostic, showing equivalent performance in the hands of both anesthesiologists and paramedics. The proposed technology could provide: in the OR, oxygen to surgical patients with an unexpected difficult airway in seconds; in every ER, it could serve as a life-saving rescue device when patients are critically in need of oxygen; in every ambulance, it could supplant existing airway devices (SGAs and BVMs) that do not intubate.

5.2.1 Soft robotic airway device design requirements

The human airway is unique in that it has been designed by thousands of years of evolution to reject all foreign objects from entering, even in a significantly injured individually. The result is a trachea that hides behind the base of the tongue, more than 90 degrees from the oral axis. The larynx includes complex musculature that is controlled via the most fundamental aspect of the central nervous system (CNS) - the vagal nerve - that snaps shut with the smallest hint of intrusion. Finally, the pharynx has a variety of anatomical features to further protect the larynx from foreign materials, including the epiglottis, which closes from the anterior surface to redirect food and liquids into the esophagus, and the arytenoid cartilages, which both create a step from the pharyngeal axis to the laryneal axis and closes from the posterior side to seal off the larynx within

the closed epiglottis [126].

Airway management capabilities vary wildly depending on site of service (i.e. operating room (OR), non-OR hospital such as emergency department (ED) or intensive care unit (ICU), or pre-hospital), provider skill (anesthesiologist, emergency medicine physician, respiratory therapist, paramedic), and the type of health system (Level I-V trauma center, academic vs community medical center, public vs private emergency medical services (EMS) agency).

In the operating room (OR), airway management conditions are normally extremely controlled and routine [137]. Before the procedure the anesthesiologist will do an awake airway exam, giving them some insight into the anatomical constraints they will face when intubating. Based on this exam, once in the OR, as many tools as the doctor anticipates needing are readily available. The patient is positioned in a favorable orientation (supine with shoulders lifted, head in the sniffing position, table at proper height for the provider) and preoxygenated. The fasted patient is then anesthetized and sedated, stopping all respiratory effort with 60+ seconds of oxygen reserve. The anesthesiologist then quickly advances the ETT into the airway and resumes ventilation. The only time these cases go awry is when unanticipated difficulties are encountered - anatomical constraints the MD could not predict from an external evaluation alone (such as an anterior airway, floppy epiglottis, an airway mass of some sort). With the combination of environmental control and provider skill, failures only happen $\sim$3% percent of the time, but correspond to 105% increase in cost [127,128,142].

In the hospital but outside the OR (i.e. in the emergency department (ED) or intensive care unit (ICU)), circumstances are rarely as favorable. Patients are rarely fasted, often with blood or vomit in their airway. Their respiratory reserve could be completely expended, and preoxygenation could be failing. Many times they will be actively undergoing CPR, which bucks the body up, down and side-to-side. The doctor has no opportunity

to do a pre-procedure examination, and has no idea what they will encounter anatomically. Luckily, the doctor will likely have multiple nurses available to help, hopefully have access to multiple tools and technologies, and in the case of Level I and II trauma centers, should have an anesthesiologist on-site to help. In these environments, success rates range from 72% to 85% percent first-pass, but correspond to high complication rates of up to 45% (including hypoxemia, hypotension, cardiac instability) [129,131,133,138].

In the pre-hospital environment, things become even more complicated. Not only does all the above hold, but lighting will be inconsistent; patient positioning could range from behind a toilet to upside down in a rolled car; loved ones could be screaming in the next room; the paramedic and EMT might be the only two providers on-scene. The paramedic may or may not have access to video laryngoscopy, and may have only trained a few hours on mannequins this year. With such variability in procedure scenarios, nationally paramedics can only achieve approximately 65% first-pass success [130,132,140,143].

Finally, in the military environment, medics are subject to even more complicated circumstances with even less training, while being tasked with providing care to team members with whom they have deep relationships. There could be gunfire and artillery, it could be night time, it could be your best friend on the team, and you have the training of a civilian EMT. Intubation is so fraught with failure in these environments, practice guidelines (the Tactical Combat Casualty Care (TCCC) manual) recommends either an SGA placement or invasive airway access - a cricothyroidotomy [141]. Psychologically, the decision to cut ones neck is often nearly insurmountable. It is for these reasons, that airway mismanagement is the second leading cause of preventable death in the military, behind only hemorrhagic death [144–146].

Given the current state of airway management practice, the primary goal of a novel airway device is to attempt to normalize performance across site of service and provider skill. Therefore, the design objective should seek to meet or exceed the national average

for first-pass intubation success regardless of provider skill, with a clinically relevant time to intubation, while producing no more adverse events than current intubation practice. That is, the population-level first-pass success (FPS) should achieve the weighted average for all intubations completed on a national basis, such as is described in (5.1). Clinically relevant time to intubation is qualitatively set to "as short as possible", with a firm upper limit of less than 180 seconds (the time it takes for preoxygenated patients to drop below 90% SA_{O_2}) [147]. Complication rates follow a similar determination as (5.1), based on findings in [133,148].

$$\begin{aligned} \text{Weighted Average (WA)} &= PI_{OR} * FPS_{OR} + PI_{IH} * FPS_{IH} + PI_{OH} * FPS_{OH} \\ &= 0.88 * 0.95 + 0.08 * 0.85 + 0.04 * 0.65 \\ &= 93\% \text{ FPS} \end{aligned} \tag{5.1}$$

where PI_{XX} is the percentage of intubations completed in a given environment, with $XX \in \{OR, IH, OH\}$ describing the Operating Room (OR), in-hospital non-OR (IH), and out-of-hospital (OH).

5.2.2 Designing for simulant: mannequins

Airway mannequins are the primary method for non-clinical airway management training, due to their wide availability, relatively low cost, and high variation in the anatomical representation. Thus, the logical first step in this endeavor was to prototype and test on mannequins.

Leading providers for these simulators include Ambu (Ballerup, Denmark), Laerdal Medical (Stravanger, Norway), and TruCorp Ltd (Lurgan, UK). Mannequins from each provider were acquired, representing 5 different airway anatomies [149–153]. In each, in

concert with Dr. David Drover (Professor of Anesthesiology, Stanford University), we identified the primary design variable as the incisor-to-glottic distance (ITG). Supplmenting our mental model with the normal variation of the anatomy as presented in [154,155], we sought to design a system that: (i) datumed against the incisors; (ii) advanced from the incisors to the oropharynx; (iii) turned inferiorly to access the hypopharynx; (iv) first extended into the esophagus to block that pathway; (v) branched at the appropriate depth anteriorly into the trachea (Fig. 5.1A-D. Importantly, step (v) needed to have sufficient range to cover the vast majority of the adult human population, which we quantitatively set at three sigma (99.7%)).

Testing was conducted in each of the mannequins previously described, with the objective of finding the range of depths for which a given device would still effectively intubate. It was found that, on average, a device could intubate within $\pm$1.5cm of the tracheal opening. Using the models provided in [154,155], these findings allowed for the creation of three sizes that effectively covered the adult population to the design specification described above (as shown in Fig. 5.2).

With the mannequin airway morphology readily known, the design intent was to optimze the performance in each of the (i)-(v) steps listed above. This included designing an improved mouthpiece that reliably datumed off the incisors in the appropriate form-

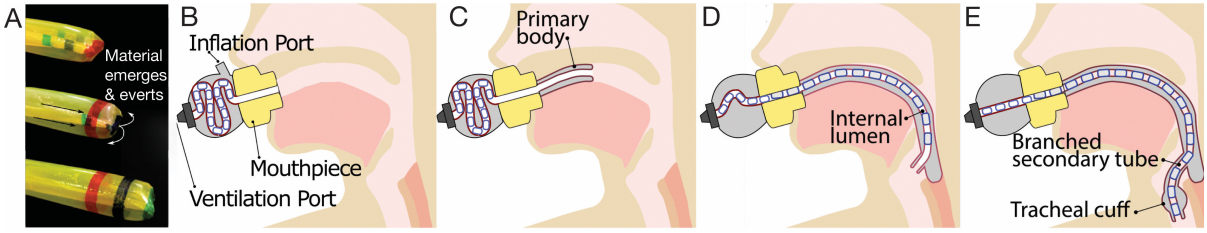

Figure 5.1: Illustration of proposed device. (A) Eversion process explained. (B) Mouthpiece is placed. (C) With inflation, primary body grows towards pharynx. (D) Soft primary body conforms to anatomy while pulling soft internal tube. (E) Secondary body branches anteriorly, passively deforming as necessary to enter trachea and deliver soft internal tube. After deployment, cuff is inflated to secure airway.

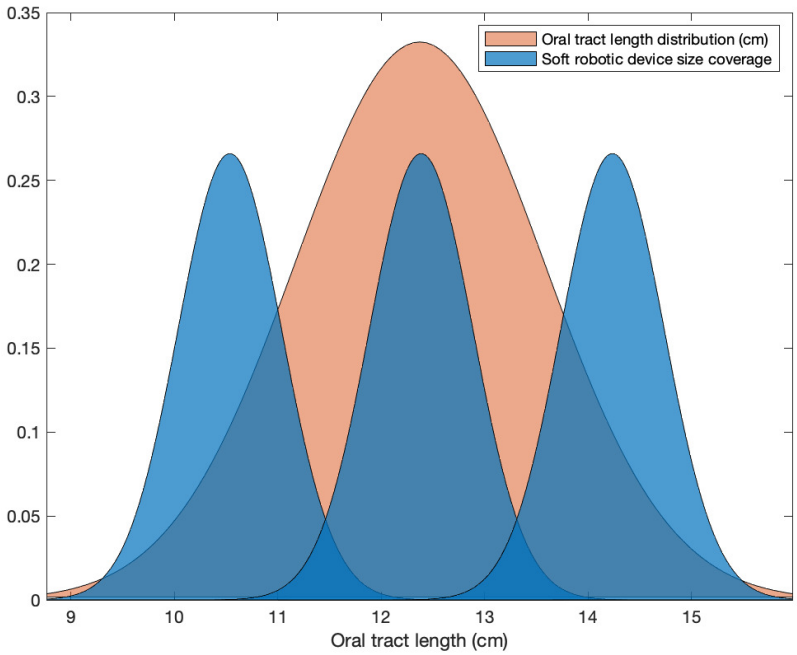

Figure 5.2: Distribution of normal airway tract lengths, overlaid by sizes selected to cover 99.7% of adults

factor; identifying the best spline for the primary body (Fig. 5.1C) to account for varying oropharyngeal depths; defining the optimal branch distance at a given size; and refining the branch geometry and internal ETT configuration to mitigate the pressure (and as a consequence, force) required to access the trachea. Such design efforts were driven by insights gained from Chapter 2; specifically, (2.6) and (2.9) gave force and pressure insights that informed both the primary body spline and the branch geometry. This design culminated in that shown in Figs. 5.3 and 5.4.

This design was then tested in each of the mannequins described above. Twenty tests were performed in each mannequin airway with a single device. After 5 tests in each mannequin, manufacturer-provided lubricant was reapplied to overcome the non-realistic friction produced by their silicone construction. Inflation was provided by a hand pump capable of producing 35 kPa of air pressure. Time to intubation was defined

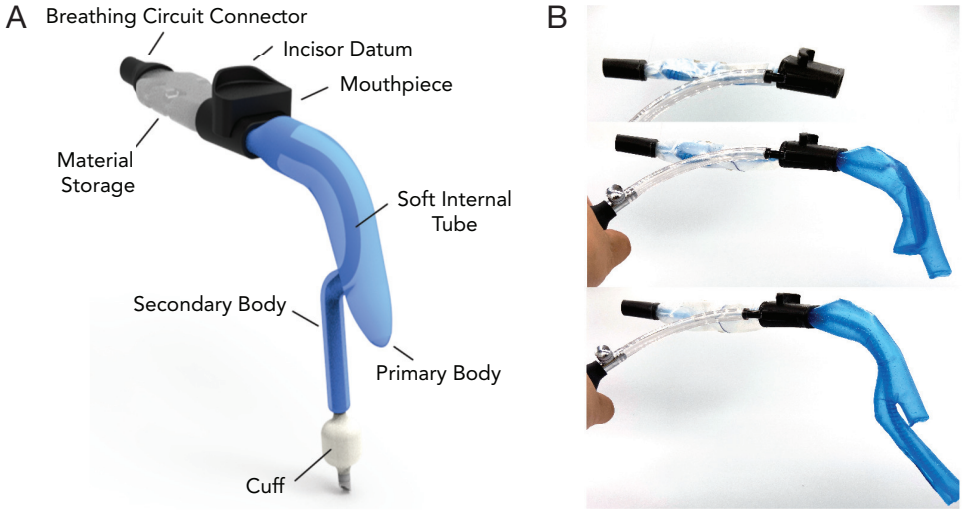

Figure 5.3: (A) Render of the device with all critical features shown (fully deployed state). (B) Sequential deployment of a complete prototype: the primary body first grows into the esophagus, then the secondary body branches anteriorly into the trachea.

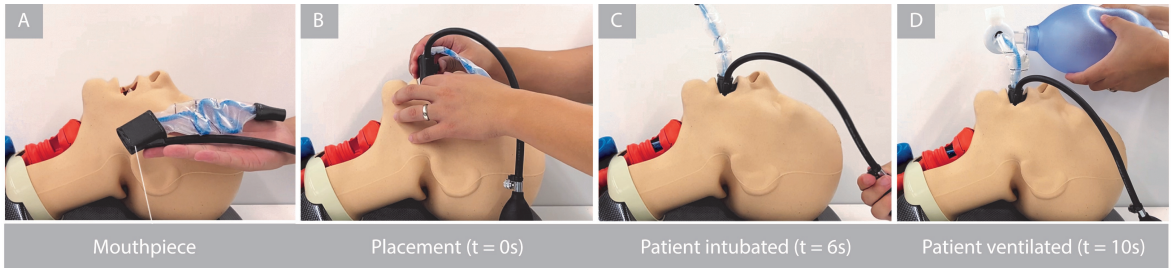

Figure 5.4: (A) The mouthpiece, which houses the body material, is shown. (B) Device is placed in patient's mouth. (C) Device is inflated with the included hand pump, autonomously navigating to the trachea in 6 s. (D) A standard bag resuscitator is connected to the breathing port, ventilating the patient.

as the time from the introduction of the mouthpiece until full eversion in the trachea; first-pass success was recorded if the device full everted into the trachea under only the influence of supplied air pressure. These results are shown in Table 5.1. Of note: while an in-line pressure gauge was not included for the above testing, all successes occurred under the 35 kPa limit of the hand pump; additionally, while intubation time was not tracked, successes occurred in as little as 6 seconds. The next step was to translate this design to a more representative simulation environment for verification and validation:

TruCorp "normal" airway ([152])	TruCorp "difficult" airway 1 [153]	TruCorp "difficult" airway 2 [153]	Laerdal "normal" airway [150]	Laerdal "difficult" airway [151]	**Average first-pass success**
20/20	19/20	18/20	18/20	19/20	**94%**

Table 5.1: First-pass success rates in various industry-standard training mannequins, including simulated edema and elongated epiglottis. Average first-pass success rate across anatomies is 94%.

fresh-frozen, unpreservered cadavers.

5.2.3 Designing for simulant: cadavers

The above-described results were observed in March and April of 2022. While we had done some initial cadaver testing to confirm our mannequin results, the sample size was quite small to this point ($n = 6$). In those tests, we observed reliable success in 4 out of 6 of the specimens, with the other two inconclusive for a variety of reasons (immature testing protocols, inadequate analytical equipment, etc.). Consequently, in May of 2022, as we made the conscious decision to validate our mannequin-inspired design, our null hypothesis was that the device would change marginally over the coming 2-3 months to maximize performance, and that we would be manufacturing devices by the end of the year. That hypothesis was wildly incorrect.

In designing for mannequins, we went through the process of identifying key variables, implementing model-based design to hit certain specifications, tested and iterated. This design cycle resulted in a highly reliable system, but the key assumptions were wrong: mannequin anatomy and tissue dynamics are not representative of human tissue, except as a proxy for laryngoscopy. This realization sent us back to the top of the design waterfall. This process is shown visually in Figure 5.5, as new components began incorporation into the device.

The most important differences between mannequins and cadavers are two-fold: 1)

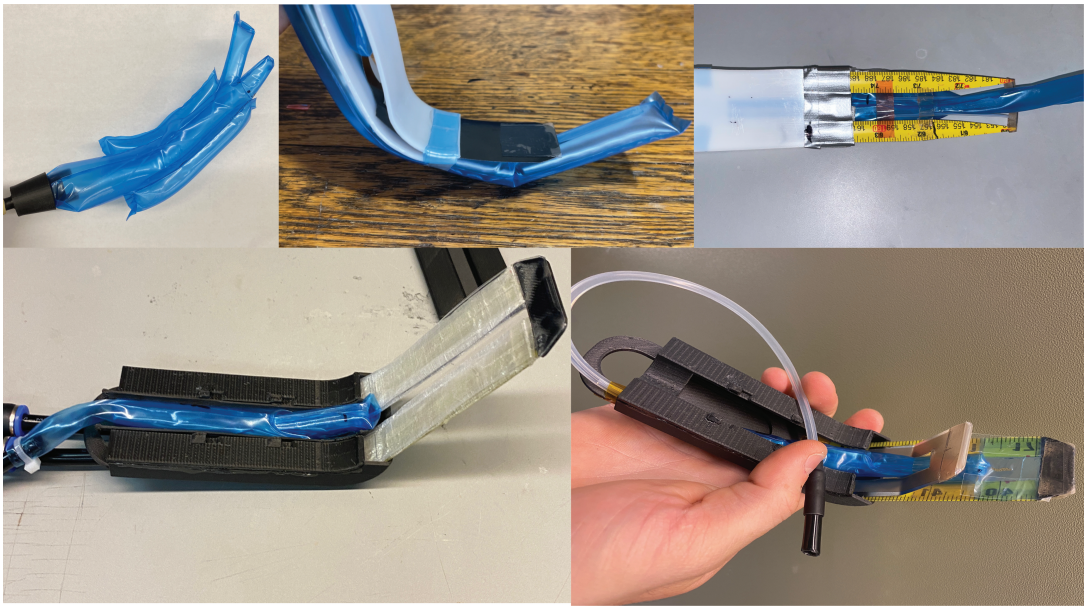

Figure 5.5: Design iterations as a function of additional cadaver results. From top left: fully soft system slowly incorporating more rigid features to defeat the epiglottis and properly index in the anatomy. Bottom right: early version of the near-final design.

in mannequins, the anatomy from oral cavity to esophagus is wide open; in cadavers, the anatomy collapses against the pharynx. 2) in mannequins, the airway anatomy (e.g. epiglottis, arytenoid cartilages, vocal cords) is quite rigid; in cadavers, these are all significantly more flexible, and vary significantly in their size, shape, and stiffness. Moreover, the size and shape of the upper airway can change drastically across heights, sexes, and BMIs – features that are inadequately captured by the mannequin environment. Thus, the effort restarted to identify key variables and understand tissue dynamics, to design concepts capable of navigating the airway effectively, and to iterate across a statistically significant sample of unique cadaver airways.

The primary design difficulty in developing a highly reliable, higly robust, semi-autonomous, universal intubation system is the fact that the airway is at an unknown distance, at an unknown height, hidden behind an epiglottis of unknown length and unknown mechanical characteristics. This effort led us to seek anatomical landmarks

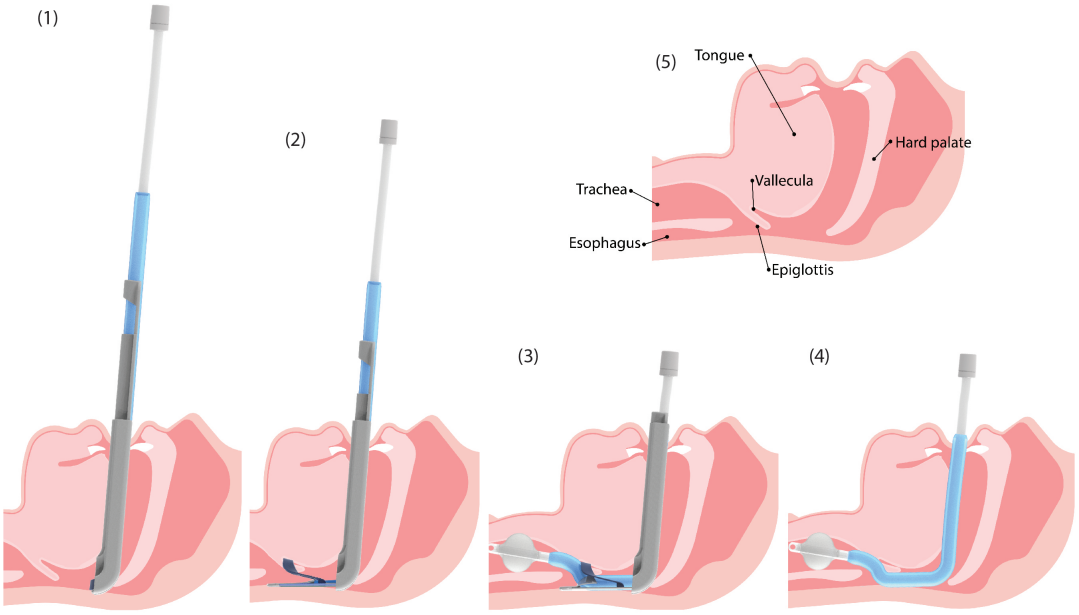

Figure 5.6: Four-step deployment of the current design. First, the introducer is advanced to the oropharynx, where it naturally stops. Second, the bi-stable assembly is advanced until it engages with the vallecula. Third, the toroidal ETT sheath is advanced into the tracheal. Fourth, the cuff is inflated and the introducer is removed.

against which we could reliably datum, and from which other anatomical features would be reliably distributed. Ultimately, this resulted in a significant design update: the mouthpiece morphed into an "introducer" that indexes against the oropharnygeal wall instead of the incisors; the primary body evolved into a bi-stable assembly that datums against the vallecula and glossoepiglottic folds; and the intubating vine no longer includes an esophageal branch, but instead a vestigial nub on its posterior side. These steps are shown in Fig. 5.6.

The result, shown in Fig. 5.7, describes a device that enables: (i) a one-size-fits-all constructions, where the plunger throw accounts for the entire oral tract length distribution shown in Fig. 5.2; (ii) a three-step deployment, which early usability studies have shown are easily interpretable to both highly skilled anesthesiologists and paramedics, and that takes an average of less than 30 seconds to deploy; and (iii) a detachable design,

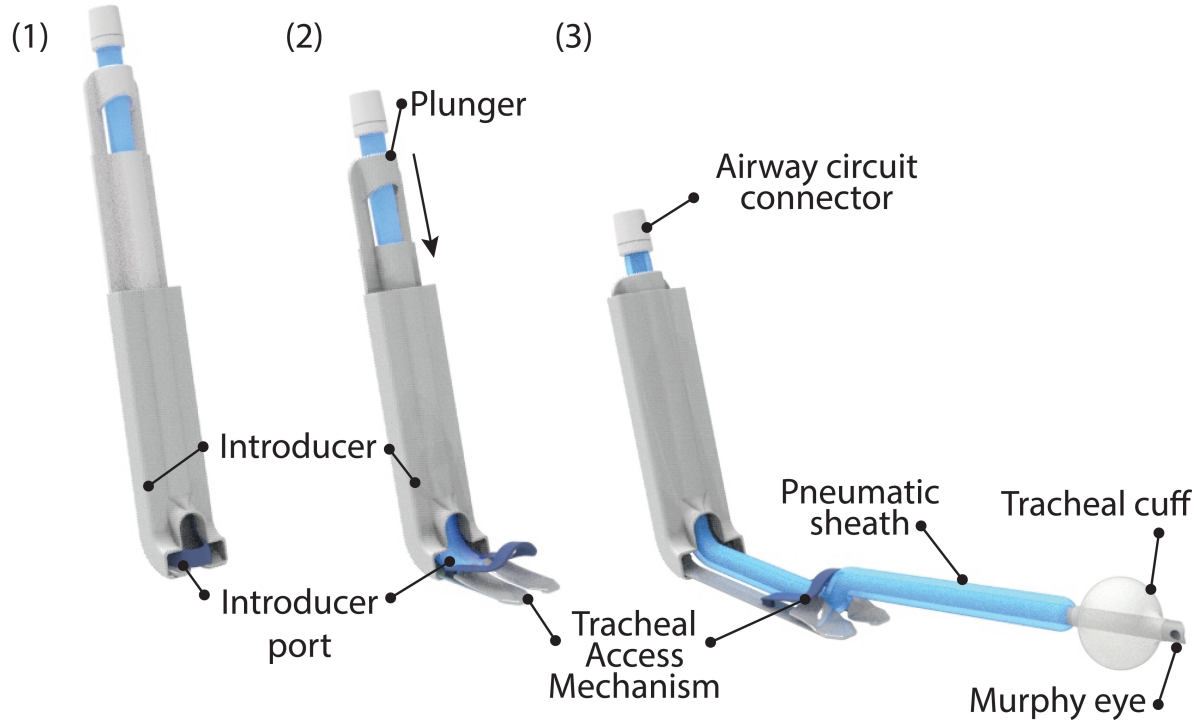

Figure 5.7: Render of new product

that enables the introducer to be removed after intubation leaving only the ETT and the vine overtube / pneumatic sheath in place.

5.2.4 Preliminary results

While testing has been completed in approximately 50 cadavers to date, much of that testing had been done on iterations so obsolete that they have little relevance to the current performance of the device. That said, the previous approximately 20 specimens have been used for a highly similar embodiment to the current state-of-the-art, for which performance has been tracked. A few caveats: 1) with the device still undergoing modifications, the definition of success has been broadened to include failures for which small modifications then enable success 2) the tracheal access mechanism has changed significantly since May, but the previous tracheal access mechanism is treated similarly.

Specimen Type	Successful Specimens	Total Specimens
Full-body cadavers	**16**	**18**
2/15/23	3	3
2/17/23	2	2
5/5/23	2	2
5/31/23	5	6
6/12/23	4	5
8/22/23	4	4
Cadaver "busts"	**2**	**3**
Cadaver heads	**5**	**6**
Total	**27**	**31**

Table 5.2: Overall success rates in 31 unique cadaver specimens. Success rate is currently estimated to be 87% as of 8/22/23

Results are reported in Table 5.2, showing approximately 84% overall success across 26 specimens. This corresponds to the average first-pass success of an emergency medicine doctor, and is something we are actively working to improve. Ongoing work is focused on increasing the range of operation (on both tails of the distributions), improving tracheal access mechanism performance, and bettering the user experience features to minimize procedure time.

5.2.5 Limitations of simulation environment

As is described above, the transition from mannequins to cadavers unearthed significant translation error due to a low resolution simulation environment. This is still expected to be true in the case of cadavers to live humans, but to a significantly lower degree.

The primary limitation of the cadaveric environment is the lack of tissue perfusion.

In a live human, blood pressure and flow produce good skin turgor – the ability for the tissue to return to its original state after force application. This is obviously absent in the cadaver model, and applied force results in a progressive "draining" of the fluid within the tissue that gives it structure. In particular, the tongue gets progressively flattened as more and more blood is emptied during intubation attempts, with both the described device and with traditional tools. Ultimately, there is a threshold beyond which the tissue is no longer a realistic representation of the live human case, and this complicates failure mode analysis and the subsequent design iteration. Luckily, there exist methods to simulate perfusion in the cadaver model, which we plan to include in the upcoming cadaver trial, as described in Section 5.2.6.

Additionally, a significant number of our design specimens have been dissected cephala that only include a few c-spine vertebra (between c-4 and c-7). These dissections were chosen for their lower price than full bodies, and the ease with which they could be stored, thawed, and tested. Unfortunately, the airway cuts eliminate some level or anatomical constraints that would otherwise be present between the larynx and surrounding tissue. This complicates the understanding of how forces applied at the device level translate to tissue interaction. With this in mind, recent testing has been confined to full bodies or cadaver busts, which have been dissected at approximately the nipple line.

Rigor mortis is another issue with the cadaver model. After expiration, muscle tissue becomes effectively locked in place and requires excessive force to mobilize it compared to a live person. This results in limited head and neck mobility of our models, and thus complicates intubation. However, of all the limitations, we believe this aspect actually serves to improve the resiliency of the design, and that performance will improve when rigor mortis is no longer a feature.

5.2.6 Future work: head-to-head cadaver trial

While this device has a long road to clinical and commercial significance, the next step on the journey is quite clear: complete a protocol-controlled, head-to-head cadaver study that seeks to show the expected value proposition: expert-level performance in a provider-agnostic package. To that end, we have designed a study protocol that aims to capture the challenge of intubation at the upper and lower ends of the skill spectrum.

Anesthesiologists are the airway experts, and while they primarily intubate in the controlled OR, they are regularly called to assist in emergent intubations in the emergency department and ICU. Paramedics are tasked with intubating when circumstances indicate it, which could range from a cardiac arrest in the back of an ambulance to the side of the road after a car accident. Thus, the two cases we seek to recreate in a simulated environment are: Case 1 - an unsoiled, controlled airway similar to the OR or a cardiac arrest; Case 2 - a soiled, emergent airway similar to a severe trauma event. The protocol for said test is as follows:

1. **Provider selection:** Four skilled anesthesiologists to represent the highest level of performance. Four novice paramedics to represent the low end of the skill spectrum. **Desired endpoint:** performance normalization (even if that is reduction in performance by anesthesiologist in some cases).

2. **Cadaver selection:** Certain externally identifiable characteristics capture the span of humans, and serve as a proxy for “variable anatomy". We then seek to select cadavers that satisfy the below combinatorics shown in Table 5.3. Ideally, we acquire an even split of: male / female; over / under 5’7”; over / under 30 BMI; over / under 50 years old. Minimally, we require: 60/40 male / female split; 70/30 BMI split (over/under 30 BMI, can be split in said proportion on either side), e.g. 16 cadavers that satisfy male/female, tall/short, high/low BMI, old/young. With

soiled / unsoiled, we have 32 combinations from 16 cadavers.

Specimen	Male	Tall	Hi BMI	Old
1	X	X	X	X
2		X	X	X
3	X		X	X
4	X	X		X
5	X	X	X	
6	X	X		
7			X	X
8		X		X
9		X	X	
10	X			X
11	X		X	
12				X
13		X		
14			X	
15	X			
16				

Table 5.3: Combinations of variables of interest. Note: not male = female; not tall = short; not Hi BMI = low BMI; not old = young

3. **Protocols:** We will have each provider intubate using traditional methods on 2 cadavers with clean airways (with anesthesiologist grading the airway), followed by two cadavers with soiled airways and C-collars (using vomit found in [156] with slight modifications). In both cases, we will measure FPS, overall success, time to intubate, perceived difficulty. This is followed with intubations using the subject device, tracking the same elements. This corresponds to 32 attempts with traditional methods, 32 with the subject device. **Methods:**

   (a) Each cadaver will be given a number. For each testing group, we will randomly select four cadavers, omitting cadavers that have already been used.

   (b) We will construct four groups of two providers, one doctor and one medic in each. Each set of four providers (4 anesthesiologists and 4 paramedics) will be randomly assigned to one of four groups.

(c) We will do testing across two days, with four sessions. On each day will be a morning / afternoon session, with one group per session.

(d) Sequence of cadavers (clean vs dirty airway ordering) will be randomized for the group beforehand. Clean cadavers will be lightly suctioned prior to test initiation; soiled cadavers will have 300cc of artificial vomit added via the mouth, and a c-collar affixed. **Option:** Scenario based test for each cadaver, including a surgical scenario and a trauma scenario

(e) The following traditional tools will be made available: "Macintosh" and "Miller" direct laryngoscopy blades; Uescope video laryngoscope with 3 and 4 blade sizes; bougies and stylets; 7mm ID standard ETT.

(f) Providers will intubate each specimen with traditional methods first, followed by the subject device for all 4.

(g) Measured quantities: airway grade, time to intubate, number of devices used, number of attempts, likeart scale questionnaire.

Definitions:

i. **First-pass success:** The first pass starts upon entering the mouth with any airway device. The first pass ends with a removal of any device from the mouth before trying again, or with the exchange of devices (e.g. exchanging an ETT with stylet with a bougie)

ii. **Time to intubate:** The time to intubate will be defined as the time between first entering the airway, and the final forward motion of the ETT.

iii. **Airway grade:** We will use the Cormack-Lehane grading system for evaluating the airway

5.3 Discussion

While there is yet more work to be done, these initial results provide an exciting foundation upon which one future of these systems could and should build. All to often, the practice of medical device development seeks to produce incremental benefit to the expert provider at a steeper cost, ultimately only serving to increase the cost and limit the availability of care. Soft robotics offer a compelling alternative to this paradigm, wherein "smart" devices enable comparable performance at a fraction of the cost in non-expert hands.

If successful, this effort will create a model upon which future soft robotic medical devices may be built. In the case of airway management, this newfound capability of expert performance in novice hands may have the effect of saving innumerable lives, mitigating the rate of adverse events and complications, and reducing the cost burden of providing expert-level care in a broader range of environments. Such a paradigm may have similar effects in endovascular, pulmonological, and gastroenterological applications.

Chapter 6

Conclusion

6.1 Project impacts and future directions

On the timescales of human progress, soft robotics as a field is still in its infancy. As such, the whitespace that exists for novel applications is presently indeterminant, and consequently extraordinarily exciting. As a technologist, the opportunities ahead abound, and I will share some thoughts on how each of the preceding chapters have constructed my academic identity, as well as provide some ideas for future directions on each of the presented topics.

Chapter 2 Analytical Modeling: extracting design insights from closed-form solutions:

This project was important for setting the stage for the remainder of my Ph.D., and is to this day a very useful first-pass analysis tool when designing new vine robots. As the first effort to understand what design variables apply to the functional performance of vine robots, in many ways it is a roadmap to the initial design space of most of my ongoing projects. That said, a model is only as useful as its composition of utility and detail – that is, the order of magnitude of its detail often constrains the order of magnitude of its utility as a design tool. There is quite a bit more to be done on the physical modeling of soft and vine robots, which can likely unearth many additional insights.

Chapter 3 Design: applying modeling insights towards novel capabilities:

This work developed an additional design avenue for vine robot fabrication that switches the paradigm from fully soft to a hybrid design via the SRM – hopefully enabling the synthesis of the best of both worlds in robotics. In theory, this work can be extended to multiple different SRMs that individually control different axes of motion, and various lengths of vine robot tail. However, many of the design features represent design tradeoffs instead of design solutions. Hopefully, this effort unlocks future design directions, which might enable miniaturization and and extension in the total length of

the body that can be so controlled.

Chapter 4 Data-Driven Modeling, and Control: breakthrough performance of a soft robot arm:

This work showed that the Koopman formalism could be effectively applied well into the regime of non-linear dynamics, and while it took about 3 times as many years as I originally predicted, it certainly paid off in terms of its implications for soft robot modeling and control and its feature in *Science Robotics*. In many ways, I believe that the Koopman approach to modeling and control will prove to be a more data-efficient and performative method than traditional machine learning techniques. This little-known method could enable performance such that soft robots may one day be capable of performing useful tasks directly alongside humans. I believe that improvements in end effectors, and inclusion of length change, are the logical next steps for this project, and I am excited to see what comes next.

Chapter 5 Ongoing Projects: Semi-autonomous, Soft Robotic Airway Management:

This effort is getting very close to unlocking a currently unimaginable capability for EMS medical providers – delivering an endotracheal tube on the same order of success as a medical doctor in the hospital via vine-inspired airway management. Moreover, if successful, this current work will be the first soft robotic medical device (and will vindicate the title of *Veritasium's* viral YouTube video "This unstoppable robot could save your life"). While there is much yet to be done, this work is certainly a fitting culmination of my Ph.D. work – developing novel solutions to facilitate new capabilities in under-defined environments. I believe this work will be the foundation of soft robotics in medicine, and I hope to remain at the forefront of that development effort.

6.2 Final thoughts

The past 5 years of my life has been the most trying, defeating, embarrassing, inspiring, exciting, and gratifying chapter of my 31-year life thus far. Of course I see the contradiction of what I just said, as in many ways this has been an incredibly manic period of my life, characterized in no small part by terrible imposter syndrome and an unshakeable sense of inadequacy. However, from those depths, with the willingness to suspend my disbelief in my own capabilities, coupled with the support of my family, my friends, my labmates, and collaborators, I am concluding this chapter with nothing but assurance I took the absolutely necessary and appropriate step in my life to pursue the unknown.

My background does not readily admit graduate school as a tried-and-true path to achieving my career goals. Aside from some lawyers here and there, I am the only person in my family to pursue an advanced degree. In truth, at age 18, I thought I would be graduating business school with job prospects in real estate or consulting 4 years hence, just like my father did. Fast forward 13 years, and I am just emerging from nearly a decade worth of focus on a completely different set of topics. The only thing I can tell you about a pro forma at this point is that I don't really know how to make one.

However, I do now fully believe that regardless of the topic area, I have developed the fundamental capability to step into a world of unknowns and understand how the pieces fit together, whether it is machine learning, medical devices, or a pro forma. This is the lasting legacy of a graduate degree in the sciences that is hard effectively convey. In fact, I don't think that I would be adequately prepared for the world beyond grad school had I not viscerally experienced the terror of facing uncertainty, in a manner that truly tested my capabilities as a thinker and as a doer, for the years on end that characterize grad school. For that, I can't recommend a Ph.D. enough to those for whom such an

experience brings you a sense of wonder and intrigue instead of fear and contempt.

Today, I realize that everything breaks, and that the stability margin between advanced civilization and the stone age is leaner than we often realize. And yet, most importantly, I believe the future is bright, provided we all seek to expand that margin of stability through whatever means we have available. Cheers to all that are willing to join me on this mission.

Appendix A

Supplementary Materials

A.1 Supplementary Materials From Data-Driven Modeling, and Control: breakthrough performance of a soft robot arm

Testing Apparatus The experiments conducted in the framework of the study are performed on an experimental system shown in Fig. A.1.

A 1.8x1.8x1.5 m 80/20 frame was assembled to support the testing apparatus. To this frame the motion capture cameras, soft arm, and control hardware were affixed. Information about the position and shape of the manipulator is gathered via motion capture (PhaseSpace Inc. Impulse X2E). This investigation utilized the motion capture system with 8 detectors (cameras) and 4 sets of trackers evenly spaced along the backbone of the soft arm; four LEDs are attached along the axis of each muscle. The same motion capture system was used for both data collection used in offline model construction and for closed-loop position feedback in control experiments. In closed-loop experiments that are performed without predefined trajectory, additional four LED trackers are mounted on an external object (a pole), their coordinates are averaged in real-time in order to determine the central point, which then served as an arbitrary reference generator.

Festo VEAB-L-26-D2-Q4-V1-1R1 proportional pressure regulators with 0.01 to 2 bar output range and approximately 15 liters/min of flow at 1 bar pressure, are used to control the pressure in the arm's muscles. The body is held to a constant pressure of approximately 1.5 bar

The software used for running the system was LabVIEW 2019 with myRIO toolkit and real-time module, whereas LabVIEW Python node is used to acquire the real-time data from motion capture system. These information is then fed trough the fast network protocol to a myRIO 1900 control hardware. The same control hardware is also used to drive the pressure valves whereas an additional circuitry based on operational amplifiers is used to adjust 0-5V voltage levels generated by MyRIO hardware to be compatible with used proportional valves whose input range is 0-10V. Exhaust air ports of the valves are connected to vacuum so as to improve the dynamical response of the system.

Model Performance Metrics We perform a convergence study on the reconstruction power of our Koopman models as a function of the number of snapshots for a range of observables. This process allowed us to develop a dictionary of observables suitable for our system. Given a particular choice of observables and number of training samples, we build the corresponding linear input-output system with A, B, and C matrices. This linear model is applied to $N = 8000$ samples of sinusoidal verification data over a range of deflection amplitudes and speeds. These particular samples are not included in the training data in order to give us a fair evaluation of the predictive power of our models. The linear system produced via (4.24) and (4.15) evaluate the evolution of these initial conditions over a single time step. The single-step reconstruction error is given by

$$e_i = \frac{\|x_i^{+,\text{ predict}} - x_i^{+,\text{ actual}}\|_2}{L}. \tag{A.1}$$

where $x_i^{+,\text{ actual}}$ is the evolution of x_i measured by the motion capture system, $x_i^{+,\text{ predict}}$ is the evolution predicted by the DMD model, and L is the length of the soft arm. We use the root mean square (RMS) of the individual e_i errors to score our model:

$$e_{\text{RMS}} = 100\sqrt{\frac{1}{N}\sum_{i=1}^{N} e_i^2}. \tag{A.2}$$

Koopman Spectral Quantities We are often interested in the spectral properties of the Koopman operator because they give us physical information about the multiple coupled time-dependent processes inherent to our system. DMD can be used to approximate the discrete part of this spectrum [103]. We seek the triplet $(\lambda_i, \phi_i(z(x)), \mathbf{v}_i)$ of Koopman eigenvalues, eigenfunctions, and modes, respectively. The eigenvalues and Koopman modes are simply the eigenvalues and eigenvectors of the DMD matrix A. The Koopman modes in Fig. 4.8 are added to the time average mode associated with $\lambda = 1$ to give an

impression of the effect of the mode on the soft arm. Computation of the eigenfunctions requires $\mathbf{w}_i$ which are the eigenvectors of the conjugate transpose of A. After these are normalized so that $\langle \mathbf{v}_i, \mathbf{w}_j \rangle = \delta_{ij}$, the eigenfunctions are given by the complex inner product $\phi_i(z(x)) = \langle z(x), \mathbf{w}_i \rangle$. The eigenfunctions are shown here as functions of the lifted state $z(x)$. Their magnitude $|\phi_i(z(x))|$ is called the "mode power" and gives the relative importance of the i^{th} Koopman mode to the dynamics when the state is x. In order to compare the influences of the Koopman modes to the dynamics, their colorings in Fig. 4.8 are shown scaled to the maximum value of the mode power attained over the entire training data set.

Reconstruction of sinusoidally forced motion After choosing time delay observables, we attempted to reconstruct the movement of the soft arm under a sinusoidal inputs with six different frequencies ($0.1, 0.2, 0.4, 0.8, 1$, and 1.1Hz). We begin this process by providing a step input to the muscles that corresponds to a static position on the sinusoid with an arbitrary phase, and then complete two revolutions at a given frequency before incrementing up in speed. The position of the physical system was recorded via motion capture system, and these inputs were provided to our above-developed model. This process was repeated for low (similar to [82–84], approximately 15°), medium (similar to [104,105], approximately 25°), and high deflection (the single-actuator maximum of our system (robot 1), approximately 110°), with results reported in Fig. A.2.

Disturbance Rejection Finally, to evaluate the disturbance rejection capabilities of our system and to further distinguish the contribution of the static Koopman pregain, G, and the dynamic Koopman LQR gain, K, we commanded both stationary and circular references for the soft arm tip and subjected the system to disturbances. The control effort was recorded and compared to the control effort expected from the pregain term

alone. Given a static reference, the control effort from the pregain alone is constant in time. The results of the tests are shown in Fig. A.5, capturing the contribution of K, proportional to the disturbance.

Supplementary Figures

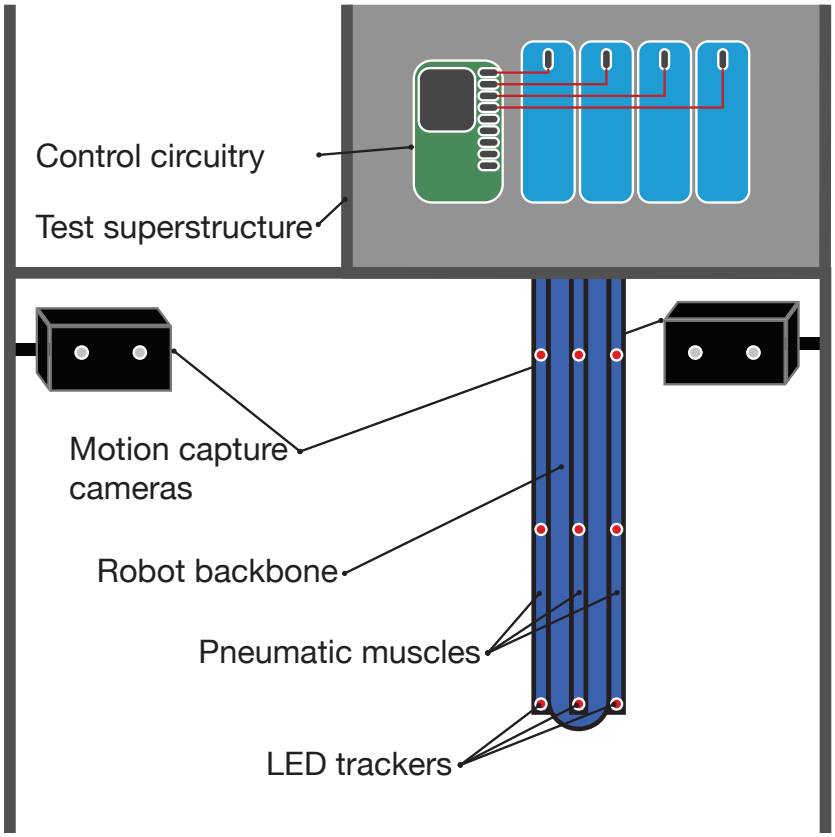

Figure A.1: **Schematic representation of the experimental setup and its components.** The soft arm is mounted from above to the test superstructure. The soft arm backbone provides stiffness and the pneumatic muscles generate movement. Four layers of LED trackers are tracked by motion capture cameras positions around the arm.

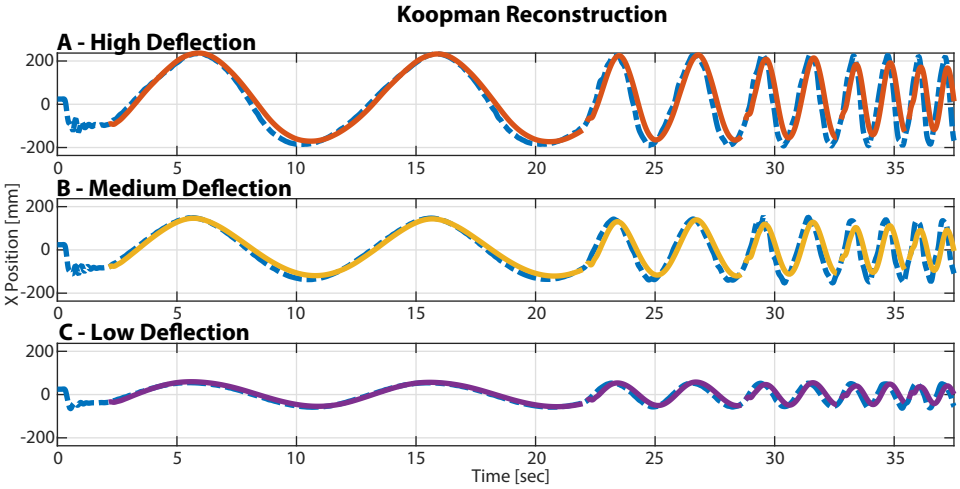

Figure A.2: **Koopman reconstruction of circular motion.** The dynamic Koopman model is given a collection of sinusoidal inputs with a range of amplitudes and speeds and is tasked with reconstructing the motion of the soft arm. The true trajectories are shown in dashed blue, and the high (**A**), medium (**B**), and low (**C**) deflection reconstructions are given in red, yellow, and purple, respectively. The reconstruction is restarted every time the frequency changes. The reconstruction agrees with the true frequency, but is missing some of the amplitude in the fast regime. The static Koopman operator and feedback control account for the improvement in performance between this plot and Fig. 4.9

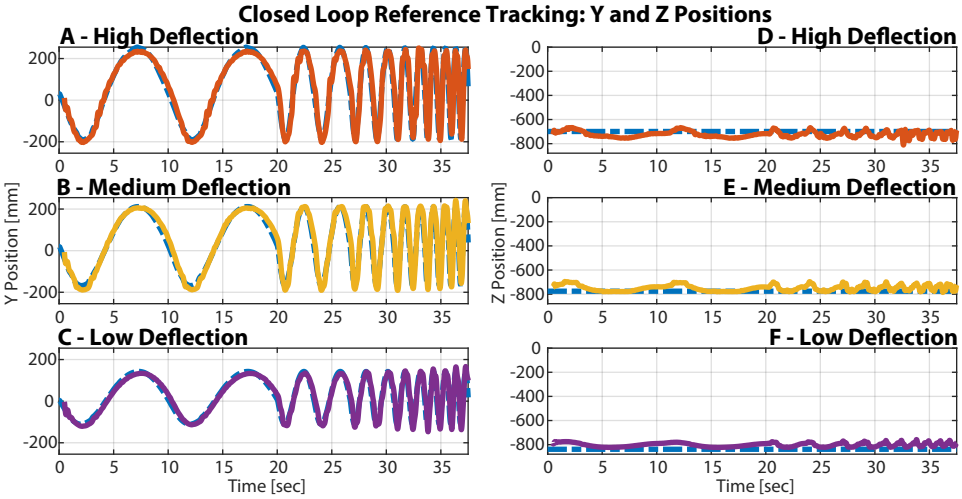

Figure A.3: **Y and Z components of the real-time closed-loop reference tracking experiments**. The soft arm tracked circular reference trajectories in the X-Y plane with frequencies ranging from 0.1 to 1.1 Hz (0.2Hz step) at: (**A**,**D**) high, (**B**,**E**) medium, and (**C**,**F**) low deflection magnitudes. Plots show the Y (left column) and Z (right column) positions over time compared to their respective references. The commanded references are dashed lines and the control results are solid lines.

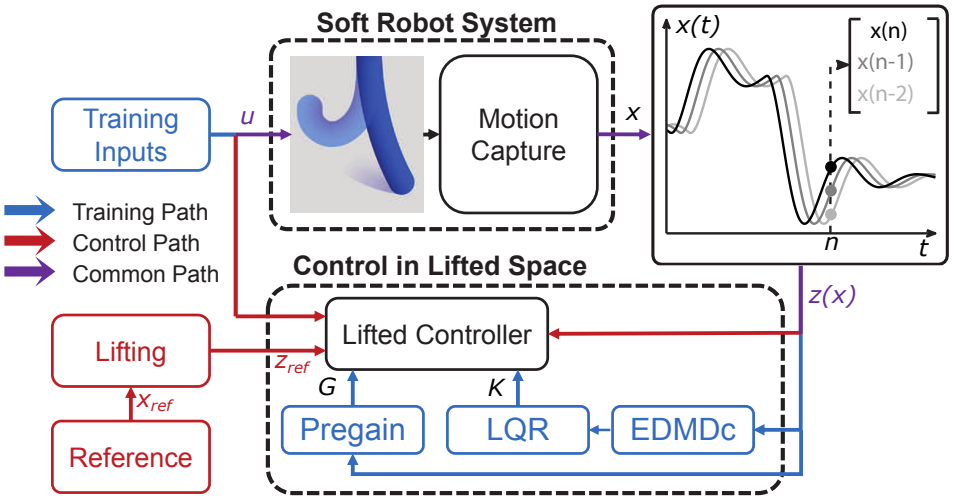

Figure A.4: **Block diagram of the system, training method and K-LQR control approach.** Training inputs representing voltage signals are fed into pressure valves and 3D positions of the soft arm are measured by using a motion capture system. The lifting procedure of the position data provides the inputs needed to determine the Koopman model of the system and to calculate optimal lifted controller parameters. The position of the soft arm is finally controlled in 3D space by using obtained K-LQR.

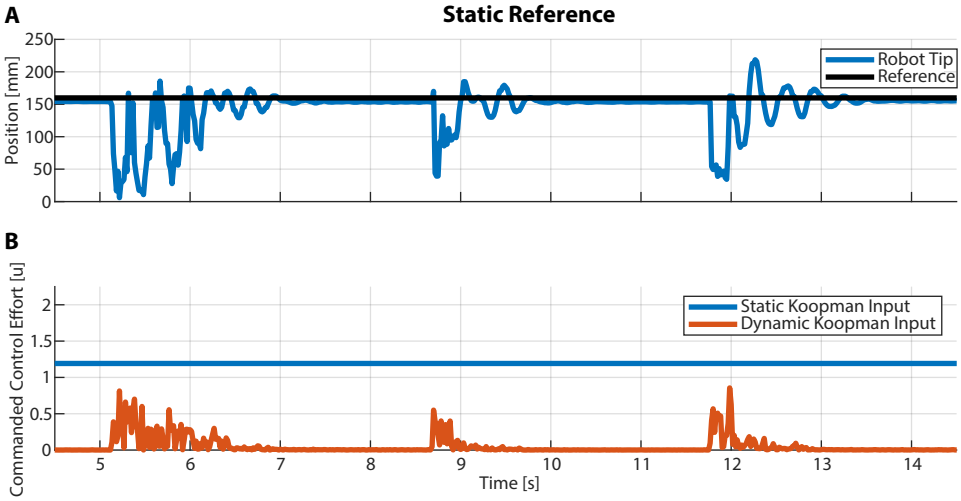

Figure A.5: **Demonstration of our controller's ability to reject impulse disturbances in real-time. A)** The position over time of the end effector is shown relative to a predefined reference. The soft arm returns to the reference position after three large disturbances are applied. **B)** The magnitude of the commanded control effort is shown. Note that the static Koopman input component comes from the pregain term and is constant because the static reference doesn't change. The dynamic Koopman input adapts in real time to the disturbances.

Supplementary Movies All Supplementary Movies can be found at the following URL: `https://doi.org/10.5281/zenodo.8184777`.

Movie S1: Movie S1 shows the performance of Robot 1 commanded to follow an arbitrary trajectory throughout the workspace, ranging from low to high deflection.

Movie S2: Movie S2 shows the performance of Robot 1 commanded to follow a series of sinusoidal trajectories at increasing speeds ($0.1-1.1$Hz frequency) and increasing deflections, as shown in Figures 4.9 and A.3.

Movie S3: Movie S3 shows our system completing two real-world tasks: first, catching a swinging ball that enters the workspace from two different directions; second, throwing a ball into a bin positioned at two different locations in the workspace.

Movie S4: Movie S4 shows our training, modeling, and control sequence for Robot 1. This sequence uses 5 minutes of step inputs, approximately 3 seconds of model and controller computation, followed by arbitrary reference tracking.

Movie S5: Movie S5 shows our training, modeling, and control sequence for Robot 2. The same sequence is provided as in Movie S4, but with a robot capable of nearly 180° of deflection. Arbitrary reference tracking is successful across the entire range of deflections.

Bibliography

[1] I. Ermolov, *Industrial Robotics Review*, pp. 195–204. Springer International Publishing, Cham, 2020.

[2] W. Ji and L. Wang, *Industrial robotic machining: a review*, *The International Journal of Advanced Manufacturing Technology* **103** (2019) 1239–1255.

[3] A. S. Bisen and H. Payal, *Collaborative robots for industrial tasks: A review*, *Materials Today: Proceedings* **52** (2022) 500–504. International Conference on Smart and Sustainable Developments in Materials, Manufacturing and Energy Engineering.

[4] S. Bragança, E. Costa, I. Castellucci, and P. M. Arezes, *A Brief Overview of the Use of Collaborative Robots in Industry 4.0: Human Role and Safety*, pp. 641–650. Springer International Publishing, Cham, 2019.

[5] D. Kragic, J. Gustafson, H. Karaoguz, P. Jensfelt, and R. Krug, *Interactive, collaborative robots: Challenges and opportunities.*, in *IJCAI*, pp. 18–25, 2018.

[6] F. Vicentini, *Collaborative robotics: a survey*, *Journal of Mechanical Design* **143** (2021), no. 4.

[7] D. Kim, S.-H. Kim, T. Kim, B. B. Kang, M. Lee, W. Park, S. Ku, D. Kim, J. Kwon, H. Lee, *et. al.*, *Review of machine learning methods in soft robotics*, *Plos one* **16** (2021), no. 2 e0246102.

[8] D. Rus and M. T. Tolley, *Design, fabrication and control of soft robots*, *Nature* **521** (2015), no. 7553 467–475.

[9] C. Majidi, *Soft robotics: a perspective—current trends and prospects for the future*, *Soft robotics* **1** (2014), no. 1 5–11.

[10] T. George Thuruthel, Y. Ansari, E. Falotico, and C. Laschi, *Control strategies for soft robotic manipulators: A survey*, *Soft robotics* **5** (2018), no. 2 149–163.

[11] E. W. Hawkes, C. Majidi, and M. T. Tolley, *Hard questions for soft robotics*, *Science robotics* **6** (2021), no. 53 eabg6049.

[12] J. Wang and A. Chortos, *Control strategies for soft robot systems*, *Advanced Intelligent Systems* **4** (2022), no. 5 2100165.

[13] L. Shi, Z. Liu, and K. Karydis, *Koopman operators for modeling and control of soft robotics*, *arXiv preprint arXiv:2301.09708v1* (2023).

[14] O. Yasa, Y. Toshimitsu, M. Y. Michelis, L. S. Jones, M. Filippi, T. Buchner, and R. K. Katzschmann, *An overview of soft robotics*, *Annual Review of Control, Robotics, and Autonomous Systems* **6** (2022).

[15] S. Kim, C. Laschi, and B. Trimmer, *Soft robotics: a bioinspired evolution in robotics*, *Trends in biotechnology* **31** (2013), no. 5 287–294.

[16] C. Laschi, B. Mazzolai, V. Mattoli, M. Cianchetti, and P. Dario, *Design of a biomimetic robotic octopus arm*, *Bioinspiration & biomimetics* **4** (2009), no. 1 015006.

[17] F. Ilievski, A. D. Mazzeo, R. F. Shepherd, X. Chen, and G. M. Whitesides, *Soft robotics for chemists*, *Angewandte Chemie* **123** (2011), no. 8 1930–1935.

[18] S. Kim, E. Hawkes, K. Choy, M. Joldaz, J. Foleyz, and R. Wood, *Micro artificial muscle fiber using niti spring for soft robotics*, in *2009 IEEE/RSJ International Conference on Intelligent Robots and Systems*, pp. 2228–2234, IEEE, 2009.

[19] R. F. Shepherd, F. Ilievski, W. Choi, S. A. Morin, A. A. Stokes, A. D. Mazzeo, X. Chen, M. Wang, and G. M. Whitesides, *Multigait soft robot*, *Proceedings of the national academy of sciences* **108** (2011), no. 51 20400–20403.

[20] E. Brown, N. Rodenberg, J. Amend, A. Mozeika, E. Steltz, M. R. Zakin, H. Lipson, and H. M. Jaeger, *Universal robotic gripper based on the jamming of granular material*, *Proceedings of the National Academy of Sciences* **107** (2010), no. 44 18809–18814.

[21] B. Post, *More help for polio victims*, 1958. Published by *Newsweek*.

[22] B. Roth, J. Rastegar, and V. Scheinman, *On the design of computer controlled manipulators, first cism-ift0mm symp. on theory and practice of robots and manipulators, vol. 1*, 1974.

[23] J. F. Wilson and N. Inou, *Bellows-type springs for robotics*, in *Proc. Adv. Spring Technol. JSSE 60th Anniversary Int. Symp*, pp. 109–119, 2007.

[24] K. Suzumori, S. Iikura, and H. Tanaka, *Applying a flexible microactuator to robotic mechanisms*, *IEEE Control systems magazine* **12** (1992), no. 1 21–27.

[25] D. Mishima, T. Aoki, and S. Hirose, *Development of pneumatically controlled expandable arm for search in the environment with tight access*, in *Field and Service Robotics*, pp. 509–518, Springer, 2003.

[26] E. W. Hawkes, L. H. Blumenschein, J. D. Greer, and A. M. Okamura, *A soft robot that navigates its environment through growth*, *Science Robotics* **2** (2017), no. 8 eaan3028.

[27] W. McMahan, V. Chitrakaran, M. Csencsits, D. Dawson, I. D. Walker, B. A. Jones, M. Pritts, D. Dienno, M. Grissom, and C. D. Rahn, *Field trials and testing of the octarm continuum manipulator*, in *Proceedings 2006 IEEE International Conference on Robotics and Automation, 2006. ICRA 2006.*, pp. 2336–2341, IEEE, 2006.

[28] B. A. Jones and I. D. Walker, *Kinematics for multisection continuum robots*, *IEEE Transactions on Robotics* **22** (2006), no. 1 43–55.

[29] I. D. Walker, D. M. Dawson, T. Flash, F. W. Grasso, R. T. Hanlon, B. Hochner, W. M. Kier, C. C. Pagano, C. D. Rahn, and Q. M. Zhang, *Continuum robot arms inspired by cephalopods*, in *Unmanned Ground Vehicle Technology VII*, vol. 5804, pp. 303–314, SPIE, 2005.

[30] R. M. Alexander, *Principles of Animal Locomotion*. Princeton University Press, 2003.

[31] A. Goriely, *The mathematics and mechanics of biological growth*, vol. 45. Springer, 2017.

[32] M. W. Steer and J. M. Steer, *Pollen tube tip growth*, *The New Phytologist* **111** (1989), no. 3 323–358.

[33] R. R. Lew, *How does a hypha grow? the biophysics of pressurized growth in fungi*, *Nature Reviews Microbiology* **9** (2011), no. 7 509–518.

[34] D. Weigel and G. Jürgens, *Stem cells that make stems*, *Nature* **415** (2002), no. 6873 751–754.

[35] E. Zuckerkandl, *Coelomic pressures in sipunculus nudus*, *The Biological bulletin* **98** (1950), no. 2 161–173.

[36] R. Gibson, *A new genus and species of lineid heteronemertean from South Africa, polybrachiorhynchus dayi (nemertea: Anopla), possessing a multibranched proboscis*, *Bulletin of Marine Science* **27** (1977), no. 3 552–571.

[37] S. Li and G. Hao, *Current trends and prospects in compliant continuum robots: A survey*, in *Actuators*, vol. 10, p. 145, MDPI, 2021.

[38] C. Laschi, B. Mazzolai, and M. Cianchetti, *Soft robotics: Technologies and systems pushing the boundaries of robot abilities*, *Sci. Robot.* **1** (2016), no. 1 eaah3690.

[39] N. D. Naclerio and E. W. Hawkes, *Simple, low-hysteresis, foldable, fabric pneumatic artificial muscle*, *IEEE Robotics and Automation Letters* **5** (2020), no. 2 3406–3413.

[40] L. H. Blumenschein, N. S. Usevitch, B. H. Do, E. W. Hawkes, and A. M. Okamura, *Helical actuation on a soft inflated robot body*, in *2018 IEEE International Conference on Soft Robotics (RoboSoft)*, pp. 245–252, IEEE, 2018.

[41] L. H. Blumenschein, M. M. Coad, D. A. Haggerty, A. M. Okamura, and E. W. Hawkes, *Design, modeling, control, and application of everting vine robots*, *Frontiers in Robotics and AI* **7** (2020) 548266. Licensed from Frontiers under CC-BY 4.0. Reprinted, with permission.

[42] D. A. Haggerty, N. D. Naclerio, and E. W. Hawkes, *Characterizing environmental interactions for soft growing robots*, in *2019 IEEE/RSJ International Conference on Intelligent Robots and Systems (IROS)*, pp. 3335–3342, IEEE, 2019. ©2020 IEEE. Reprinted, with permission.

[43] D. A. Haggerty, N. D. Naclerio, and E. W. Hawkes, *Hybrid vine robot with internal steering-reeling mechanism enhances system-level capabilities*, *IEEE Robotics and Automation Letters* **6** (2021), no. 3 5437–5444. ©2020 IEEE. Reprinted, with permission.

[44] D. A. Haggerty, M. J. Banks, E. Kamenar, A. B. Cao, P. C. Curtis, I. Mezić, and E. W. Hawkes, *Control of soft robots with inertial dynamics*, *Science Robotics* **8** (2023), no. 81.

[45] D. A. Haggerty, M. J. Banks, P. C. Curtis, I. Mezić, and E. W. Hawkes, *Modeling, reduction, and control of a helically actuated inertial soft robotic arm via the koopman operator*, *arXiv preprint arXiv:2011.07939* (2020).

[46] J. D. Greer, L. H. Blumenschein, A. M. Okamura, and E. W. Hawkes, *Obstacle-aided navigation of a soft growing robot*, in *2018 IEEE International Conference on Robotics and Automation (ICRA)*, pp. 1–8, IEEE, 2018.

[47] L. H. Blumenschein, A. M. Okamura, and E. W. Hawkes, *Modeling of bioinspired apical extension in a soft robot*, in *Conference on Biomimetic and Biohybrid Systems*, pp. 522–531, Springer, 2017.

[48] D. Trivedi, C. D. Rahn, W. M. Kier, and I. D. Walker, *Soft robotics: Biological inspiration, state of the art, and future research*, *Applied bionics and biomechanics* **5** (2008), no. 3 99–117.

[49] T. Viebach, F. Pauker, G. Buchmann, G. Weiglhofer, and R. Pauker, *Everting sleeve system*, July 5, 2006. European Patent 1676598A2.

[50] H. Tsukagoshi, N. Arai, I. Kiryu, and A. Kitagawa, *Smooth creeping actuator by tip growth movement aiming for search and rescue operation*, in *2011 IEEE International Conference on Robotics and Automation*, pp. 1720–1725, IEEE, 2011.

[51] H. Tsukagoshi, N. Arai, I. Kiryu, and A. Kitagawa, *Tip growing actuator with the hose-like structure aiming for inspection on narrow terrain*, *IJAT* **5** (2011), no. 4 516–522.

[52] A. Sadeghi, A. Tonazzini, L. Popova, and B. Mazzolai, *Robotic mechanism for soil penetration inspired by plant root*, in *2013 IEEE International Conference on Robotics and Automation*, pp. 3457–3462, IEEE, 2013.

[53] M. C. Yip and D. B. Camarillo, *Model-less feedback control of continuum manipulators in constrained environments*, *IEEE Transactions on Robotics* **30** (2014), no. 4 880–889.

[54] M. Mahvash and P. E. Dupont, *Stiffness control of a continuum manipulator in contact with a soft environment*, in *2010 IEEE/RSJ International Conference on Intelligent Robots and Systems*, pp. 863–870, IEEE, 2010.

[55] R. J. Webster III and B. A. Jones, *Design and kinematic modeling of constant curvature continuum robots: A review*, *The International Journal of Robotics Research* **29** (2010), no. 13 1661–1683.

[56] P. Slade, A. Gruebele, Z. Hammond, M. Raitor, A. M. Okamura, and E. W. Hawkes, *Design of a soft catheter for low-force and constrained surgery*, in *2017 IEEE/RSJ International Conference on Intelligent Robots and Systems (IROS)*, pp. 174–180, IEEE, 2017.

[57] M. M. Coad, L. H. Blumenschein, S. Cutler, J. A. R. Zepeda, N. D. Naclerio, H. El-Hussieny, U. Mehmood, J. Ryu, E. W. Hawkes, and A. M. Okamura, *Vine robots: Design, teleoperation, and deployment for navigation and exploration*, .

[58] N. D. Naclerio, C. Hubicki, Y. Aydin, D. Goldman, and E. Hawkes, *Soft robotic burrowing device with tip-extension and granular fluidization*, in *2018 IEEE International Conference on Intelligent Robots and Systems (IROS)*, pp. 5918–5923, IEEE, 2018.

[59] Z. M. Hammond, N. S. Usevitch, E. W. Hawkes, and S. Follmer, *Pneumatic reel actuator: Design, modeling, and implementation*, in *Robotics and Automation (ICRA), 2017 IEEE International Conference on*, pp. 626–633, IEEE, 2017.

[60] R. Comer and S. Levy, *Deflections of an inflated circular-cylindrical cantilever beam*, *AIAA journal* **1** (1963), no. 7 1652–1655.

[61] R. W. Leonard, G. W. Brooks, and H. G. McComb Jr, *Structural considerations of inflatable reentry vehicles*, .

[62] W. Fichter, *A theory for inflated thin-wall cylindrical beams*, .

[63] "Overview of materials for low density polyethylene LDPE, blow molding grade."

[64] N. Ladizesky and I. Ward, *Determination of poisson's ratio and young's modulus of low-density polyethylene*, *Journal of Macromolecular Science, Part B: Physics* **5** (1971), no. 4 661–692.

[65] J. Page and J. Wang, *Prediction of shear force and an analysis of yarn slippage for a plain-weave carbon fabric in a bias extension state*, *Composites Science and Technology* **60** (2000), no. 7 977–986.

[66] W. E. Heap, N. D. Naclerio, M. M. Coad, S.-G. Jeong, and E. W. Hawkes, *Soft retraction device and internal camera mount for everting vine robots*, in *2021 IEEE/RSJ International Conference on Intelligent Robots and Systems (IROS)*, pp. 4982–4988, IEEE, 2021.

[67] S. Wang, R. Zhang, D. A. Haggerty, N. D. Naclerio, and E. W. Hawkes, *A dexterous tip-extending robot with variable-length shape-locking*, in *2020 IEEE International Conference on Robotics and Automation (ICRA)*, pp. 9035–9041, IEEE, 2020. ©2020 IEEE. Reprinted, with permission.

[68] M. M. Coad, R. P. Thomasson, L. H. Blumenschein, N. S. Usevitch, E. W. Hawkes, and A. M. Okamura, *Retraction of soft growing robots without buckling*, *IEEE Robotics and Automation Letters* **5** (2020), no. 2 2115–2122.

[69] T. Yoshida, K. Nagatani, S. Tadokoro, T. Nishimura, and E. Koyanagi, *Improvements to the rescue robot quince toward future indoor surveillance missions in the fukushima daiichi nuclear power plant*, in *Field and service robotics*, pp. 19–32, Springer, 2014.

[70] H. Godaba, F. Putzu, T. Abrar, J. Konstantinova, and K. Althoefer, *Payload capabilities and operational limits of eversion robots*, in *Annual Conference Towards Autonomous Robotic Systems*, pp. 383–394, Springer, 2019.

[71] L. H. Blumenschein, L. T. Gan, J. A. Fan, A. M. Okamura, and E. W. Hawkes, *A tip-extending soft robot enables reconfigurable and deployable antennas*, *IEEE Robotics and Automation Letters* **3** (2018), no. 2 949–956.

[72] B. H. Do, V. Banashek, and A. M. Okamura, *Dynamically reconfigurable discrete distributed stiffness for inflated beam robots*, in *2020 IEEE International Conference on Robotics and Automation (ICRA)*, pp. 9050–9056, IEEE, 2020.

[73] M. Selvaggio, L. Ramirez, N. Naclerio, B. Siciliano, and E. Hawkes, *An obstacle-interaction planning method for navigation of actuated vine robots*, in *2020 IEEE International Conference on Robotics and Automation (ICRA)*, pp. 3227–3233, IEEE, 2020.

[74] J. D. Greer, T. K. Morimoto, A. M. Okamura, and E. W. Hawkes, *A soft, steerable continuum robot that grows via tip extension*, *Soft robotics* (2018).

[75] Y. Satake, A. Takanishi, and H. Ishii, *Novel growing robot with inflatable structure and heat-welding rotation mechanism*, *IEEE/ASME Transactions on Mechatronics* **25** (2020), no. 4 1869–1877.

[76] A. Ataka, T. Abrar, F. Putzu, H. Godaba, and K. Althoefer, *Model-based pose control of inflatable eversion robot with variable stiffness*, *IEEE Robotics and Automation Letters* **5** (2020), no. 2 3398–3405.

[77] R. Williams and B. H. Shelley, *Inverse kinematics for planar parallel manipulators*, in *Proceedings of ASME Design Technical Conferences*, pp. 14–17, 1997.

[78] S.-G. Jeong, M. M. Coad, L. H. Blumenschein, M. Luo, U. Mehmood, J. H. Kim, A. M. Okamura, and J.-H. Ryu, *A tip mount for transporting sensors and tools using soft growing robots*, in *2020 IEEE/RSJ International Conference on Intelligent Robots and Systems (IROS)*, pp. 8781–8788, 2020.

[79] R. Jitosho, N. Agharese, A. Okamura, and Z. Manchester, *A dynamics simulator for soft growing robots*, in *2021 IEEE International Conference on Robotics and Automation (ICRA)*, pp. 11775–11781, IEEE, 2021.

[80] I. Mezić, *Spectral properties of dynamical systems, model reduction and decompositions*, *Nonlinear Dynamics* **41** (2005) 309–325.

[81] M. Budišić, R. Mohr, and I. Mezić, *Applied koopmanism*, *Chaos: An Interdisciplinary Journal of Nonlinear Science* **22** (2012), no. 4 047510.

[82] D. Bruder, X. Fu, G. Brent, D. Remy, and R. Vasudevan, *Data-driven control of soft robots using koopman operator theory*, *IEEE Transactions on Robotics* **37** (2021), no. 3 948–961.

[83] D. Bruder, B. Gillespie, C. D. Remy, and R. Vasudevan, *Modeling and control of soft robots using the koopman operator and model predictive control*, *arXiv preprint arXiv:1902.02827* (2019).

[84] D. Bruder, C. D. Remy, and R. Vasudevan, *Nonlinear system identification of soft robot dynamics using koopman operator theory*, in *2019 International Conference on Robotics and Automation (ICRA)*, pp. 6244–6250, IEEE, 2019.

[85] D. Bruder, X. Fu, R. B. Gillespie, C. D. Remy, and R. Vasudevan, *Koopman-based control of a soft continuum manipulator under variable loading conditions*, *arXiv preprint arXiv:2002.01407* (2020).

[86] I. Mezić, *Koopman operator, geometry, and learning of dynamical systems*, *Notices of the American Mathematical Society* **68** (2021), no. 7 1087–1105.

[87] T. G. Thuruthel, E. Falotico, F. Renda, and C. Laschi, *Model-based reinforcement learning for closed-loop dynamic control of soft robotic manipulators*, *IEEE Transactions on Robotics* **35** (2019), no. 1 124–134.

[88] M. W. Hannan and I. D. Walker, *Kinematics and the implementation of an elephant's trunk manipulator and other continuum style robots*, *Journal of robotic systems* **20** (2003), no. 2 45–63.

[89] D. Trivedi, A. Lotfi, and C. D. Rahn, *Geometrically exact models for soft robotic manipulators*, *IEEE Transactions on Robotics* **24** (2008), no. 4 773–780.

[90] B. A. Jones and I. D. Walker, *Practical kinematics for real-time implementation of continuum robots*, *IEEE Transactions on Robotics* **22** (2006), no. 6 1087–1099.

[91] V. Falkenhahn, A. Hildebrandt, R. Neumann, and O. Sawodny, *Model-based feedforward position control of constant curvature continuum robots using feedback linearization*, in *2015 IEEE International Conference on Robotics and Automation (ICRA)*, pp. 762–767, IEEE, 2015.

[92] A. D. Kapadia, I. D. Walker, D. M. Dawson, and E. Tatlicioglu, *A model-based sliding mode controller for extensible continuum robots*, in *Proceedings of the 9th WSEAS international conference on Signal processing, robotics and automation*, pp. 113–120, 2010.

[93] A. D. Marchese, R. Tedrake, and D. Rus, *Dynamics and trajectory optimization for a soft spatial fluidic elastomer manipulator*, *The International Journal of Robotics Research* **35** (2016), no. 8 1000–1019.

[94] Y. Engel, P. Szabo, and D. Volkinshtein, *Learning to control an octopus arm with gaussian process temporal difference methods*, in *Advances in neural information processing systems*, pp. 347–354, 2006.

[95] D. Braganza, D. M. Dawson, I. D. Walker, and N. Nath, *A neural network controller for continuum robots*, *IEEE transactions on robotics* **23** (2007), no. 6 1270–1277.

[96] T. G. Thuruthel, E. Falotico, F. Renda, and C. Laschi, *Learning dynamic models for open loop predictive control of soft robotic manipulators*, *Bioinspiration & biomimetics* **12** (2017), no. 6 066003.

[97] C. Della Santina, R. L. Truby, and D. Rus, *Data–driven disturbance observers for estimating external forces on soft robots*, *IEEE Robotics and Automation Letters* **5** (2020), no. 4 5717–5724.

[98] C. Della Santina, R. K. Katzschmann, A. Bicchi, and D. Rus, *Model-based dynamic feedback control of a planar soft robot: Trajectory tracking and interaction with the environment*, *The International Journal of Robotics Research* **39** (2020), no. 4 490–513.

[99] B. O. Koopman, *Hamiltonian systems and transformation in hilbert space*, *Proceedings of the National Academy of Sciences* **17** (may, 1931) 315–318.

[100] H. Arbabi and I. Mezic, *Ergodic theory, dynamic mode decomposition, and computation of spectral properties of the koopman operator*, *SIAM Journal on Applied Dynamical Systems* **16** (2017), no. 4 2096–2126.

[101] M. Korda and I. Mezić, *Linear predictors for nonlinear dynamical systems: Koopman operator meets model predictive control*, *Automatica* **93** (jul, 2018) 149–160.

[102] H. Arbabi and I. Mezic, *Computation of transient koopman spectrum using hankel-dynamic mode decompoisition*, *APS* (2017) G1–009.

[103] M. Korda and I. Mezić, *On convergence of extended dynamic mode decomposition to the koopman operator*, *Journal of Nonlinear Science* **28** (nov, 2017) 687–710.

[104] R. K. Katzschmann, C. Della Santina, Y. Toshimitsu, A. Bicchi, and D. Rus, *Dynamic motion control of multi-segment soft robots using piecewise constant curvature matched with an augmented rigid body model*, in *2019 2nd IEEE International Conference on Soft Robotics (RoboSoft)*, pp. 454–461, IEEE, 2019.

[105] R. K. Katzschmann, M. Thieffry, O. Goury, A. Kruszewski, T.-M. Guerra, C. Duriez, and D. Rus, *Dynamically closed-loop controlled soft robotic arm using a reduced order finite element model with state observer*, in *2019 2nd IEEE International Conference on Soft Robotics (RoboSoft)*, pp. 717–724, IEEE, 2019.

[106] A. Centurelli, L. Arleo, A. Rizzo, S. Tolu, C. Laschi, and E. Falotico, *Closed-loop dynamic control of a soft manipulator using deep reinforcement learning*, *IEEE Robotics and Automation Letters* **7** (2022), no. 2 4741–4748.

[107] X. Wang and N. Rojas, *A data-efficient model-based learning framework for the closed-loop control of continuum robots*, 2022.

[108] T. G. Thuruthel, B. Shih, C. Laschi, and M. T. Tolley, *Soft robot perception using embedded soft sensors and recurrent neural networks*, *Science Robotics* **4** (2019), no. 26.

[109] R. L. Truby, C. Della Santina, and D. Rus, *Distributed proprioception of 3d configuration in soft, sensorized robots via deep learning*, *IEEE Robotics and Automation Letters* **5** (2020), no. 2 3299–3306.

[110] S. Neppalli, B. Jones, W. McMahan, V. Chitrakaran, I. Walker, M. Pritts, M. Csencsits, C. Rahn, and M. Grissom, *Octarm - a soft robotic manipulator*, in *IEEE/RSJ International Conference on Intelligent Robots and Systems*, IEEE, 2007.

[111] D. Braganza, D. M. Dawson, I. D. Walker, and N. Nath, *A neural network controller for continuum robots*, *IEEE Transactions on Robotics* (2007).

[112] I. Mezić and A. Banaszuk, *Comparison of systems with complex behavior*, *Physica D: Nonlinear Phenomena* **197** (2004), no. 1-2 101–133.

[113] J. L. Proctor, S. L. Brunton, and J. N. Kutz, *Dynamic mode decomposition with control*, *SIAM Journal on Applied Dynamical Systems* **15** (2016), no. 1 142–161, [https://doi.org/10.1137/15M1013857].

[114] J. L. Proctor, S. L. Brunton, and J. N. Kutz, *Generalizing koopman theory to allow for inputs and control*, *SIAM Journal on Applied Dynamical Systems* **17** (2018), no. 1 909–930.

[115] L. Shi and K. Karydis, *Acd-edmd: Analytical construction for dictionaries of lifting functions in koopman operator-based nonlinear robotic systems*, *IEEE Robotics and Automation Letters* **7** (2021), no. 2 906–913.

[116] J. Chen, Y. Dang, and J. Han, *Offset-free model predictive control of a soft manipulator using the koopman operator*, *Mechatronics* **86** (oct, 2022) 102871.

[117] H. Yin, M. Welle, and D. Kragic, *Policy learning with embedded koopman optimal control .*, *Proceedings of Machine Learning Research* **144** (2018).

[118] I. Abraham and T. D. Murphey, *Active learning of dynamics for data-driven control using koopman operators*, *IEEE Transactions on Robotics* **35** (2019), no. 5 1071–1083.

[119] A. Gibson, *Application of koopman linear quadratic regulator to the control of a spherical microbubble*, Master's thesis, University of Colorado Colorado Springs, 2022.

[120] G. Mamakoukas, M. L. Castano, X. Tan, and T. D. Murphey, *Derivative-based koopman operators for real-time control of robotic systems*, *IEEE Transactions on Robotics* **37** (2021), no. 6 2173–2192.

[121] A. Kazemipour, O. Fischer, Y. Toshimitsu, K. W. Wong, and R. K. Katzschmann, *A robust adaptive approach to dynamic control of soft continuum manipulators*, *arXiv preprint arXiv:2109.11388* (2021).

[122] I. Mezić, *On numerical approximations of the koopman operator*, *Mathematics* **10** (2022), no. 7 1180.

[123] B. D. Anderson and J. B. Moore, *Optimal control: linear quadratic methods*. Courier Corporation, 2007.

[124] Y. Huang, M. Hofer, and R. D'Andrea, *Offset-free model predictive control: A ball catching application with a spherical soft robotic arm*, in *2021 International Conference on Intelligent Robots and Systems (IROS)*, pp. 563–570, IEEE/RSJ, 2021.

[125] M. M. Coad, L. H. Blumenschein, S. Cutler, J. A. R. Zepeda, N. D. Naclerio, H. El-Hussieny, U. Mehmood, J.-H. Ryu, E. W. Hawkes, and A. M. Okamura, *Vine robots: Design, teleoperation, and deployment for navigation and exploration*, *IEEE Robotics & Automation Magazine* **27** (2019), no. 3 120–132.

[126] M. R. Van Scott, J. Chandler, S. Olmstead, J. M. Brown, and M. Mannie, *Airway anatomy, physiology, and inflammation*, *The toxicant induction of irritant asthma, rhinitis, and related conditions* (2013) 19–61.

[127] J.-A. Song, H.-B. Bae, J.-I. Choi, J. Kang, and S. Jeong, *Difficult intubation and anesthetic management in an adult patient with undiagnosed congenital tracheal stenosis: a case report*, *Journal of International Medical Research* **48** (2020), no. 4 0300060520911267.

[128] N. Dohrn, T. Sommer, J. Bisgaard, E. Rønholm, and J. F. Larsen, *Difficult tracheal intubation in obese gastric bypass patients*, *Obesity surgery* **26** (2016), no. 11 2640–2647.

[129] K. Karamchandani, J. Wheelwright, A. L. Yang, N. D. Westphal, A. K. Khanna, and S. N. Myatra, *Emergency airway management outside the operating room: current evidence and management strategies*, *Anesthesia & Analgesia* **133** (2021), no. 3 648–662.

[130] H. E. Wang, R. H. Schmicker, M. R. Daya, S. W. Stephens, A. H. Idris, J. N. Carlson, M. R. Colella, H. Herren, M. Hansen, N. J. Richmond, *et. al.*, *Effect of a strategy of initial laryngeal tube insertion vs endotracheal intubation on 72-hour*

survival in adults with out-of-hospital cardiac arrest: a randomized clinical trial, *Jama* **320** (2018), no. 8 769–778.

[131] J. M. Mosier, J. C. Sakles, J. A. Law, C. A. Brown III, and P. G. Brindley, *Tracheal intubation in the critically ill. where we came from and where we should go*, *American journal of respiratory and critical care medicine* **201** (2020), no. 7 775–788.

[132] B. Guihard, C. Chollet-Xémard, P. Lakhnati, B. Vivien, C. Broche, D. Savary, A. Ricard-Hibon, P.-J. M. dit Cassou, F. Adnet, E. Wiel, *et. al.*, *Effect of rocuronium vs succinylcholine on endotracheal intubation success rate among patients undergoing out-of-hospital rapid sequence intubation: a randomized clinical trial*, *Jama* **322** (2019), no. 23 2303–2312.

[133] V. Russotto, S. N. Myatra, J. G. Laffey, E. Tassistro, L. Antolini, P. Bauer, J. B. Lascarrou, K. Szułdrzyński, L. Camporota, P. Pelosi, *et. al.*, *Intubation practices and adverse peri-intubation events in critically ill patients from 29 countries*, *Jama* **325** (2021), no. 12 1164–1172.

[134] J. C. Sakles, S. Chiu, J. Mosier, C. Walker, and U. Stolz, *The importance of first pass success when performing orotracheal intubation in the emergency department*, *Academic Emergency Medicine* **20** (2013), no. 1 71–78.

[135] A. M. Joffe, M. F. Aziz, K. L. Posner, L. V. Duggan, S. L. Mincer, and K. B. Domino, *Management of difficult tracheal intubation: a closed claims analysis*, *Anesthesiology* **131** (2019), no. 4 818–829.

[136] M. Taboada, P. Doldan, A. Calvo, X. Almeida, E. Ferreiroa, A. Baluja, A. Cariñena, P. Otero, V. Caruezo, A. Naveira, *et. al.*, *Comparison of tracheal intubation conditions in operating room and intensive care unit: a prospective, observational study*, *Anesthesiology* **129** (2018), no. 2 321–328.

[137] J. L. Apfelbaum, C. A. Hagberg, R. T. Connis, B. B. Abdelmalak, M. Agarkar, R. P. Dutton, J. E. Fiadjoe, R. Greif, P. A. Klock Jr, D. Mercier, *et. al.*, *2022 american society of anesthesiologists practice guidelines for management of the difficult airway*, *Anesthesiology* **136** (2022), no. 1 31–81.

[138] M. E. Prekker, B. E. Driver, S. A. Trent, D. Resnick-Ault, K. P. Seitz, D. W. Russell, J. P. Gaillard, A. J. Latimer, S. A. Ghamande, K. W. Gibbs, *et. al.*, *Video versus direct laryngoscopy for tracheal intubation of critically ill adults*, *New England Journal of Medicine* (2023).

[139] L. Cabrini, G. Landoni, M. Baiardo Redaelli, O. Saleh, C. D. Votta, E. Fominskiy, A. Putzu, C. D. Snak de Souza, M. Antonelli, R. Bellomo, *et. al.*, *Tracheal intubation in critically ill patients: a comprehensive systematic review of randomized trials*, *Critical Care* **22** (2018), no. 1 1–9.

[140] J. R. Benger, K. Kirby, S. Black, S. J. Brett, M. Clout, M. J. Lazaroo, J. P. Nolan, B. C. Reeves, M. Robinson, L. J. Scott, *et. al.*, *Effect of a strategy of a supraglottic airway device vs tracheal intubation during out-of-hospital cardiac arrest on functional outcome: the airways-2 randomized clinical trial*, *Jama* **320** (2018), no. 8 779–791.

[141] H. R. Montgomery, F. K. Butler, S. D. Giebner, W. Kerr, C. C. Conklin, D. M. Morissette, M. A. Remley, T. A. Shaw, J. K. Torrisi, and T. A. Rich, *Tactical Combat Casualty Care Quick Reference Guide*. Department of Defense of the United States of America, first ed., 2017. https://nasemso.org/wp-content/uploads/tccc-quick-reference-guide-2017.pdf.

[142] M. A. Moucharite, J. Zhang, and R. Giffin, *Factors and economic outcomes associated with documented difficult intubation in the united states*, *Clinicoeconomics and Outcomes Research: CEOR* **13** (2021) 227.

[143] M. Bernhard, T. K. Becker, A. Gries, J. Knapp, and V. Wenzel, *The first shot is often the best shot: first-pass intubation success in emergency airway management*, *Anesthesia & Analgesia* **121** (2015), no. 5 1389–1393.

[144] B. J. Eastridge, R. L. Mabry, P. Seguin, J. Cantrell, T. Tops, P. Uribe, O. Mallett, T. Zubko, L. Oetjen-Gerdes, T. E. Rasmussen, *et. al.*, *Death on the battlefield (2001–2011): implications for the future of combat casualty care*, *Journal of trauma and acute care surgery* **73** (2012), no. 6 S431–S437.

[145] J. B. Holcomb, N. R. McMullin, L. Pearse, J. Caruso, C. E. Wade, L. Oetjen-Gerdes, H. R. Champion, M. Lawnick, W. Farr, S. Rodriguez, *et. al.*, *Causes of death in us special operations forces in the global war on terrorism: 2001–2004*, *Annals of surgery* **245** (2007), no. 6 986.

[146] S. G. Schauer, J. F. Naylor, J. J. Oliver, J. K. Maddry, and M. D. April, *An analysis of casualties presenting to military emergency departments in iraq and afghanistan*, *The American Journal of Emergency Medicine* **37** (2019), no. 1 94–99.

[147] U. Nimmagadda, M. R. Salem, and G. J. Crystal, *Preoxygenation: physiologic basis, benefits, and potential risks*, *Anesthesia & Analgesia* **124** (2017), no. 2 507–517.

[148] E. J. Perkins, J. L. Begley, F. M. Brewster, N. D. Hanegbi, A. A. Ilancheran, and D. J. Brewster, *The use of video laryngoscopy outside the operating room: A systematic review*, *Plos one* **17** (2022), no. 10 e0276420.

[149] A. B. Denmark, "Airway management trainer." https://www.ambu.com/emergency-care-and-training/training-manikins/product/ambu-airway-management-trainer.

[150] L. M. S. Norway, "Airway management trainer." https://laerdal.com/us/doc/92/Laerdal-Airway-Management-Trainer.

[151] L. M. S. Norway, "Deluxe difficult airway trainer." https://laerdal.com/us/doc/160/Deluxe-Difficult-Airway-Trainer.

[152] T. L. N. I. UK, "Airsim combo bronchi x." https://www.trucorp.com/P/64/AirSimComboBronchiX.

[153] T. L. N. I. UK, "Combo x difficult airway 1 & 2 pack." https://www.trucorp.com/P/119/ComboDifficultAirway12Pack.

[154] C. Eagle, *The relationship between a person's height and appropriate endotracheal tube length*, *Anaesthesia and intensive care* **20** (1992), no. 2 156–160.

[155] K. Yao, K. Goto, A. Nishimura, R. Shimazu, S. Tachikawa, and T. Iijima, *A formula for estimating the appropriate tube depth for intubation*, *Anesthesia Progress* **66** (2019), no. 1 8–13.

[156] J. DuCanto, K. D. Serrano, and R. J. Thompson, *Novel airway training tool that simulates vomiting: suction-assisted laryngoscopy assisted decontamination (salad) system*, *Western Journal of Emergency Medicine* **18** (2017), no. 1 117.